Density functional modelling of materials for fuel cell catalysts with reduced content of critical components

Alberto Figuerola Sánchez

Memòria presentada per

Alberto Figueroba Sánchez

per a optar al grau de Doctor per la Universitat de Barcelona

Programa de doctorat en Química Teòrica i Computacional

Density functional modelling of materials for fuel cell catalysts with reduced content of critical components

Alberto Figueroba Sánchez

2017

Dirigida per:

Dr. Konstantin M. Neyman

(Universitat de Barcelona i Institució Catalana de Recerca i Estudis Avançats)

UNIVERSITAT DE BARCELONA

Barcelona, 2017

UNIVERSITAT DE BARCELONA

FACULTAT DE QUÍMICA

DEPARTAMENT DE CIÈNCIA DELS MATERIALS I QUÍMICA FÍSICA

INSTITUT DE QUÍMICA TEÒRICA I COMPUTACIONAL

DENSITY FUNCTIONAL MODELLING OF MATERIALS FOR FUEL CELL CATALYSTS WITH REDUCED CONTENT OF CRITICAL COMPONENTS

Alberto Figueroba Sánchez

2017

A tots els que m'estimo

The work presented in this doctoral thesis has been carried out at the Materials Science and Physical Chemistry Department of the Chemistry Faculty of the University of Barcelona (UB), and within the Institute of Theoretical and Computational Chemistry (IQTCUB) and the Reference Network of Theoretical and Computational Chemistry of Catalonia (XRQTC).

This project has been possible in virtue of the financial support provided by the European Union (Grant FP7 nº310191). The work has been additionally supported by the Spanish *Ministerio de Economica y Competividad* (Grants CTQ2012-34969, CTQ2015-64618) and *Generalitat de Catalunya* (Grant 20014SGR97). Computer resources were partly provided by the Barcelona Supercomputing Center (*Red Española de Supercomputación*).

Agraïments

En primer lloc, m'agradaria donar els meus més sincers agraïments al meu director de tesi, el Prof. Konstantin Neyman. To acknowledge Konstantin properly I might switch to English. It is very difficult for me to explain in just few words how important Konstantin has been during these last years for me, not only as my supervisor, but also as a researcher. Since I started with the thesis work, he has not only played the strict role of a supervisor, but also has taught me every day how to became a better researcher and person. I am thankful of having him as a supervisor; I doubt I could have had a better one. En segon lloc, voldria també agrair especialment al meu director del Treball de Fi de Grau i del Màster, el Prof. Pere Alemany. Durant els dos anys que vaig passar al seu grup, em va transmetre la passió pels estudis computacionals, així com per l'estudi de sòlids cristal·lins. Em va mostrar com era treballar en investigació i com el treball dur donava els seus fruits. Estic molt orgullós d'haver pogut formar part del seu grup, encara que només fos de passada.

A part d'aquestes dues persones tant importants, m'agradaria donar les gràcies a tots aquells que han fet possible la realització d'aquesta tesi o, si bé no directament, han estat presents a la meva vida durant aquests anys. En primer lloc voldria nombrar als membres (o ex-membres) del grup del Konstantin, Sergey, Gábor, Hristiyan, i Albert, per tot el seu suport durant aquest temps. He tingut sort de poder coincidir amb uns companys de grup excel·lents, tant com a investigadors com en l'àmbit personal. Voldria també mencionar els membres del "Computational Materials Science Laboratory", en especial al professors titulars, Francesc, Carme, Iberio, Stefan i Francis els quals han estats sempre disposats a donar un cop de mà i als quals tinc gran estima. No em vull oblidar dels tècnics de l'IQTC Jordi i Teresa, per aguantar tots els e-mails amb dubtes i reclamacions tant quan les cues no tiraven com quan el Materials Studio decidia no funcionar. També voldria donar les gràcies als meus companys de despatx durant aquesta etapa: Marçal, Sergi, Maria, Dani, Andi, Tommaso, Toni i Isaac. Ha estat tot un plaer compartir despatx amb tots vosaltres.

A la meva segona família, el grup de B&B: Sergi, Uri, Noe, Almu, Julia, Sonia, Cristina, Raul i a tots els que van passar en algun moment per ell (en especial Mikel, KC i Félix). Sé que de vegades soc un borde dels grossos, però us estimo a tots amb bogeria. Soc un privilegiat per haver-vos pogut conèixer i haver compartit tants i tants moments amb vosaltres. Heu fet que aquest anys de tesi fossin dels més feliços de la meva vida.

A la meva tercera família, els companys de carrera, especialment la meva companya de pis durant aquesta etapa la Mireia, ets com una germana per mi i et dono les gràcies per haver pogut compartir amb tu tots aquests anys. Als companys de viciades, Llorca, Aymà, Lluch, Tommy, Eloy i Mario i als Chemistry's Carol, Montse, Joan, Annas varias i Vicky. A la Lidia Rosado, Marta, Loren, Jan, Omar, Pau i Branda. Gràcies a tots per continuar aguantant-me després de tots aquests anys.

A dues persones que han significat molt per mi durant aquests anys de tesi en diferents etapes, la Helena i la Eva. Gràcies per confiar tant en mi i per intentar fer-me millor persona.

Finalment, agrair a la meva família. Als meus pares, Fermín i Mª Ángeles, per haver-me deixat sempre escollir sempre el meu futur acadèmic sense ni tan sols fer una sola pregunta. M'heu recolzat sempre de manera incondicional i us estaré sempre agraït per això. Al meu germà Alejandro, que des de que me'n vaig anar a viure a Barcelona sembla que per fi siguem no només germans sinó també amics. Als meus avis, tant als que encara hi són (Magdalena), com als que se'n van anar abans (Fermín, Angelita i José). Cada dia me'n recordo de vosaltres, espero que pugueu estar orgullosos del vostre net. Aquesta tesi està especialment dedicada a vosaltres.

"We must not forget that when radium was discovered no one knew that it would prove useful in hospitals. The work was one of pure science. And this is a proof that scientific work must not be considered from the point of view of the direct usefulness of it. It must be done for itself, for the beauty of science, and then there is always a chance that scientific discovery may become like the radium a benefit for humanity."

Maria Skłodowska-Curie

(The first woman winning the Nobel Prize, Polish Physicist and Chemist, 1867-1934)

Table of contents

List of Definitions and Abbreviations

1 electronvolt (eV) = 96.485 kilojoules per mol (kJ mol^{-1})

E_{ad} adsorption energy

q Bader charge (of an atom)

E_{ad79} binding energy of a metal atom M on the edge of a cuboctahedral M_{79} particle

AO atomic orbital

ARXPS angle resolved X-ray photoelectron spectroscopy

BO Bloch orbital

CeO_2 cerium dioxide

DF density functional

DFT density functional theory

DRIFT diffuse reflectance infrared Fourier transform spectroscopy

DOS density of states

ΔE_{dop} energy of doping

E_{coh} experimental cohesive energy

$\Delta_f H$ experimental standard heat of formation

EXAFS extended X-ray absorption fine structure

FTIR Fourier transform infrared spectroscopy

LCAO linear combination of atomic orbitals

μ magnetization (of an atom, difference of its spin-up and spin-down electron density)

M metal (or metal atom)

MO	molecular orbital
NP	nanoparticle
E_{vac}	oxygen vacancy formation energy
OSC	oxygen storage capacity
O_{vac}	oxygen vacancy
SAC	single-atom catalyst
TPR	temperature-programmed reduction
TWC	three-way catalyst
VASP	Vienna Ab Initio Simulation Package
WGS	water gas shift reaction
XANES	X-ray absorption near edge structure
XPS	X-ray photoelectron spectroscopy

CHAPTER ONE

Introduction

The research work presented in this thesis deals with the study of the electronic, structural, and chemical properties of catalytic materials formed by transition metal species and cerium dioxide (CeO_2) by means of computational modeling and simulation. The initial motivation of the present work was devoted at developing knowledge-driven cost-efficient materials for their application in fuel cells as catalysts. Nevertheless, the findings obtained regarding the electronic and geometric structure of the studied systems allow for their useful employment for many other catalytic applications. In this chapter, an introduction to the importance of ceria-based catalysts is presented, highlighting their most relevant applications.

1.1. On catalysis

The best way for improving or fine-tuning the rate of a chemical process is by using catalysts. Catalysts are substances that interact with reactants (and products) modifying the reaction mechanism. The catalyst is both a reactant and a product, and its internal structure and concentration are ideally exactly the same at the start and at the end of the reaction. Catalysts actively participate in the chemical reactions, anchoring the reactants, transferring required chemical species to the reactants and generating reaction intermediates, and eventually forming and stabilizing products, with the concomitant final liberation of products. From a thermodynamic point of view, catalysts do not change the equilibrium of the chemical process, which depends only on the relative pressures of reactants when they are in gas phase, or their concentration in liquid media, and the overall system temperature. The interaction of the catalyst with reactants allows the reaction to proceed through alternative mechanisms, therefore modifying the energetic profile of the reaction process (Figure 1.1). This results in different reaction step energy barriers and overall reaction rates.

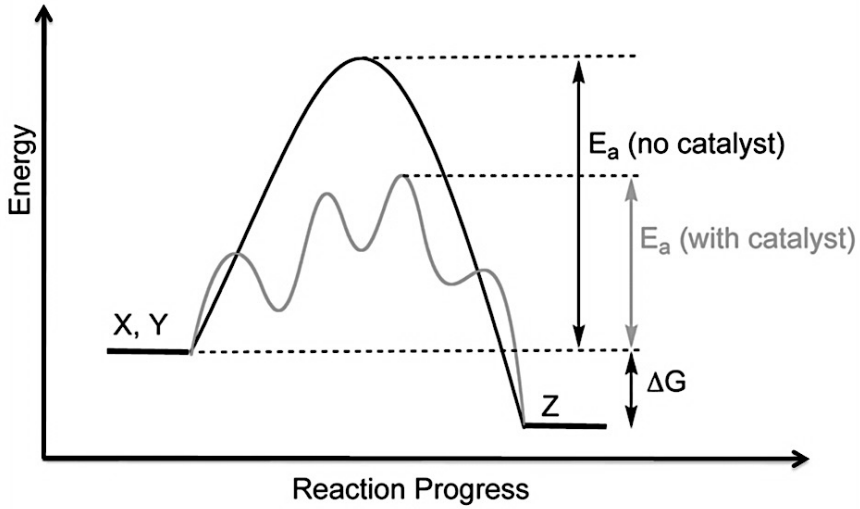

Figure 1.1. Energy profile of a chemical reaction, evolving from two reactants (X, Y) to a product (Z). The inclusion of a catalyst results in the modification of the reaction mechanism, leading to a lower activation barrier, E_a, with no change of the reaction exergonicity.

Catalysis can be considered homogeneous or heterogeneous depending on the physical state of the reactants and the catalyst. A catalyst is homogeneous when it has the same physical state as the reactants. In turn, a catalyst is heterogeneous if it is in a different physical state than the reactants. In such catalysts, the interaction between reactants and catalyst takes place at the interface between the different phases. In general, the heterogeneous catalysts used in industry are solids that react with liquid or gaseous mixtures of reactants. In such cases, reactants are adsorbed on the surface of the catalyst, modifying their geometric and electronic structure with respect the free molecules.

1.2. Catalysis by ceria

Cerium dioxide CeO_2 (also referred to as ceria) has been one of the most studied and employed materials for the development of heterogeneous catalysts during the last few decades. Ceria has been used as a key component in three-way catalysts (TWC) for the treatment of exhaust gases from automobiles.[1-3] Other catalytic applications such as removal of SO_x from fluid catalytic cracking flue gases[4-6] or as a component of several oxidation catalysts have also been reported.[7-14] Despite the obvious importance of CeO_2-based materials in industry, the detailed mechanistic understanding at the atomic level for many of these applications is still a mater of debate.

Ceria features some well-known key properties that make this material interesting for catalysis; for instance, as opposed to other non-reducible supports such as MgO or Al_2O_3, ceria can directly participate in chemical reactions due to the ability to either release O atoms under reducing conditions or uptake them under oxidative media. This feature is often referred to as oxygen storage capacity (OSC). Such release of O atoms results in the concomitant formation of vacancies, which can be refilled under oxidative conditions. In addition, cerium atoms can easily interchange their oxidation state from +4 to +3, depending on the reaction conditions. Thus, the redox couple Ce^{4+}/Ce^{3+} allows electrons left by released O atoms to be accommodated in cerium atoms. Ceria is also known to affect dispersion of supported metals;[15] promote the water gas shift (WGS)[16] and steam reforming reactions;[17] increase the thermal stability of the support;[2] promote noble metal reduction and oxidation;[15] store and release oxygen, hydrogen, and sulfur;[18] form surface and bulk vacancies;[19] and form intermetallic M–Ce compounds.[20] Nevertheless, ceria-based catalysts generally require transition metals to be active for industrial applications.[21]

The use of ceria is not only limited to catalysis. Doped-ceria materials have been tested for their use in solid oxide fuel cells (SOFC). Such devices transform chemical energy into electricity by reaction of fuels.[22] In such fuel cells, ceria is used as a solid electrolyte. Its modification and doping with metals allows the enhancement of the ionic conductivity of SOFC components, being able to be operative at low temperatures.[23-25] Ceria-based materials are also used as ethanol and NO_2 sensors,[26] and in membranes for separation of oxygen.[27] Finally, ceria has also been used for biomedical applications.[28-32]

1.3. Interaction of transition metals with ceria

Supported transition metals are extensively used as heterogeneous catalysts. Traditionally, the support played the role of providing the proper architecture for dispersing and stabilizing active metal particles. However, several other interactions can occur at the metal-oxide interface. Such interactions result in substantial modifications of the physical and chemical properties of both the oxide support and the metals and, in consequence, of the catalytic properties of the material. Anderson and Boudart suggested a definition of metal-support interactions as:[33] "*a direct influence of the support on the chemisorption and catalytic properties of the metal phase either by stabilizing unusual metal particle structure, by changing the electronical properties due to electron transfer processes between the metal particles and the support, or chemical bonding –compound formation– between metal and support*".

Some of the properties of ceria previously listed are strongly related to metal-support interactions. For example, the stabilization of dispersed metals[1,34-39] and formation of Ce-M alloys under reductive atmosphere[40,41] are obviously phenomena strongly biased by metal-oxide interactions. Several studies have addressed the interaction of metals and ceria under oxidizing conditions.[1,35,36,38,39,42-46] In principle, these focused on those transition metals used in automotive exhaust gases treatment catalysts, such as Pd, Pd, and Rh. Nevertheless, the elevated price of such noble metals hinders some of the large-scale applications of these ceria-based materials, for example, in fuel cell technologies.[47-49] In general, different studies have shown that under oxidative media, M-O surface complexes are formed with an improved degree of metal dispersion.[39] This relevant finding opens a novel route for the design of cost-efficient catalysts with the maximum specific catalytic performance of the noble metal content. Synthesis of such materials can be accomplished by finely dispersing atomic metal species on the surface of the support, resulting in systems denoted as single-atom catalysts (SACs).[15,50,51] Studies of SACs have been carried out not only using ceria as the support oxide, but also in other non-reducible oxides such as MgO. Nevertheless, the adsorption of such atomic transition metals appears to be too weak to prevent the sintering processes, such as their agglomeration in metal particles.[52] Thus, sufficiently stable SACs require specially strong binding sites on the support to counteract metal-metal bond formation.

Materials constituting SACs have been reported to be catalytically active for different reactions. Cationic Pt and Au species on nanostructured ceria[53] and in other non-reducible oxides, such as zeolites and silica,[54,55] catalyze the WGS reaction at relatively low temperatures. Pd cations adsorbed on alumina[56] and Pt on FeO_x[57] have also been reported to be active towards CO oxidation. Finally, hydrogenation activity has been attributed to materials composed by Pd atoms anchored to cavities of mesoporous graphitic carbon nitride[58] and FeO_x-supported Pt.[59]

1.4. Motivation and outline of the thesis

As pointed out in the current section, CeO_2-based materials with different transition metals are particularly important for diverse catalytic applications. However, many aspects regarding understanding of the materials at the atomic level remain unclear and are still a debate focus. In addition, many of the previously mentioned transition metals, such as Pd, Pt, and Rh, are expensive, and this hinders their large-scale applications. Thus, in order to be able to design cost-efficient materials for catalytic applications, a better understanding of the interactions between transition metals and ceria is required, with the ultimate goal of maximizing the catalytic power per active transition metal quantity.

In this thesis, a computational study of the interactions arising upon deposition of transition metals on ceria has been performed, aiming for a comprehensive understanding of the nature of such interactions. In addition, a better understanding at the atomistic level of the structure of metal-ceria materials can lead to a knowledge-driven design of new improved and cost-efficient catalysts.

This thesis is structured as follows: **Chapter 2** describes the methodology and models used for carrying out the research work, together with the necessary theoretical background. Such background includes description of periodic systems, structural concepts, electronic structure, Bloch theorem, and density functional theory (DFT) including the Hubbard +U correction.

Chapter 3 involves the research carried out to study a novel type of heterogeneous catalyst: Single atom catalysts. The idea behind these interesting materials is to

maximize the efficiency of the metal content included in ceria. Formation of SACs is a promising way of developing cost-efficient materials, since all the metal content is located at the surface, available for reactants. Thus, we studied the interaction of 12 different transition metal atoms with nanostructured ceria. In addition, we analyzed how stable such composites are with respect to undesired processes typical from harsh conditions in fuel cells: sintering and agglomeration.

Chapter 4 describes and analyzes an alternative way of treating SACs. This alternative is based on the substitutional insertion of a transition metal atom by one metal of the lattice of the support. This process is often referred to as doping. Thus, we studied the effect of doping ceria with 4 different transition metals (Pt, Pd, Ni, and Cu) together with the possible implications of two typical reduction processes (formation of O vacancies and homolytic dissociative adsorption of H_2) present in catalytic environments.

Chapter 5 deals with one of the most important features of ceria for catalytic applications: modification of its OSC. In particular, we performed detailed analysis on how the OSC of ceria can be modified at an atomistic level and their implications in catalysis. In addition, we tackle the possible effect of nanostructuring and metal loading on the OSC of ceria.

Chapter 6 summarizes a study regarding the stability of Pt^{2+} species when located at the surface of ceria. For instance, many catalytic applications, such as dissociation of hydrogen, require metal particles to be present. We tackle three possible ways of reductive stabilizing such systems: i) by formation of O vacancies, ii) metal loading, and iii) adsorption of Sn atoms.

Chapter 7 deals with characterization of Pt/CeO_2 thin films through analysis of the frequency modes of CO molecules. A detailed comparison between the experimental and calculated frequencies is presented, explaining the obtained trends. We also tackle the effect ceria support induces in the frequency modes of CO, together with the possible dependency on the particle size.

The conclusions of this thesis are given in **Chapter 8**.

1.5. References

(1) Summers, J. C.; Ausen, S. A. Interaction of Cerium Oxide with Noble Metals. *J. Catal.* **1979**, *58*, 131–143.

(2) Kim, G. Ceria-Promoted Three-Way Catalysts for Auto Exhaust Emission Control. *Sect. Title Air Pollut. Ind. Hyg.* **1982**, *21*, 267–274.

(3) Gandhi, H.; Piken, A.; Shelef, M.; Delosh, R. Laboratory Evaluation of Three-Way Catalysts. *SAE Pap. 760201* **1976**, *55*.

(4) Bhattacharyya, A. A.; Woltermann, G. M.; Yoo, J. S.; Karch, J. A.; Cormier, W. E. Catalytic SO_x Abatement: The Role of Magnesium Aluminate Spinel in the Removal of SO_x from Fluid Catalytic Cracking (FCC) Flue Gas. *Ind. Eng. Chem. Res.* **1988**, *27*, 1356–1360.

(5) Yoo, J. S.; Jaecker, J. A. U.S. Patent 4,469,589, 1984.

(6) Bertolacini, R. J.; Hirschberg, E. H.; Modica, F. S. U.S. Patent 4,497,902, 1985.

(7) Kilbourn, B. T. The Role of the Lanthanides in Applied Catalysis. *J. Less-Common Met.* **1986**, *126*, 101–106.

(8) Liu, W.; Flytzani-Stephanopoulos, M. Total Oxidation of Carbon Monoxide and Methane over Transition Metal-Fluorite Oxide Composite Catalysts. *J. Catal.* **1995**, *153*, 304–316.

(9) Brazdil, J. F.; Grasselli, R. K. Relationship between Solid State Structure and Catalytic Activity of Rare Earth and Bismuth-Containing Molybdate Ammoxidation Catalysts. *J. Catal.* **1983**, *79*, 104–117.

(10) Imamura, S.; Uematsu, Y.; Utani, K.; Ito, T. Combustion of Formaldehyde on Ruthenium/Cerium (IV) Oxide Catalyst. *Ind. Eng. Chem. Res.* **1991**, *30*, 18–21.

(11) Zamar, F.; Trovarelli, A.; de Leitenburg, C.; Dolcetti, G. CeO_2-Based Solid Solutions with the Fluorite Structure as Novel and Effective Catalysts for Methane Combustion. *J. Chem. Soc. Chem. Commun.* **1995**, 965.

(12) Yu, Z. Q.; Yang, X. M.; Lunsford, J. H.; Rosynek, M. P. Oxidative Coupling of Methane over Na_2WO_4/CeO_2 and Related Catalysts. *J. Catal.* **1995**, *154*, 163–173.

(13) Haneda, M.; Mizushima, T.; Kakuta, N.; Ueno, A.; Sato, Y.; Matsuura, S.; Kasahara, K.; Sato, M. Structural Characterization and Catalytic Behavior of Al_2O_3-Supported Cerium Oxides. *Bull. Chem. Soc. Jpn.* **1993**, *66*, 1279–1288.

(14) Amirkhanova, A. K.; Krichevskii, L. A.; Kagarlitskii, A. D. Oxidative Ammonolysis of 2,5-Dimethylbyrazine over Molybdena Ceria Titania Catalysts. *Kinet. Catal.* **1994**, *35*, 838–840.

(15) Flytzani-Stephanopoulos, M.; Gates, B. C. Atomically Dispersed Supported Metal Catalysts. *Annu. Rev. Chem. Biomol. Eng.* **2012**, *3*, 545–574.

(16) Bunluesin, T.; Gorte, R. J.; Graham, G. W. Studies of the Water-Gas-Shift Reaction on Ceria-Supported Pt, Pd, and Rh: Implications for Oxygen-Storage Properties. *Appl. Catal. B Environ.* **1998**, *15*, 107–114.

(17) Lin, S. S. Y.; Kim, D. H.; Engelhard, M. H.; Ha, S. Y. Water-Induced Formation of Cobalt Oxides over Supported Cobalt/ceria-Zirconia Catalysts under Ethanol-Steam Conditions. *J. Catal.* **2010**, *273*, 229–235.

(18) Zhou, K.; Wang, X.; Sun, X.; Peng, Q.; Li, Y. Enhanced Catalytic Activity of Ceria Nanorods from Well-Defined Reactive Crystal Planes. *J. Catal.* **2005**, *229*, 206–212.

(19) Paier, J.; Penschke, C.; Sauer, J. Oxygen Defects and Surface Chemistry of Ceria: Quantum Chemical Studies Compared to Experiment. *Chem. Rev.* **2013**, *113*, 3949–3985.

(20) Kuhlenbeck, H.; Shaikhutdinov, S.; Freund, H.-J. Well-Ordered Transition Metal Oxide Layers in Model Catalysis – A Series of Case Studies. *Chem. Rev.* **2013**, *113*, 3986–4034.

(21) Trovarelli, A. Catalytic Properties of Ceria and CeO_2-Containing Materials. *Catal. Rev.* **1996**, *38*, 439–520.

(22) Steele, B. C.; Heinzel, A. Materials for Fuel-Cell Technologies. *Nature* **2001**, *414*, 345–352.

(23) Inaba, H.; Tagawa, H. Ceria-Based Solid Electrolytes. *Solid State Ionics* **1996**, *83*, 1–16.

(24) Hibino, T.; Hashimoto, A.; Inoue, T.; Tokuno, J. I.; Yoshida, S. I.; Sano, M. A Low-Operating-Temperature Solid Oxide Fuel Cell in Hydrocarbon-Air Mixtures. *Science* **1999**, *288*, 2031–2033.

(25) Shao, Z.; Haile, S. M. A High-Performance Cathode for the next Generation of Solid-Oxide Fuel Cells. *Nature* **2004**, *431*, 170–173.

(26) Barreca, D.; Gasparotto, A.; Maccato, C.; Maragno, C.; Tondello, E.; Comini, E.; Sberveglieri, G. Columnar CeO_2 Nanostructures for Sensor Application. *Nanotechnology* **2007**, *18*, 125502.

(27) Brinkman, K. S.; Takamura, H.; Tuller, H. L.; Iijima, T. The Oxygen Permeation Properties of Nanocrystalline CeO_2 Thin Films. *J. Electrochem. Soc.* **2010**, *157*, B1852–B1857.

(28) Tarnuzzer, R. W.; Colon, J.; Patil, S.; Seal, S. Vacancy Engineered Ceria Nanostructures for Protection from Radiation-Induced Cellular Damage. *Nano Lett.* **2005**, *5*, 2573–2577.

(29) Pagliari, F.; Mandoli, C.; Forte, G.; Magnani, E.; Pagliari, S.; Nardone, G.; Licoccia, S.; Minieri, M.; Di Nardo, P.; Traversa, E. Cerium Oxide Nanoparticles Protect Cardiac Progenitor Cells from Oxidative Stress. *ACS Nano* **2012**, *6*, 3767–3775.

(30) Niu, J.; Azfer, A.; Rogers, L. M.; Wang, X.; Kolattukudy, P. E. Cardioprotective Effects of Cerium Oxide Nanoparticles in a Transgenic Murine Model of Cardiomyopathy. *Cardiovasc. Res.* **2007**, *73*, 549–559.

(31) Das, M.; Patil, S.; Bhargava, N.; Kang, J. F.; Riedel, L. M.; Seal, S.; Hickman, J. J. Auto-Catalytic Ceria Nanoparticles Offer Neuroprotection to Adult Rat Spinal Cord Neurons. *Biomaterials* **2007**, *28*, 1918–1925.

(32) Chen, J.; Patil, S.; Seal, S.; McGinnis, J. F. Rare Earth Nanoparticles Prevent Retinal Degeneration Induced by Intracellular Peroxides. *Nat. Nanotechnol.* **2006**, *1*, 142–150.

(33) Anderson, J. R.; Boudart, M. *Catalysis - Science and Technology*; Berlin, S.-V., Ed.; Vol. 6.; 1984.

(34) Luc Duplan, J.; Praliaud, H. Infrared Determination of the Accessible Metallic Surface of Supported Palladium Containing Ceria. *Appl. Catal.* **1990**, *67*, 325–335.

(35) Diwell, A. F.; Rajaram, R. R.; Shaw, H. A.; Truex, T. J. The Role of Ceria in Three-Way Catalysts. *Stud. Surf. Sci. Catal.* **1991**, *71*, 139–152.

(36) Shyu, J. Z.; Otto, K.; Watkins, W. L. H.; Graham, G. W.; Belitz, R. K.; Gandhi, H. S. Characterization of Pd/γ-Alumina Catalysts Containing Ceria. *J. Catal.* **1988**, *114*, 23–33.

(37) Ramaroson, E.; Tempere, J. F.; Guilleux, M. F.; Vergand, F.; Roulet, H.; Dufour, G. Spectroscopic Characterization and Reactivity Study of Ceria-Supported Nickel Catalysts. *J. Chem. Soc., Faraday Trans.* **1992**, *88*, 1211–1218.

(38) Shyu, J. Z.; Otto, K. Characterization of Pt/γ-Alumina Catalysts Containing Ceria. *J. Catal.* **1989**, *115*, 16–23.

(39) Murrel, L. L.; Tauster, S. J.; Anderson, D. R. Laser Raman Characterization of Surface Phase Precious Metal Oxides Formed on CeO_2. *Catal. Automot. Pollut. Control II* **1991**, *71*, 275–289.

(40) Kepiński, L.; Wolcyrz, M.; Okal, J. Effect of Chlorine on Microstructure and Activity of Pd/CeO_2 Catalysts. *J. Chem. Soc. Faraday Trans.* **1995**, *91*, 507.

(41) Meriaudeau, P.; Dutel, J. F.; Dufaux, M.; Naccache, C. Further Investigation on Metal-Support Interaction: TiO_2, CeO_2, SiO_2 Supported Platinum Catalysts. *Stud. Surf. Sci. Catal.* **1982**, *11*, 95–104.

(42) Munuera, G.; Fernández, A.; González-Elipe, A. R. The Role of the Oxygen Vacancies at the Support in the Co Oxidation on Rh/CeO_2 and Rh/TiO_2 Autocatalysts. *Stud. Surf. Sci. Catal.* **1991**, *71*, 207–219.

(43) Brogan, M. S.; Dines, T. J.; Cairns, J. A. Raman Spectroscopic Study of the Pt-CeO_2 Interaction in the Pt/Al_2O_3-CeO_2 Catalyst. **1994**, *90*, 1461–1466.

(44) Soria, J.; Martínez-Arias, A.; Conesa, J. C. Effect of Oxidized Rhodium on Oxygen Adsorption on Cerium Oxide. *Vacuum* **1992**, *43*, 437–440.

(45) Bernal, S.; Botana, F. J.; Calvino, J. J.; Cifredo, G. A.; Pérez-Omil, J. A.; Pintado, J. M. HREM Study of the Behaviour of a Rh/CeO_2 Catalyst under High Temperature Reducing and Oxidizing Conditions. *Catal. Today* **1995**, *23*, 219–250.

(46) Bernal, S.; Blanco, G.; Calvino, J. J.; Cifredo, G. A.; Omil, J. A. P.; Pintado, J. M.; Varo, A. HRTEM and TPO Study of the Behaviour under Oxidizing Conditions of Some Rh/CeO_2 Catalysts. *Stud. Surf. Sci. Catal.* **1994**, *82*, 507–514.

(47) Tollefson, J. Worth Its Weight in Platinum. *Nature* **2007**, *450*, 334–335.

(48) Vielstich, W.; Lamm, A.; Gasteiger, H. A. *Handbook of Fuel Cells: Fundamentals, Technology, Applications*; Wiley: Chichester, 2013.

(49) Stamenkovic, V. R.; Mun, B. S.; Arenz, M.; Mayrhofer, K. J. J.; Lucas, C. A.; Wang, G. F.; Ross, P. N.; Markovic, N. M. Trends in Electrocatalysis on Extended and Nanoscale Pt-Bimetallic Alloy Surfaces. *Nat. Mater.* **2007**, *6*, 241–247.

(50) Flytzani-Stephanopoulos, M. Gold Atoms Stabilized on Various Supports

Catalyze the Water–Gas Shift Reaction. *Acc. Chem. Res.* **2014**, *47*, 783–792.

(51) Yang, X.-F.; Wang, A.; Qiao, B.; Li, J.; Liu, J.; Zhang, T. Single-Atom Catalysts: A New Frontier in Heterogeneous Catalysis. *Acc. Chem. Res.* **2013**, *46*, 1740–1748.

(52) Neyman, K. M.; Inntam, C.; Nasluzov, V. A.; Kosarev, R.; Rösch, N. Adsorption of D-Metal Atoms on the Regular MgO(001) Surface: Density Functional Study of Clustermodels Embedded in an Elastic Polarizable Environment. *Appl. Phys. A* **2004**, *78*, 823–828.

(53) Fu, Q.; Saltsburg, H.; Flytzani-Stephanopoulos, M. Active Nonmetallic Au and Pt Species on Ceria-Based Water-Gas Shift Catalysts. *Science* **2003**, *301*, 935–938.

(54) Zhai, Y.; Pierre, D.; Si, R.; Deng, W.; Ferrin, P.; Nilekar, A. U.; Peng, G.; Herron, J. A.; Bell, D. C.; Saltsburg, H.; Mavrikakis, M.; Flytzani-Stephanopoulos, M. Alkali-Stabilized Pt-OHx Species Catalyze Low-Temperature Water-Gas Shift Reactions. *Science* **2010**, *329*, 1633–1637.

(55) Yang, M.; Li, S.; Wang, Y.; Herron, J. A.; Xu, Y.; Allard, L. F.; Lee, S.; Huang, J.; Mavrikakis, M.; Flytzani-Stephanopoulos, M. Catalytically Active Au-$O(OH)_x$- Species Stabilized by Alkali Ions on Zeolites and Mesoporous Oxides. *Science* **2014**, *346*, 1498–1501.

(56) Peterson, E. J.; DeLaRiva, A. T.; Lin, S.; Johnson, R. S.; Guo, H.; Miller, J. T.; Kwak, J. H.; Peden, C. H. F.; Kiefer, B.; Allard, L. F.; Ribeiro, F. H.; Datye, A. K. Low-Temperature Carbon Monoxide Oxidation Catalysed by Regenerable Atomically Dispersed Palladium on Alumina. *Nat. Commun.* **2014**, *5*, 4885.

(57) Qiao, B.; Wang, A.; Yang, X.; Allard, L. F.; Jiang, Z.; Cui, Y.; Liu, J.; Li, J.; Zhang, T. Single-Atom Catalysis of CO Oxidation Using Pt_1/FeO_x. *Nat. Chem.* **2011**, *3*, 634–641.

(58) Vilé, G.; Albani, D.; Nachtegaal, M.; Chen, Z.; Dontsova, D.; Antonietti, M.; López, N.; Pérez-Ramírez, J. A Stable Single-Site Palladium Catalyst for Hydrogenations. *Angew. Chemie Int. Ed.* **2015**, *54*, 11265–11269.

(59) Wei, H.; Liu, X.; Wang, A.; Zhang, L.; Qiao, B.; Yang, X.; Huang, Y.; Miao, S.; Liu, J.; Zhang, T. FeO_x-Supported Platinum Single-Atom and Pseudo-Single-Atom Catalysts for Chemoselective Hydrogenation of Functionalized Nitroarenes. *Nat. Commun.* **2014**, *5*, 5634.

CHAPTER TWO

Theoretical background

In this chapter, an overview of the theoretical background behind band theory, Density Functional Theory (DFT) and the application of the latter to condensed matter, with particular focus on the aspects related to the present work is presented. The computer code used to perform all calculations of the research work is the Vienna Ab initio Simulation Package (VASP).[1-3] This program treats systems in a periodic environment. Some details regarding application of VASP to the studies of ceria-based materials are also briefly discussed.

2.1. Periodic solids

First, prior to starting with the theoretical deductions based on the Schrödinger equation that allows calculation of the electronic structure of a given system, the model known as periodic solid will be introduced. This will help us to bridge theoretical methods for description of isolated molecules to those employed in the case of periodic solids, in a similar way as VASP considers all systems.

A crystal is a macroscopic system formed by a huge number of atoms set in a regular fashion in the three-dimensional space. Due to the impossibility of solving the electronic Schrödinger equation for the complete system, which might be formed by a number of around 10^{24} electrons, the study of the electronic structure of solids is based on a simplified model called periodic system. A periodic system can be defined as a system containing infinite number of atoms, but with a relatively simple structure obtained by repetition of a structural unit formed by a small number of atoms by translations. In principle, if the number of atoms contained in the structural unit repeated by translations is small with respect the total number of atoms forming the crystal, the periodic solid model reproduces well the structural properties of the crystal overall, except that in a real crystal of finite size there are surfaces separating the interior and the exterior parts of the crystal. Thus, the periodic model provides a reasonable approximation to the properties derived from the electronic structure of the interior of the crystal. For instance, if we want to know the electric or magnetic properties of a crystalline solid, the periodic solid model should be enough for obtaining a proper description.

The structural unit used for building the periodic solid can be formed by just a single atom or can feature a more complex structure, containing a number N of atoms. Depending on the directions used for propagating the unit cell in the space, periodic solids of one, two or three dimension can be built if one, two or three translational vectors linearly independent are used in the construction of the crystal.

2.2. Electronic structure and orbitals

Below, the concept of orbital will be introduced and illustrated how it arises by developing of the Schrödinger equation.

The electronic structure of whatever system composed by either atoms, molecules or, even, crystals can be described by the Schrödinger equation for electrons and nuclei that form the system. The time-independent Schrödinger equation will be used for the present development:

$$\hat{H}\Psi = E\Psi \ , \tag{2.1}$$

where Ψ is the wave function for the particles of the system, and $\hat{H}$ is the Hamiltonian operator applied to Ψ for calculating the energy eigenvalue E. $\hat{H}$ can be obtained adding the kinetic energy $\hat{T}$ and potential energy $\hat{V}$ operators of the particles of the system under study:

$$\hat{H} = \hat{T} + \hat{V}(r) \ . \tag{2.2}$$

The Hamiltonian operator $\hat{H}$ for a system formed by *M* nuclei and *N* electrons can be written, without relativistic corrections, in the following way:

$$\hat{H} = -\sum_{i=1}^{N} \frac{\hbar^2}{2m} \nabla_i^2 - \sum_{A=1}^{M} \frac{\hbar^2}{2M_A} \nabla_A^2 - \frac{1}{4\pi e_0} \left(\sum_{i=1}^{N} \sum_{A=1}^{M} \frac{z_A e^2}{r_{iA}} - \sum_{i=1}^{N} \sum_{j>i}^{N} \frac{e^2}{r_{ij}} - \sum_{A=1}^{M} \sum_{B>A}^{M} \frac{z_A z_B e^2}{r_{AB}} \right) . \quad (2.3)$$

The two first terms of $\hat{H}$ represent the kinetic energies of N electrons with mass m and M nuclei with mass M_A. In this equation ∇^2 is the Laplace operator that, in Cartesian coordinates, is expressed as:

$$\nabla^2 = \nabla \bullet \nabla = \frac{\partial^2}{\partial x^2} + \frac{\partial^2}{\partial y^2} + \frac{\partial^2}{\partial z^2} \ . \quad (2.4)$$

The third term of equation (2.3) represents the attractive interaction between electrons (with charge $-e$) and nuclei (with charge $+z_A e$) at the distance r_{iA} separating the i-th electron from the A-th nuclei. The forth and fifth terms are related with the electrostatic repulsion between electrons and nuclei, respectively. The double count of such interactions is excluded implicitly at the summation considering $j > i$ and $B > A$.

The resulting Schrödinger equation cannot be solved analytically (except for the simples cases with just one electron), which implies the application of a series of approximations to reach a useful solution. The first of such simplifications was to neglect the temporal effect on the wave function Ψ, using the time-independent Schrödinger equation (2.1). The second approximation consists in assuming that all electrons feature much higher velocities than the nuclei due to the much higher mass of the latter with respect to electrons. This implies that the positions of the nuclei can be fixed, when positions of electrons are studied. This is the so-called Born-Oppenheimer approximation. When removing the change in the nuclear coordinates from Equation (2.3) the wave function Ψ becomes function only of the electronic coordinates and the fifth term in the Hamiltonian irrelevant for the calculation of Ψ can be neglected when solving the time-independent Schrödinger equation and then added as a constant.

Using atomic units and the above mentioned approximations, the Hamiltonian operator describing the electronic movement of a system with fixed nuclei reads:

$$\hat{H} = -\sum_{i=1}^{N} \frac{1}{2} \nabla_i^2 - \sum_{i=1}^{N} \sum_{A=1}^{M} \frac{z_A}{r_{iA}} + \sum_{i=1}^{N} \sum_{j>i}^{N} \frac{1}{r_{ij}} \quad , \tag{2.5}$$

where the first term corresponds to the kinetic energy of electrons, the second term – to the attractive potential of nuclei towards electrons and the third term – to the electrostatic repulsion between electrons.

Ab initio theoretical methods of calculation are those which, up to this point, do not use further simplifications in the Hamiltonian (Equation (2.5)). Nevertheless, the repulsion term between electrons hinders the solution of the Schrödinger equation for each electron separately, making necessary further approximations for solving the resulting coupled equation system.

In molecular quantum chemistry, an approximate many-electron Ψ can be obtained from a series of one-electron functions ψ_i called molecular orbitals (MO). Despite that it is desirable that the electrons described by this set of functions ψ_i were independent from each other, resulting in a total wave function Ψ as a product of all MO ψ_i, it is not true and, thus, the Schrödinger equation for the *N* electron system has to be solved in an iterative manner. Nevertheless, using a set of ψ_i for approximating Ψ of the *N* electrons is a good starting point. In such approximation, the movement of each electron can be considered independent of the other electrons in an average field created by all other electrons of the molecule.

If we express the MO as a linear combination of basis set functions similar to the ones that describe electrons in isolated atoms (atomic orbitals (AOs)) we obtain the linear combination of atomic orbitals (LCAO),

$$\psi_i(r) = \sum_{A} \sum_{\substack{\mu=1 \\ \mu \in A}}^{n} c_{\mu i} \phi_\mu(r) \quad , \tag{2.6}$$

where the base functions $\phi_\mu(r)$ are AOs localized on the different atoms *A* forming the molecule. Note, that the AOs can be, for instance, solutions of the Schrödinger equation for hydrogen-like orbitals (atoms with only one electron and nuclear charge z_A).

For finding the best *N*-electron Ψ, the variational theorem is used, which states that this will be the wave function corresponding to the lowest energy. Ψ can be found calculating the expectation value *E*,

$$E = \frac{\int \Psi^* \hat{H} \Psi d\tau}{\int \Psi^* \Psi d\tau} = \frac{\langle \Psi | \hat{H} | \Psi \rangle}{\langle \Psi | \Psi \rangle} \geq E_0 \cdot \tag{2.7}$$

Ψ is a complex function, including an imaginary part, with Ψ^* being its complex conjugate.

If Equation (2.5) is used for describing a MO as combination of AO one obtains:

$$E_i = \frac{\sum_A \sum_B \sum_\mu \sum_\nu c^*_{\mu i} c_{\nu i} \langle \phi_\mu | \hat{H} | \phi_\mu \rangle}{\sum_A \sum_B \sum_\mu \sum_\nu c^*_{\mu i} c_{\nu i} \langle \phi_\mu | \phi_\mu \rangle} = \frac{\sum_A \sum_B \sum_\mu \sum_\nu c^*_{\mu i} c_{\nu i} H_{\mu\nu}}{\sum_A \sum_B \sum_\mu \sum_\nu c^*_{\mu i} c_{\nu i} S_{\mu\nu}} , \tag{2.8}$$

defining, at the right side of the equation, the Hamiltonian $H_{\mu\nu}$ and overlap $S_{\mu\nu}$ integrals. Applying the variational theorem, one obtains a linear equation set, which can be solved matching the secular determinant to zero. Thus, *N* values E_i for the energy or eigenvalues of the Hamiltonian can be obtained. Introducing each of such values in the equation system, one can calculate *N* sets of coefficients $c_{\mu i}$, a set for each different value of E_i, also called eigenvector of $\hat{H}$.

2.3. Bloch theorem

Herein, we introduce the treatment required for theoretically studying systems such as crystalline solids. For systems with many atoms a problem arises, when solving the secular determinant obtained by LCAO procedure due to the huge dimensions of the matrices and, therefore, of the resulting secular equation. To overcome this obstacle, one can describe the electronic structure of a unit cell of the crystal and utilize the translational symmetry of the system for obtaining the electronic structure of the whole system.

Crystals are translationally invariant in the three dimensions of the space. Therefore, one can use the translational symmetry for generating the Ψ of the crystal, which is composed by crystal orbitals called electron bands.[4]

For an ideal crystalline solid, the potential $V(r)$, to which electrons are subjected, has to be identical in all cells due to the periodicity of the lattice, expressed by the vector T,

$$V(r+T) \equiv V(r) \ . \tag{2.9}$$

Bloch theorem enounces that such periodicity in the potential implies that the wave functions describing the electrons of a solid, or crystal orbitals, $\Psi(r,k)$ have to be also periodic and, therefore, can be expressed as a lineal combination of Bloch orbitals (BO)

$$\Psi\left(r,k\right)=\sum_{\mu}c_{\mu}\left(k\right)\phi_{\mu}\left(r,k\right)\ , \tag{2.10}$$

where the summation is extended to the number of AO associated with atom μ. In this expression $\phi_{\mu}\left(r,k\right)$ corresponds to a BO and $c_{\mu}\left(k\right)$ – to the coefficients indicating the participation of each BO in the crystal orbitals. Note that these crystal orbitals are equivalents to the MOs in the case of a molecule. Equation (2.10) is analogous to Equation (2.6) for an extended system. In the case of a solid, instead of expressing the orbitals of the system using a basis of AOs they are expressed using a base of BOs, which are nothing else but linear combinations of atomic orbitals adapted to the translational symmetry of the system. BOs are constructed from the AOs χ_{μ} by

$$\phi_{\mu}\left(r,k\right)=\sum_{n}e^{ikR_{n}}\chi_{\mu}\left(r-R_{n}\right)\ , \tag{2.11}$$

where the equivalent (infinite) AOs in each cell are multiplied by a phase factor $e^{ikR_{n}}$, R_{n} indicates in which unit cell the orbital $\chi_{\mu}\left(r-R_{n}\right)$ is found. The summation is extended up to the number of unit cells (infinite) forming the solid, *n*. Thus, from the linear combination of the same type of AOs χ_{μ} of each of the unit cells of a solid a set of orbitals is constructed, BOs, which are extended in the whole solid and that can be combined using Equation (2.10) for obtaining the crystal orbitals $\Psi\left(r,k\right)$.[4]

Important conclusions can be drawn from the previous equations. First, Ψ of a solid can be calculated as a linear combination of extended orbitals, which is much easier than to combine each of the AOs separately. Furthermore, the periodicity on the potential $V\left(r+T\right)$ allows one to produce an infinite number of BOs due to the parameter k used in their construction, which is a continuous parameter. As we will

have as many crystal orbitals as BOs we combine, the number of crystal orbitals will be also infinite. Considering all crystal orbitals, their energies do not correspond to finite values, but to allowed energy bands separated by regions of forbidden energies or gaps. Finally, a quantum number k has been introduced for constructing the different BOs $\Psi(r,k)$.[4]

2.4. k number, Brillouin zone and electronic bands

As mentioned in the previous section, BOs for a periodic system depend on a quantum number called k, which is used for constructing them. This number has inverse length units and, in mathematical language, it is defined at the reciprocal space associated with the crystalline lattice, defined in the physical space, called real space.[4] Reciprocal space is a mathematical tool used for simplifying the treatment of infinite periodic systems, such as crystals.

Whatever position in three-dimensional Euclidean space can be defined by a vector, which is linear combination of three linear independent base vectors $\vec{a}_1$, $\vec{a}_2$ and $\vec{a}_3$:

$$\vec{Q} = p\vec{a}_1 + q\vec{a}_2 + r\vec{a}_3 \ . \tag{2.12}$$

Position of each point of the periodic lattice in the real space is defined by a vector

$$\vec{R} = n_1\vec{a}_1 + n_2\vec{a}_2 + n_3\vec{a}_3 \ , \tag{2.13}$$

where, differently from the previous case, we can only consider integer values for the coefficients n_1, n_2 and n_3.

For the lattice $\{\vec{R}\}$ we can construct a new lattice, called reciprocal lattice, whose points $\vec{K}$ can be expressed as a function of a set of reciprocal vectors $\vec{g}_1$, $\vec{g}_2$ and $\vec{g}_3$

$$\vec{K} = m_1\vec{g}_1 + m_2\vec{g}_2 + m_3\vec{g}_3 \ . \tag{2.14}$$

The reciprocal lattice can be obtained from the real one taking into account that, by definition, real and reciprocal space vectors are related by the equation

$$e^{i\vec{K}\vec{R}} = 1 \ . \tag{2.15}$$

This relation is similar to the orthogonality relation between basis vectors. Independently of the dimensionality of the system, reciprocal space vectors have inverse length units.

Band electronic structure is the representation of the energy of a wave function extended as a function of quantum number k. It is, thus, the equivalent of the energy diagrams of MOs for a crystal. Crystal orbitals are k-dependent wave functions. Therefore, they will be as many as k numbers are considered. In principle, as the number of atoms in the lattice is infinite, infinite number of AOs will be obtained and, thus, infinite BOs (each with a different value of k) that will be combined for producing an infinite number of crystal orbitals.[4]

Although there is infinite number of possible k points, the values that can feature this number are reduced due to the periodicity of the lattice. In order to deduce such values the example of a macroscopic one-dimensional crystal with length L can be used. We will also consider that the crystal is compound of a huge number of unit cells N with lattice parameter a. If we glue the unit cells of the ends forming a ring, the

wave function of the system will be continuous. Applying the Bloch theorem for whatever value of k one obtains

$$\psi(k,0) \equiv \psi(k,L) = e^{ikL}\psi(k,0) \ . \tag{2.16}$$

Equation (2.16) is applicable for all range of k, if the exponential (k,L) is multiple of 2π. Thus, k values are limited to the range of $-\frac{\pi}{\vec{a}} \le k \le \frac{\pi}{\vec{a}}$ (2.17).

The latter three-dimensional relation can be written shortly as $0 \le |k| \le \frac{\pi}{\vec{a}}$, and the set of points in the reciprocal space fulfilling this condition are called Brillouin zone.[4] The Brillouin zone is the unit cell of the reciprocal space and, thus, one can generate the whole reciprocal space by repetition of the Brillouin zone. For instance, it is a special case of unit cell, the so-called Wigner-Seitz cell, which is the unit cell containing all the non-translational symmetry of a lattice. In order to construct it, one has to choose a point of the reciprocal lattice, connect it with all the nearby points and bisect all the resultant vectors with planes (Figure 2.1). The volume defined by such planes around the original point is the first Brillouin zone.[4]

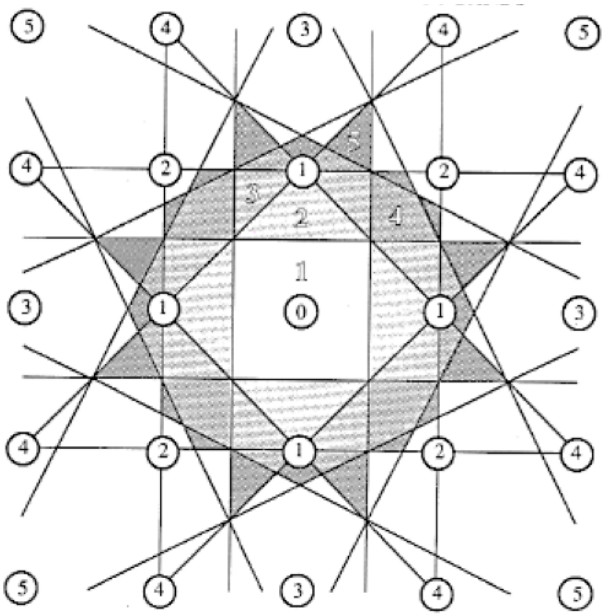

Figure 2.1. Brillouin zones of a simple square lattice. Circles represents the points of the reciprocal lattice and the numbers inside them identify the classification of the neighbors from the origin.[5] The first Brillouin zone is the white square around the point denoted with a number 0.

Despite reducing considerably the complexity of the system, in order to calculate the band structure of a solid one should take all (infinite) k points of the Brillouin zone,[4] which is impractical. In practice, what one can do is to study the structure of the band through special directions in the reciprocal space (high symmetry directions). These are the directions that will provide the structural characteristics of the system, while calculating the energy of the band for a finite set of points through each line. Usually, the calculation of properties such as the total energy of the system, which requires the calculation of all occupied crystal orbitals, is done by considering a finite lattice of k points in the Brillouin zone and to approach the integrals in the reciprocal space using sums on this finite lattice of k points. Calculations can be notably simplified by restricting them only to the irreducible part of the Brillouin zone, i.e., reciprocal space points from which the whole Brillouin zone can be obtained by application of non-translational symmetry operations (rotations and reflections) of the lattice.

Special high symmetry points in the Brillouin zone received specific names. The center of the zone is called Γ, and whatever other point is expressed as a fraction of the reciprocal vectors, this is, multiples of $2\pi/\vec{a}$.

2.5. Density of states

As has been mentioned before in this chapter, many atoms compose ~~the structure of~~ crystalline solids, which implies consideration of a large number of AOs per unit cell. Thus, analysis of their band structure is a difficult task. This is due to the fact that one has to choose one path of the infinite combinations existent in the Brillouin zone. Furthermore, BOs $\psi\left(r,k\right)$ can adopt complex values, which require assembling of linear combinations of such complex functions for producing real crystal orbitals for interpretation of their composition. Such combinations derive from the necessity of using the reciprocal space. Thus, it would be useful to have a tool that, despite the complexity of the system under study, allows the usage of the real space, when representing the obtained energies and analyze them in a simple manner.

A way of representing the whole electronic structure of the system is the density of states diagram (DOS). DOS, $P\left(E\right)$ is proportional to the inverse of the slope of the band

$$P\left(E\right)\approx\left(\frac{\partial E}{\partial k}\right)^{-1}. \tag{2.17}$$

The more pronounced the slope of the band, the less number of states will exist in a given range of k points and the lower the DOS will be or, equivalently, the flatter the band, the higher the DOS is.[4]

2.6. Density functional theory

In order to perform *ab initio* calculations for extended systems such as solids, there exist various ways of proceeding.

On one side, there exist methods consisting in solving the Schrödinger equation for determining the wave function of the system. One of the basic methods of this class is the Hartree-Fock method. It considers each electron independently of the others, being

only influenced by an effective potential created by all these electrons. Application of Hartree-Fock method results in an energy value always higher than the exact energy value of the system. Such energy difference is called correlation energy.

A way for (partial) overcoming the correlation energy problem is to calculate the energy of the system using the electron density $\rho(\vec{r})$. Usage of $\rho(\vec{r})$ to calculate the energy of the system is the dominion of the density functional theory (DFT).

The $\rho(\vec{r})$ is defined as the integral over the spin coordinates of all electrons and over all but one of the spatial variables

$$\rho(\vec{r}) = N \int \ldots \int \left|\Psi(\vec{x}_1, \vec{x}_2, \ldots, \vec{x}_N)\right|^2 \partial s_1 \partial \vec{x}_2 \ldots \partial \vec{x}_N \ . \tag{2.18}$$

$\rho(\vec{r})$ determines the probability of finding any of the N electrons within the volume $\partial \vec{r}$.

In 1927, Thomas and Fermi used a model based on the uniform electron gas for proposing a functional for the kinetic energy:

$$T_{TF}\left[\rho(\vec{r})\right] = \frac{3}{10}\left(3\pi^2\right)^{2/3} \int \rho^{5/3}(\vec{r}) \partial \vec{r} \ . \tag{2.19}$$

Using the classical expression for the nuclear-nuclear potential and electron-electron potential, one can obtain the energy of an atom in terms of the electron density:

$$E_{TF}\left[\rho(\vec{r})\right] = \frac{3}{10}\left(3\pi^2\right)^{2/3} \int \rho^{5/3}(\vec{r}) \partial \vec{r} - Z \int \frac{\rho(\vec{r})}{r} \partial \vec{r} + \frac{1}{2} \int \int \frac{\rho(\vec{r}_1)\rho(\vec{r}_2)}{r_{12}} \partial \vec{r}_1 \partial \vec{r}_2 \ . \tag{2.20}$$

To determine the density that has to be included in Equation (2.20) one can employ a variational principle, minimizing the energy under the constraint $\int \rho\left(\partial\vec{r}\right)\partial\vec{r} = \mathcal{N}$.

Hohenberg and Kohn provided demonstration that $\rho\left(\vec{r}\right)$ uniquely determines the Hamiltonian operator and, thus, all the properties of the system. The first Hohenberg-Kohn theorem states that *"the external potential* $V_{ext}\left(\vec{r}\right)$ *is (to within a constant) a unique functional of* $\rho\left(\vec{r}\right)$*; since, in turn* $V_{ext}\left(\vec{r}\right)$ *fixes* $\hat{H}$ *we see that the full many particle ground state is a unique functional of* $\rho\left(\vec{r}\right)$". Thus, $\rho\left(\vec{r}\right)$ determines $\mathcal{N}$ and $V_{ext}\left(\vec{r}\right)$ and hence all the properties of the ground state, such as the kinetic energy $T\left[\rho\right]$, the potential energy $V\left[\rho\right]$ and the total energy $E\left[\rho\right]$:

$$E\left[\rho\right] = \int \rho\left(\vec{r}\right)V_{NE}\left(\vec{r}\right)\partial\vec{r} + F_{HK}\left[\rho\right] \text{ , } F_{HK}\left[\rho\right] = T\left[\rho\right] + E_{ee} \text{ .} \qquad (2.21), (2.22)$$

If the functional $F_{HK}\left[\rho\right]$ was known, the Schrödinger equation could be solved exactly. Nevertheless, the form of kinetic energy $T\left[\rho\right]$ and electron-electron interaction E_{ee} terms are still unknown.

The second Hohenberg-Kohn theorem states that *"*$F_{HK}\left[\rho\right]$*, the functional that delivers the ground state energy of the system, delivers the lowest energy if and only if the input density is the true ground state density"*. As one can notice, this is an application of the variational principle:

$$E_0 \leq E\left[\tilde{\rho}\right] = T\left[\tilde{\rho}\right] + E_{Ne}\left[\tilde{\rho}\right] + E_{ee}\left[\tilde{\rho}\right] \text{ ,} \qquad (2.23)$$

This means that for any trial density $E\left[\tilde{\rho}\right]$ satisfying the necessary boundary conditions and associated with an external potential $\tilde{V}_{ext}$, the energy obtained in Equation (2.21) represents an upper bound to the true ground state energy E_0.

Even if the Thomas-Fermi model provides an example of DFT, its performance is really poor due to the approximation of the kinetic energy. Kohn and Sham addressed this problem in 1965 suggesting the calculation of the exact kinetic energy of a non-interacting reference system with the same density as the real interacting one

$$T_S = -\frac{1}{2}\sum_i^N \left\langle \psi_i \middle| \nabla^2 \middle| \psi_i \right\rangle , \tag{2.24}$$

where ψ_i are the orbitals of the non-interacting system. Note that T_S is not the real kinetic energy of the system. Kohn and Sham accounted for that with the introduction of the separation functional $F\left[\rho\right]$

$$F\left[\rho\right] = T_S\left[\rho\right] + J\left[\rho\right] + E_{XC}\left[\rho\right] , \tag{2.25}$$

where $E_{XC}\left[\rho\right]$ is the so-called exchange-correlation energy defined as

$$E_{XC}\left[\rho\right] \equiv \left(T\left[\rho\right] - T_S\left[\rho\right]\right) + \left(E_{ee}\left[\rho\right] - J\left[\rho\right]\right) . \tag{2.26}$$

$E_{XC}\left[\rho\right]$ is the functional that contains all unknown terms. The total energy of the system can be calculated as

$$E[\rho] = T_S[\rho] + J[\rho] + E_{XC}[\rho] + E_{Ne}[\rho] \ . \qquad (2.27)$$

The only term with no explicit form is $E_{XC}[\rho]$. Applying the variational principle, one obtains the Kohn-Sham equations:

$$\left(-\frac{1}{2}\nabla^2 + V_S(\vec{r}_1)\right)\psi_i = \varepsilon_i \psi_i \ , \qquad (2.28)$$

where the effective potential $V_S(\vec{r}_1)$ of a particle is

$$V_S(\vec{r}_1) = \int \frac{\rho(\vec{r}_2)}{r_{12}} \partial\vec{r}_2 + V_{XC}(\vec{r}_1) - V(\vec{r}_1) \ , \qquad (2.29)$$

which is formed by a Hartree-like potential, an exchange-correlation potential and the nuclei interaction potential.

Solving Kohn-Sham equations one obtains crystal orbitals (in the case of periodic systems) and their bands.[4]

DFT calculations are considered to be sufficiently correct as long as the exchange-correlation functional $E_{XC}[\rho]$ is approximated satisfactorily. The search for an appropriate $E_{XC}[\rho]$ for each system has derived two main approximations, the *local-density approximation* (LDA) and the *generalized gradient approximation* (GGA).

The $E_{XC}[\rho]$ functional obtained by applying the LDA is

$$E_{XC}^{LDA}\left[\rho\right] \equiv \int \rho\left(\vec{r}\right)\varepsilon_{XC}\left[\rho\left(\vec{r}\right)\right]\partial\vec{r} \ , \tag{2.30}$$

where ε_{XC} is the exchange-correlation energy for a particle of an homogeneous electron gas of density $\rho\left(\vec{r}\right)$. The exchange part can be expressed in an analytic manner, but the correlation part has to be derived from perturbational theory or interpolating a quantum Monte Carlo-like calculation for the electron gas.

This approximation is applicable for systems, electronic densities of which change smoothly from one to another point. It usually provides small exchange energies and high correlation energies.

The GGA exchange-correlation functional has the form

$$E_{XC}^{GGA}\left[\rho\right] \equiv \int \rho\left(\vec{r}\right)F\left\{\rho\left(\vec{r}\right),\nabla\rho\left(\vec{r}\right)\right\}\partial\vec{r} \ . \tag{2.31}$$

Unlike the LDA approach, GGA takes into account the gradient of the electron density in the development of the so-called gradient-corrected functionals. $\rho\left(\vec{r}\right)$ and the gradient $\nabla\rho\left(\vec{r}\right)$ are included for a better description of the exchange energy in regions of low electron density. Resulting calculated energies are much better than the ones obtained using LDA), especially when treating systems with bond dissociation or formation, so as often better geometries (with many known exceptions).

Despite LDA and GGA approaches are useful for approximating exchange-correlation energies, they are not sufficiently accurate, when the correlation energy is high. For instance, their application for describing metal-oxide isolators, such as ceria, results in metallic-like electronic structures. There exist various ways for solving problems like that, even if these computational techniques are much more demanding and cannot be applied to solids with complicated crystalline structures. A simple approximate method for dealing with such problems is the inclusion of an extra repulsion term, the so-called Hubbard parameter *U*, which gives rise to the LDA+*U* and

GGA+*U* methods. Such parameter is commonly used for treating in *ad hoc* fashion the Coulombic repulsion between *d* or *f* electrons, but it can be applied to whatever type of orbitals. The energy functional will be dependent on the electron density and on the occupation matrix, since the *U* parameter is a basic variable needed to be considered inside the matrix. The choice of the *U* value allowing to sufficiently accurately describe all kinds of calculated observables for a given system often is not possible.[4]

2.7. Plane waves and pseudopotentials

As mentioned in previous sections of the present chapter, orbitals or bands are usually represented as linear combinations of functions in order to allow improved performance of calculations. For a proper description of periodic systems, it is common to use plane wave functions as basis sets. Such functions are not centered at nuclei, as Gaussian-type orbitals are, but are extended throughout the entire cell. Plane waves take implicitly into account the periodic boundary conditions of the system, making them particularly appropriate for calculations of extended systems. Despite the large number of plane wave functions is required to achieve desired accuracy, by using pseudopotentials one can reduce the number of these functions significantly.

Pseudopotentials are an effective way of treating core electrons of heavy atoms in systems dealing with many electrons. Core electrons are considered unmodified during the calculation with only valence electrons determining chemical properties of solids.

An efficient way of combining the pseudopotential approximation with plane waves is the Projector Augmented Wave method (PAW) proposed by Blöchl.[6] The core electrons are treated as frozen functions. Then, a smooth part of a wave function and a linear transformation relating valence functions of core electrons can be defined to these smooth functions.

2.8 References

(1) Kresse, G.; Hafner, J. Ab Initio Molecular Dynamics for Liquid Metals. *Phys. Rev. B* **1993**, *47*, 558–561.

(2) Kresse, G.; Furthmüller, J. Efficiency of Ab-Initio Total Energy Calculations for Metals and Semiconductors Using a Plane-Wave Basis Set. *Comput. Mater. Sci.* **1996**, *6*, 15–50.

(3) Kresse, G.; Furthmüller, J. Efficient Iterative Schemes for Ab Initio Total-Energy Calculations Using a Plane-Wave Basis Set. *Phys. Rev. B* **1996**, *54*, 11169–11186

4) Dronskowski, R. *Computational Chemistry of Solid State Materials*; Wiley-VCH, 2005.

(5) Altmann, S. L. *Band Theory of Solids: An Introduction from the Point of View of Symmetry*; Oxford Science Publications, 1991.

(6) Blöchl, P. E. Projector Augmented-Wave Method. *Phys. Rev. B* **1994**, *50*, 17953–17979.

CHAPTER THREE

On the stability of single transition metal atoms adsorbed on ceria nanoparticles

3.1. Introduction

In the present chapter we tackle a rather new strategy in catalysis science with the aim of reducing the noble metal content in catalytic materials. This saving measure is nowadays an urgent need due to the ever-increasing demand for such metals from the automobile industry along with their limited supply. These circumstances have a critical effect on the price of noble metals and, therefore, on the large-scale implementation of applications that require noble-metal-based catalysts.[1-3]

In order to deal with this problem, two different strategies can be followed. The first one involves the partial or total replacement of the precious metal by other less-expensive materials. In this line, a wide number of alternatives have been already proposed, which can indeed substantially decrease the cost of the catalyst.[4-6] Nevertheless, the catalytic performance of these alternatives is rather inferior to the one obtained using the analogous noble-metal systems. The other strategy aims for a more efficient utilization of the noble metal content present in the catalyst. This can be obtained by maximizing the specific catalytic performance of the noble-metal phase, *i.e.* its per-atom activity. The latter has been usually achieved by finely dispersing the noble metal on the support material.[7,8]

The extreme situation of metal dispersion corresponds to catalysts where the active metal is distributed on the surface of the support in the form of atomic species, denoted as SACs.[9,10,11] However, non-reducible metal-oxide supports exposing regular surfaces, such as MgO(100),[12] anchor atomic transition metal species too weakly to prevent their clustering. Even regular (111) surface of widely applicable archetypical reducible oxide CeO_2 binds on it transition metal atoms only rather weakly.[13] These are indications that the preparation of sufficiently stable transition metal SACs requires special conditions, such as exposing of strongly binding sites on the supports to counteract aggregation of metal atoms in particles thermodynamically strongly triggered by metal-metal bond formation.

Various composites exposing surface metal atoms were shown to be catalytically active for a wide range of chemical reactions. For instance, atomic Pt and Au species supported on nanostructured ceria[14] and other more inert oxides[15,16] were found to

catalyze the industrially important water-gas shift reaction at low temperatures. Moreover, materials with Pd cations anchored on alumina[17] and surface Pt cations on FeO_x[18] were demonstrated to be active towards CO oxidation. SACs containing Pd atoms anchored to cavities of mesoporous graphitic carbon nitride[19] and FeO_x-supported Pt[20] have been found to be also highly active in mediating hydrogenation reactions. These and analogous systems represent a very promising and interesting new generation of cost-effective catalytic materials.

According to the existing literature, supported noble-metal atoms in oxidized states are the active species in these catalysts. It is worth mentioning, however, that SACs can partly lose the specific activity of the metal due to sintering or bulk diffusion under the harsh catalytic conditions. These processes may strongly reduce the number of active metal sites exposed to reactants at the surface of the support. Therefore, it is essential that the support provides enough surface sites able to anchor the single metal atoms with sufficient strength to prevent undesired processes of their agglomeration and bulk diffusion.

To this end, small {100} facets of NPs have been shown to be remarkably efficient in anchoring single Pt atoms in the form of cationic Pt^{2+}.[21,22] Furthermore, combination of DF calculations with X-ray photoelectron spectroscopy (XPS) experiments successfully determined the presence of Pt^{2+} cations adsorbed on these special surface sites exposing four nearby O anions arranged as a square. There, cationic Pt is efficiently protected form reduction, aggregation, and bulk diffusion, even up to high temperatures (around 700 K).[21] Thus, both theoretical and experimental evidences imply that this specific nanofacet fulfills the requirements for preparation of a sufficiently stable SAC. Notably, this O_4 surface site is not inherent solely to ceria NPs, but it can also be found on extended $CeO_2(100)$ surfaces[23] and on the step edges of low-energy $CeO_2(111)$ islands.[24]

The findings regarding the extraordinary stability of Pt atoms on ceria {100} nanofacets suggest that these sites may not only strongly bind Pt, but also other transition metal atoms. To asses this peculiar binding propensity, key factor for synthesizing stable SACs, we computationally investigated the interaction of {100} facet sites of ceria NPs with other transition metal atoms M = Fe, Ru, Os, Co, Rh, Ir, Ni, Pd, Cu, Ag, and Au of groups VIII-XI of the periodic table. In the following, we provide extensive comparison

and analysis of the adsorption energies of the atomic M_1 species on this ceria site with the binding energies of the corresponding atoms in metal NPs.

3.2. Models

As a representative model of nanostructured CeO_2, a cuboctahedral $Ce_{40}O_{80}$ NP has been chosen (Figure 3.1). This model is shown to be capable of reproducing various experimental observations.[21,25,26] The structure of this NP resulted from global optimization using interionic potentials and DF calculations.[27,28] The $Ce_{40}O_{80}$ NP retains the cubic fluorite-type crystallinity of bulk CeO_2 and exposes small O-terminated {111} and {100} facets. The latter corresponds to the polar (100) surface, which is known to be less stable than the (111) surface.[29] Nevertheless, nanostructured ceria with numerous {100} terminations have also been prepared, ranging from nanocrystals with extended (100) terraces[23] to nanocubes exposing only {100} facets.[30] To avoid in our calculations significant spurious interactions of the ceria NPs with each other, the size of the periodically repeated unit cell was chosen to keep distances between NPs in neighboring cells ≥700 pm.

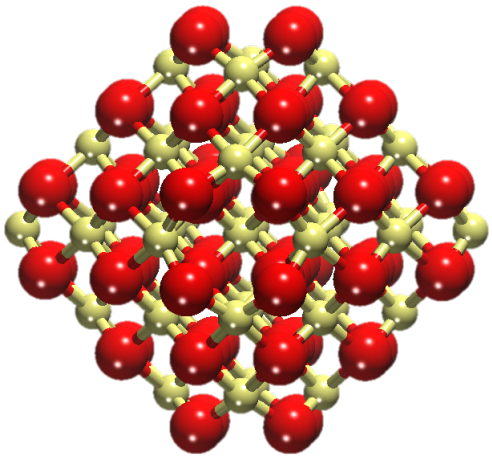

Figure 3.1. Cuboctahedral $Ce_{40}O_{80}$ nanoparticle model of nanostructured ceria. Yellow and red spheres represent Ce^{4+} and O^{2-} ions, respectively.

Adsorption energies, E_{ad}, of a metal atom M on the ceria NP have been calculated as $E_{ad} = E(M_1\text{-}Ce_{40}O_{80}) - E(M_1) - E(Ce_{40}O_{80})$, where $E(M_1)$ is the total ground-state energy of an isolated metal atom and $E(M_1\text{-}Ce_{40}O_{80})$ and $E(Ce_{40}O_{80})$ are the total energies of the ceria NP with and without the adsorbed metal atom, respectively. Negative E_{ad} values correspond to stabilizing interactions with respect the separated M_1 and $Ce_{40}O_{80}$ fragments. In order to compare the strength of this interaction with that of

M_1 agglomeration into metal particles M_n, we have calculated the binding energy, E_{ad79}, of an edge M atom in the M_{79} model as $E_{ad79} = E(M_{79}) - E(M_1) - E(M_{78})$. This M_{79} particle is a bulk cut of the *fcc* crystal (Figure 3.2).

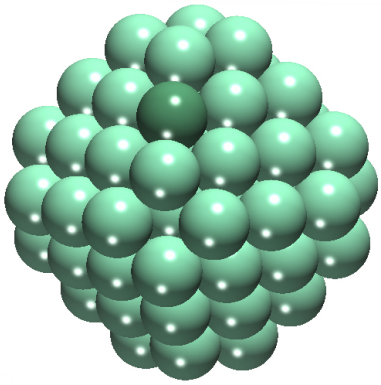

Figure 3.2. Model M_{79} NP used for estimating the binding energy of atoms in metal particles. The darker green M atom in the edge position was removed for calculating its binding energy to the remaining M_{78} species.

3.3. Results and discussion

In the following section, we perform a comparative study of the adsorption of 3d (Fe, Co, Ni, Cu), 4d (Ru, Rh, Pd, Ag), and 5d (Os, Ir, Pt,[21] Au) metal atoms on the O_4 sites of {100} nanofacets of the $Ce_{40}O_{80}$ NP. It is worth mentioning that this is not the only site on the chosen NP, where metal atoms can or may be anchored, but the adsorption of Pt on other NP sites was calculated to be much weaker than on the O_4 site,[21,22] similar in strength to the rather weak adsorption on CeO_2(111) surfaces.[31] Therefore, we focused on interactions with the O_4 site, since we expect all metal atoms under scrutiny to prefer this site for adsorption.

Optimized structures of M_1-$Ce_{40}O_{80}$ systems are shown in Figure 3.3. Using spin moment analysis, we are able to quantify the amount of charge transfer upon deposition of metal atoms on the {100} nanofacet. Such charge transfer induces the oxidation of the M_1 adsorbate concomitant with the reduction of a certain number of Ce^{4+} cations to Ce^{3+}. This number depends on the specific M atom and equals its oxidation state. Corner Ce^{4+} cations in the $Ce_{40}O_{80}$ NP are the most prone to be reduced. This is due to their lower coordination number and more open location on the surface of the NP, which results in an accordingly less destabilizing electrostatic environment.[27,32] Corner Ce^{4+} cations accept electrons from M atoms, which are oxidized to cations in the +1 or +2 oxidation states. In situations where the M center suffers further oxidation, a search for the most stable locations of the additionally formed Ce^{3+} cations has not been performed in view of the enormous number of possible configurations needed to be tested. Location of Ce^{3+} cations in other positions of the ceria NP is estimated to modify adsorption energy of the M atom to the O_4 site by up to 40 kJ mol^{-1} per Ce^{3+} cation.[27] But even this moderately strong energy difference should not critically affect the upcoming discussion of E_{ad} values of M atoms. Note that the formation of Ce^{3+} cations (which are larger than Ce^{4+} cations) noticeably elongates the corresponding Ce-O distances, to 228 pm from 213 pm in the pristine CeO_2 NP.

Next, we discuss the calculated oxidation states for each adsorbed metal atom and M-O coordination modes. Comments on how our results compare to pertinent experimental data are also provided.

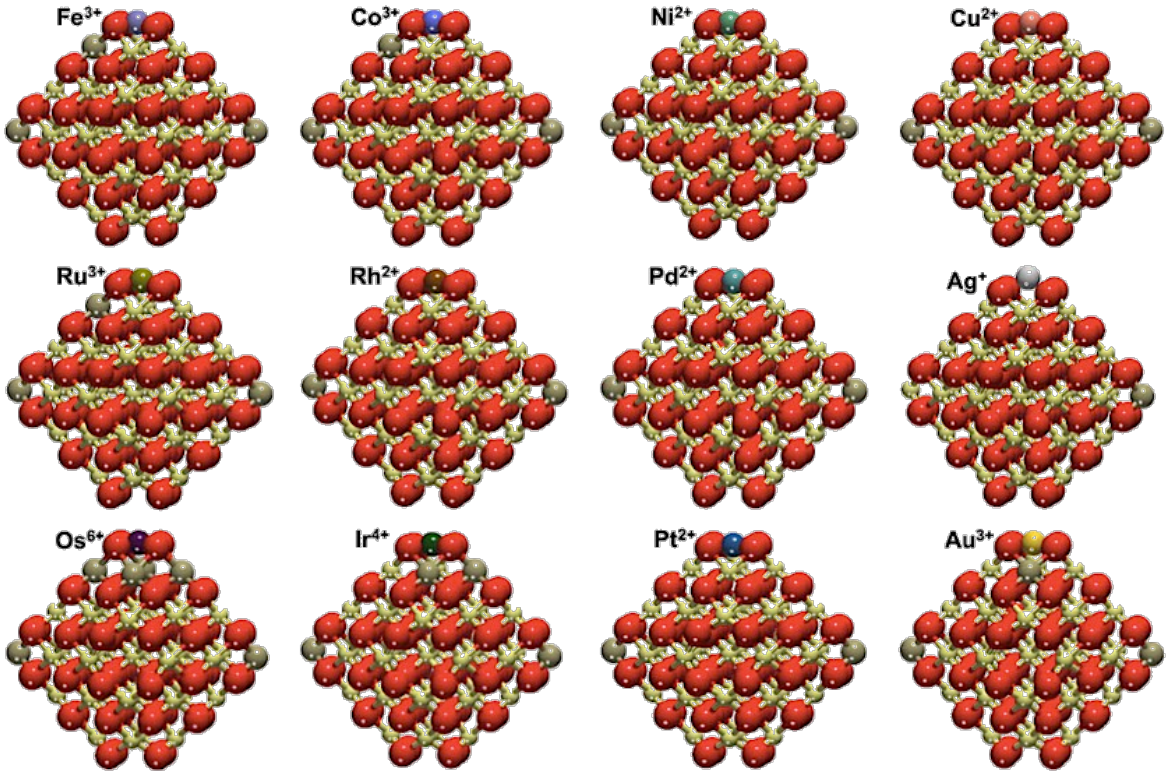

Figure 3.3. Overview of the M_1-$Ce_{40}O_{80}$ structures calculated for the adsorption of different transition metal atoms (M) on the {100} facet of the $Ce_{40}O_{80}$ nanoparticle. Yellow, brown, and red spheres represent Ce^{4+}, Ce^{3+}, and O^{2-} ions, respectively.

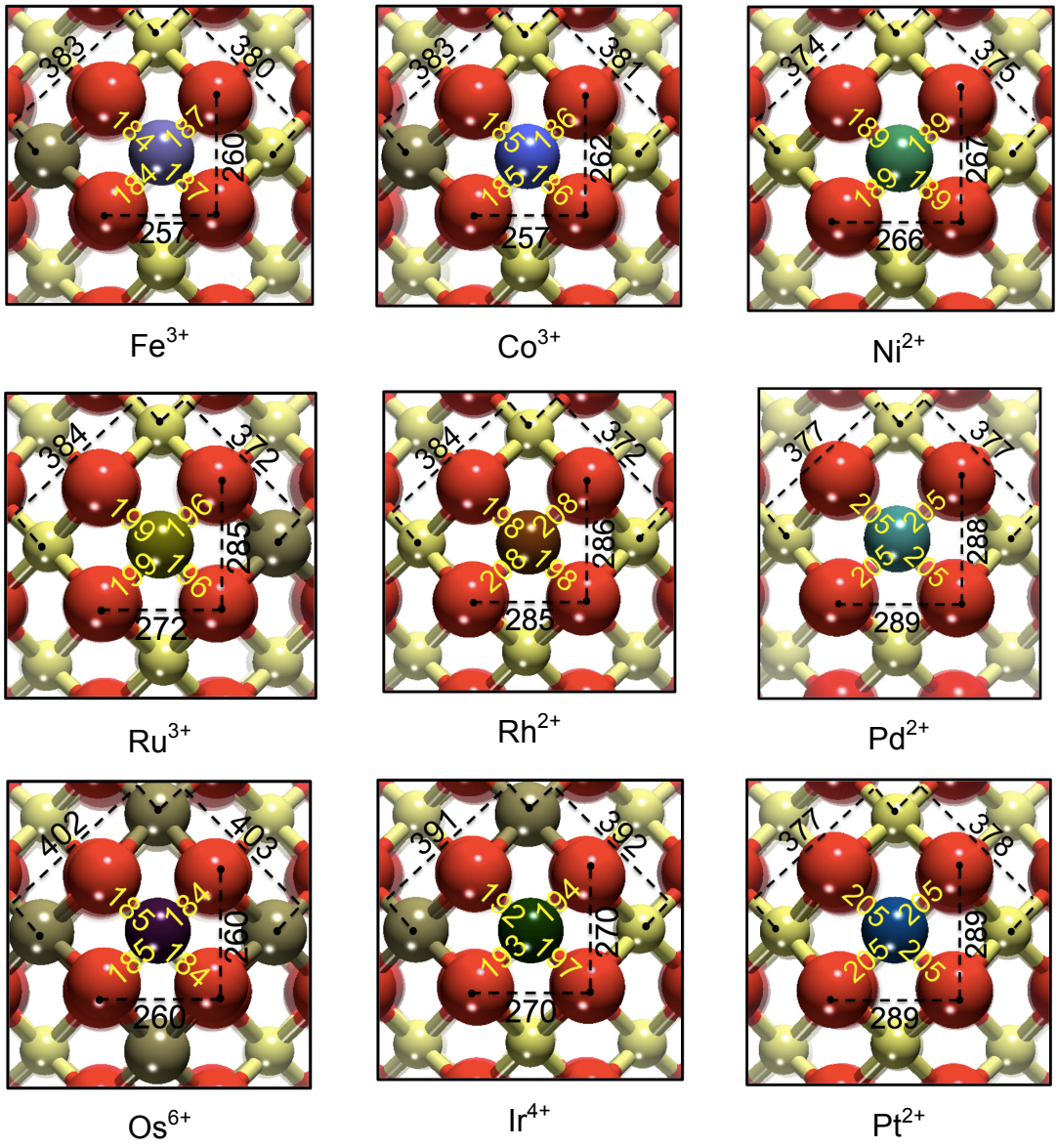

Figure 3.4. Representative M-O, O-O, and Ce-Ce distances (pm) at the {100} facet of the NP with adsorbed M atoms of the 8th, 9th, and 10th group of the periodic table.

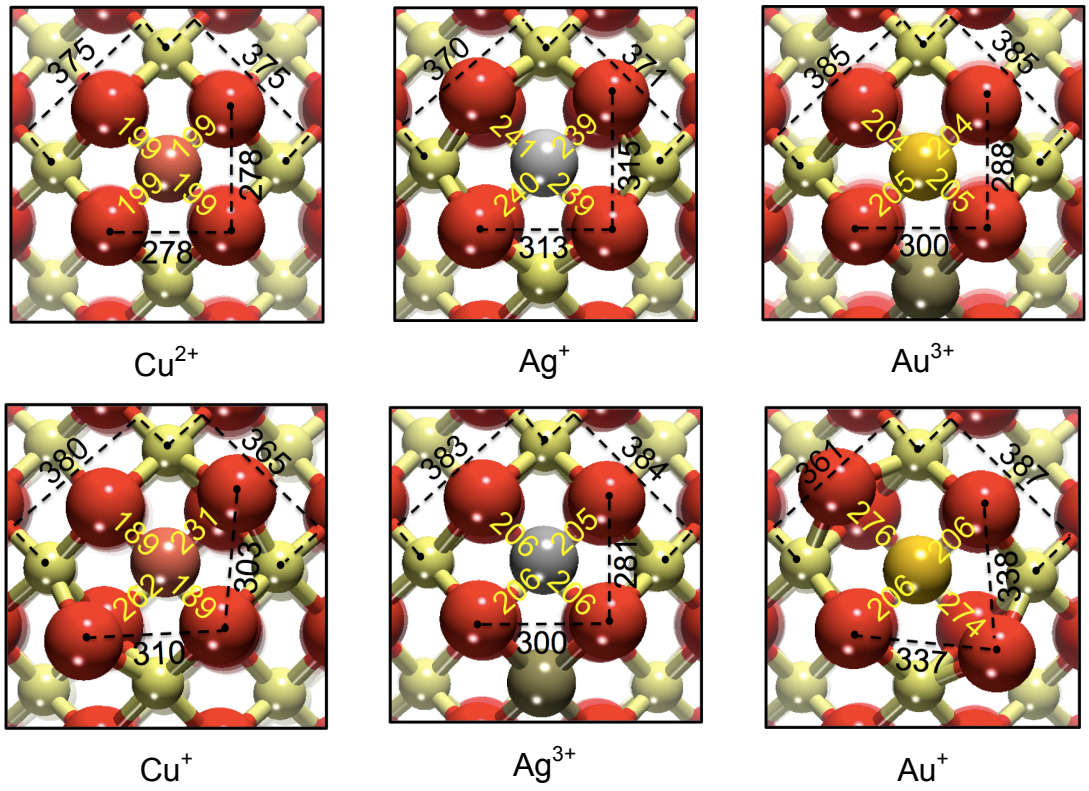

Figure 3.5. M-O, O-O, and Ce-Ce distances (pm) at the {100} facet of the ceria NP with M = Cu, Ag, and Au atoms adsorbed considering their two possible oxidation states. Top images represent the most stable states obtained.

Group VIII metals

Transition metal atoms of group VIII are calculated to feature different oxidation states, +3 for Fe and Ru, and +6 for Os. Two Ce^{3+} cations are located in corner positions, with additional f electrons on other surface Ce^{3+} cations close to the {100} site occupied by M. The M atoms are bound to four atoms of the O_4 site arranged in a square-planar fashion. The nearest M-O distances are 184-187 pm for Fe, 196-199 pm for Ru, and 184-185 pm for Os. These distances are much shorter than the distance of *ca.* 225 pm between the O atoms and the center of the O_4 square in the pristine $Ce_{40}O_{80}$ NP.[21] Mössbauer spectroscopy detected Fe^{3+} cations coordinated by four O anions in a similar mode when inserted into the lattice of ceria-zirconia catalysts.[33] Additionally, self-dispersed Ru metal powder on ceria in the form of small particles and single atoms in a highly oxidized state was also demonstrated to be very stable at high temperatures by X-ray absorption near edge structure (XANES) and Raman spectroscopies.[34]

Group IX metals

Atoms of this group manifested quite diverse oxidation states. Co is the only group IX metal atom adsorbed on the ceria NP that features a +3 state. We calculated Ru to be adsorbed in the +2 state. Similar to atoms of group VIII, only the 5d element, in this case Ir, undergoes further oxidation to the +4 state. As for the NP with adsorbed group VIII atoms, Ce^{3+} cations are formed in both corner positions and close to the O_4 site occupied by the metal. Co and Ir are bound in a square-planar coordination mode with M-O distances 185-186 pm for Co and 192-197 pm for Ir. Rh^{2+} appears to prefer a linear coordination with two short (198 pm) and two long distances (208 pm). Group IX cationic species have been characterized experimentally on ceria-based materials. Co^{3+} cations were detected using temperature-programmed reduction (TPR) and XPS experiments in ceria-zirconia catalysts.[35] Rh^{2+} cations were evidenced on ceria-zirconia mixed oxides by Fourier transform infrared (FTIR) spectroscopy.[36] Finally, surface Ir^{4+} species were identified in ceria by TPR and diffuse reflectance infrared Fourier transform spectroscopy (DRIFTS).[37]

Group X metals

Group X atoms Ni and Pd are calculated to be adsorbed similarly to Pt as +2 cations, coordinated in a square-planar mode, which is very characteristic of d^8 metals. The interatomic M-O distances are 189 pm for Ni and 205 pm for both Pd and Pt. The same oxidation state was recently reported for Ni^{2+} on defect sites of $CeO_2(111)$ surface.[38] It was shown that the interaction of Pd with ceria can lead to the formation of Pd-O-Ce surface structures featuring Pd^{2+} cations, which are highly active in the catalytic combustion of methane.[39] There is experimental evidence that Pd^{2+} cations in the square-planar coordination by oxygen are highly stable in PdO_x-CeO_2 solid solutions.[40] The presence of atomic platinum as Pt^{2+} cations on ceria surfaces has already been documented by several theoretical and experimental studies. Formation of these species was often related to exposure of (100)-terminated facets.[21,22,41-43]

Group XI metals

Adsorbed atoms of group XI, like those of group IX, exhibit various oxidation states. Moreover, each adsorbed group XI atom can feature different oxidation states. The presence of Cu as Cu^{2+} ions in the ceria lattice was reported recently.[44] We calculated Cu^{+} to be coordinated in a distorted linear fashion with two short (189 pm) and two long Cu-O distances (231 and 262 pm). Cu^{2+} adsorbs in a square-planar coordination mode with four equal Cu-O distances (199 pm). The Cu^{2+} state is found to be 54 kJ mol^{-1} more stable than the Cu^{+} state (Table 3.1). Atomic Ag can be adsorbed as either Ag^{+} or Ag^{3+}, the latter being somewhat more stable. The not very common Ag^{3+} binds to four O atoms, with Ag-O distances of 205-206 pm, in line with the square-planar coordination detected in oxoargentates.[45] Ag^{+} prefers a notably distorted square-planar coordination, where the metal atom is around 90 pm above the O_4 plane. This distortion elongates Ag-O distances to 239-241 pm. Atomic Au can also be adsorbed in two different oxidation states, +1 and +3, the latter being 70 kJ mol^{-1} more stable (Table 3.1). Au, similar to the other studied 5d metals, forms the highest oxidation state (+3) within the group. A linear coordination of Au^{+} cations is preferred, with two short (206 pm) and two long distances (274 and 276 pm), while Au^{3+} prefers a square-planar coordination (Au-O distances are 204-205 pm). Ag adsorbed as single atoms on microporous hollandite manganese oxide was found by XANES to feature the +1 oxidation state.[46] Meanwhile, gold can be stabilized both as Au^{3+} and Au^{+} surface cations in ceria-supported gold catalysts.[47]

M	E_{ad}, kJ mol^{-1}	E_{ad79}, kJ mol^{-1}	E_{ad79}-E_{ad}, kJ mol^{-1}	q, a.u.
Group VIII				
Fe^{3+}	-785	-630	155	1.50
Ru^{3+}	-812	-729	83	1.46
Os^{6+}	-978	-844	134	2.49
Group IX				
Co^{3+}	-709	-548	161	1.29
Rh^{2+}	-678	-612	66	1.07
Ir^{4+}	-830	-821	9	1.54
Group X				
Ni^{2+}	-678	-519	159	1.06
Pd^{2+}	-504	-377	127	0.91

Pt^{2+}	-678	-548	130	0.93
Group XI				
Cu^{+}	-412			0.73
Cu^{2+}	-466	-371	95	1.03
Ag^{+}	-277	-263	14	0.63
Ag^{3+}	-251			1.06
Au^{+}	-264			0.41
Au^{3+}	-334	-310	24	1.08

Table 3.1. Calculated adsorption energies E_{ad} and Bader charges q for atoms M adsorbed as M^{n+} cations on a $Ce_{40}O_{80}$ NP along with binding energies E_{ad79} of the M atoms on edges of M_{79} NPs (see Fig. 3.2).

The adsorption energy values shown in Table 3.1 indicate that the ceria {100} nanofacet can strongly anchor not only atomic Pt, but other transition metal atoms as well. Atoms of all considered transition metals are oxidized upon adsorption on the O_4 site. Bader charge analysis of adsorbed species reflects the formal oxidation states only qualitatively, being notably smaller than the latter and, interestingly, manifesting significant covalence contribution in the M-O interactions. Despite the simplicity of the considered O_4 sites exposed by the $Ce_{40}O_{80}$ NP, we expect them to be representative for a wide variety of experimental environments of different coordinated transition metal cations. Specially, our model ceria NP allows us to quantify the strength of the M-O(-Ce) bonds formed by the oxidized metal atoms. To assess whether these atomic metal species are resistant or not to undesired agglomeration and sintering processes, which is crucial issue in the design of SACs, we compared binding energies of the metal atoms on the ceria NP surface and in the corresponding M_{79} NPs (Table 3.1).

For all M atoms under scrutiny, the adsorption energy E_{ad} on the ceria NP is larger in magnitude (i.e., more negative) than the binding energy E_{ad79} of an edge atom located in the M_{79} NP. This implies that the metal dispersion as single atoms on the O_4 sites of ceria nanostructures is energetically favored with respect to the formation of metallic aggregates. Thus, the resistance to sintering processes can be expected for very stable adsorption complexes on the nanoparticulate oxide support, especially for metals

featuring substantial energy differences $\Delta E = E_{ad79} - E_{ad}$ (Table 3.1). The ΔE value is a direct measure of the propensity of anchored metal atoms to form particles: the larger ΔE value, the less prone the metal center is to undergo sintering and aggregation. At the light of these results, we predict Fe^{3+}, Os^{6+}, Co^{3+} and all group X metals to be particularly resistant to agglomeration, especially in oxidative media. For group X metals, the extraordinary stability of the square-planar coordination characteristic of d^8 metal centers explains the particularly strong interaction with the support NP. Small ΔE values calculated for cationic Ag, Au, and Ir species suggest that these complexes are less resistant to sintering and, therefore, might form metallic particles more easily than the other ones. Perhaps, to better stabilize these metals as single atoms one should explore other, more strongly binding supporting materials. The O_4 sites of CeO_2 nanostructures (not limited only to $Ce_{40}O_{80}$ NPs) bind metal atoms notably stronger than on the extended $CeO_2(111)$ surface. For instance, the adsorption of Cu, Ag, and Au atoms on the latter surface resulted in PW91+3 E_{ad} values of -179, -96, and -69 kJ mol^{-1}, respectively.[48] This greatly suggests that the adsorption complexes of transition metal atoms on {100} facets of CeO_2 NPs are substantially more resistant to agglomeration processes than on the $CeO_2(111)$ surface. We believe that since Pt was found to adsorb on both {100} facets and other non-{100} sites of the ceria NP with comparably much lower E_{ad},[21] other metals will behave similarly.

A closer look at the results in Table 3.1 reveals clear trends in calculated adsorption energies along the rows and groups of the periodic table (Fig. 3.6). The two adsorption energy values E_{ad} and E_{ad79} generally decrease in magnitude when moving from the left to the right of the period. This is an indication that metals with less occupied d bands form stronger metal-metal bonds, which are therefore more strongly bound as atoms to the oxide support. Monotonous decreases in E_{ad} and E_{ad79} values are observed for 4d and 5d metals, with more pronounced differences for Au. The trend along the period for 3d metals is less linear and both E_{ad} and E_{ad79} values are crossed with those of the 4d and 5d metals. These data also indicate that, except for Au, 5d metals form the strongest bonds with the O_4 site of the ceria NP, whereas 4d metals form the weakest bonds, with the exception of Ru.

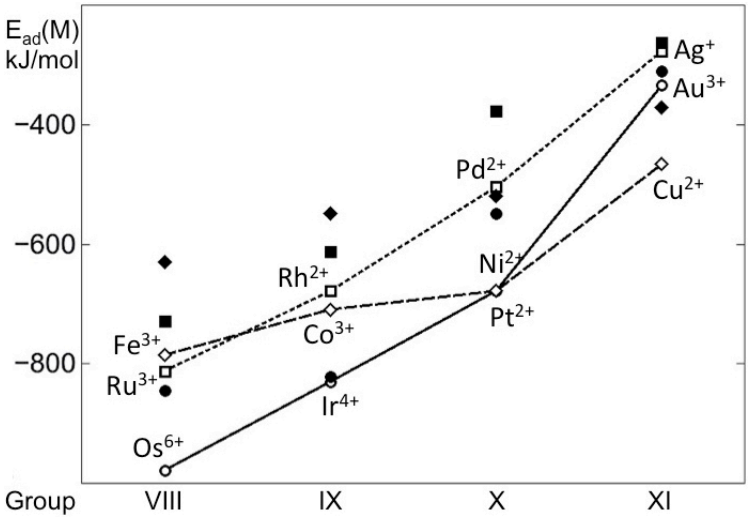

Figure 3.6. Adsorption energies of transition metal atoms (M) on the {100} facet of the $Ce_{40}O_{80}$ NP (empty points, connected as a guide for the eye) and binding energies of these atoms in edge positions of the M_{79} NP depicted in Fig. 3.2 (filled points). Results for 3d, 4d, and 5d metals are shown by diamonds, squares, and circles, respectively.

It is important to mention that the transformation of the transition metal content into the corresponding oxide phase in an oxidative environment could lead to the destruction of the single-atom sites. Similar to the sintering into metal particles, the formation of the oxide phase would lead to a decreased number of exposed metal atoms, which may change the surface properties of the catalytic material and the local environment of the metal center. The propensity of the single-atom sites to do such restructuring can be assessed by analyzing the experimental standard heats of formation ($\Delta_f H$) for the most stable oxide phases of the metals under study (Table 3.2). In general, 3d metals are more prone to form oxide phases than (more noble) 4d and 5d metals, with oxides of metals from the beginning of the period being more stable than those from the end of the period.[49] Comparing E_{ad} and $\Delta_f H$ values for each transition metal one can expect generally higher resistance against decomposition via the formation of a metal oxide phase except for Fe, which is quite susceptible to oxide formation.

Group VIII		Group IX		Group X		Group XI	
-825.5	Fe_2O_3	-237.5	CoO	-244.3	NiO	-175.3	CuO
-314.8	RuO_2	-405.5	Rh_2O_3	-118.6	PdO	-29.0	Ag_2O
-291.8	OsO_2	-249.5	IrO_2	-80.0	PtO	-13.0	Au_2O_3

Table 3.2. Experimental standard heats of formation $\Delta_f H$ (kJ mol^{-1}) of the most stable oxides of metals M[50,51] studied in Chapter 3.

All results presented in this chapter correspond only to stoichiometric ceria NPs, which are most relevant to UHV conditions or to conditions with low oxygen pressure.[22] Nevertheless, under ambient atmosphere and oxidative catalytic conditions ceria NPs can be stabilized by an excess of oxygen.[52-54] In those environments, a variety of oxygen-containing surface species can create additional adsorption sites eventually capable of stabilizing oxidized transition metal atoms as potential SACs. We expect the binding properties of such sites to be quite similar to those of the sites on the {100} O-terminated faces of the stoichiometric NPs. This assumption is supported by the finding that oxygen atoms on the {100} O_4 sites are loosely bound to ceria NPs,[55,27] which is reminiscent to the binding of the species adsorbed on the NP faces under excess O_2. Therefore, the present theoretical prediction that surface oxygen sites of nanostructured ceria are able to make diverse single-atom metal catalysts resistant to sintering probably can also be generalized to other experimental conditions.

The above results regarding the extreme stability of supported single metal atoms are expected to provide a guideline establishing suitable candidates for the design of SACs. These results may open a novel way to analyze the catalytic function of the proposed catalytic materials individually for each reaction of interest. Following this line, co-sputtering of transition metals under oxygen atmosphere, which allows preparing nanocomposites of atomically dispersed Pt on ceria,[21,56] can also be used to disperse other metals, atoms of which are strongly bound to the O_4 sites.

This has been experimentally demonstrated for model catalysts prepared according to the guidelines provided by the present calculations and comparing the stability and reactivity of Pt^{2+}, Pd^{2+}, and Ni^{2+} species on nanostructured ceria.[57] All three metals

exhibit adsorption energies on the ceria NP exceeding in magnitude the bulk cohesive energies (see Table 3.3). This fact supports the previously mentioned hypothesis: once anchored to the {100} facets of stoichiometric ceria, all 12 studied metal atoms are stable with respect to formation of metallic NPs. Nevertheless, for reduced ceria NPs, the adsorption at the nanofacet sites is expected to weaken and eventually enable formation of supported metallic aggregates.[21,58] Following this line, it is noteworthy that for Pd even with a lower calculated E_{ad} difference of 174 kJ mol^{-1} with respect to E_{ad} value of Pt (see Table 3.1), similar stability to that of the latter is expected due to a higher E_{coh} difference of 190 kJ mol^{-1} (see Table 3.3), which compensates the lower adsorption propensity. Ni seems to show a somewhat different behavior. Whereas the adsorption energy of atomic Ni at the square oxygen pocket sites is identical to that of Pt (-678 kJ mol^{-1}), the E_{coh} value of metallic Ni (-428 kJ mol^{-1}) is much lower than that of Pt (-564 kJ mol^{-1}). Thus, a strong disfavor in the formation of metallic Ni particles from the adsorbed Ni^{2+} species is expected. Nevertheless, the larger $\Delta_f H$ for NiO in comparison to that for PtO_2 and PdO (see Table 3.2) may favor the formation of nickel oxide phases even on strongly reduced catalysts films.

Group VIII		Group IX		Group X		Group XI	
-413	Fe	-424	Co	-428	Ni	-336	Cu
-650	Ru	-554	Rh	-376	Pd	-284	Ag
-788	Os	-670	Ir	-564	Pt	-368	Au

Table 3.3. Experimental cohesive energies E_{coh} (kJ mol^{-1}) for metals M.[59]

Certain types of steps on CeO_2(111) surface[24,60] also appear to efficiently anchor Pt^{2+} by forming PtO_4 moieties, indicating that the preparation of ceria surfaces with very abundant steps also facilitates metal dispersion in the form of atoms.[61] In addition, the detailed structural data calculated in this work (*e.g.* metal coordination and metal-oxygen distances, see Fig. 3.4 and 3.5) provide a benchmark for the characterization of atomically dispersed metal sites in SACs supported on nanostructured ceria. For example, Pt coordination number and Pt-O bond length measured by means of extended X-ray absorption fine structure (EXAFS)[41] experiments fully agree with the calculated

structure of Pt^{2+} on the {100} sites of ceria NPs.[21,22] Another implication of the present findings for nanocatalysts is related to the ability of some M_1-ceria SACs to undergo agglomeration and re-dispersion cycles under certain reaction conditions, forming metal clusters during the reaction and re-dispersing to the M_1-ceria state upon termination of the reaction.[62] The estimated notable stability $\Delta E = E_{ad79} - E_{ad}$ of the M_1-ceria materials with respect to the agglomeration into metal clusters (Table 3.1) controls that clusters remain small enough (possibly, sub-nano) and can readily transform back into single-atom species.

3.4. Overview

The interaction of 12 different transition metal atoms M = Fe, Ru, Os, Co, Rh, Ir, Ni, Pt, Pd, Cu, Ag, and Au with a $Ce_{40}O_{80}$ NP has been computationally studied in this chapter. Specific adsorption sites of ceria, the {100} nanofacets, can very effectively anchor all considered metal atoms in the form of M^{n+} cations. The oxidation of the M centers takes place with the concomitant reduction of n Ce^{4+} cations to Ce^{3+} ones. Our calculated data indicate that higher oxidation states are favored by transition metals in later periods and in groups more to the left side of the periodic table. The deposition of the M atoms leads to a significant structural reconstruction of the oxygen atoms constituting the adsorption site, which coordinate differently to the M^{n+} cation depending on its oxidation state.

Importantly, the adsorption in each M_1-ceria system under study is stronger than the binding of the corresponding M atom in a metal NP M_{79}. These energy differences are particularly large for the group X metals (Ni, Pd, and Pt) and for Fe, Co, and Os. This suggests that, especially for these metals, CeO_2-based materials exposing O_4 sites such as those on {100} nanofacets could provide suitable architectures for preparing single metal atom catalysts with very high resistance to sintering.

In general, the present calculated results are expected to be helpful in guiding the preparation and for the atomic-level characterization of efficient single-atom catalysts, the limiting case in nanocatalysis featuring the smallest active species.

3.5. References

(1) Tollefson, J. Worth Its Weight in Platinum. *Nature* **2007**, *450*, 334–335.

(2) Vielstich, W.; Lamm, A.; Gasteiger, H. A. *Handbook of Fuel Cells: Fundamentals, Technology, Applications*; Wiley: Chichester, 2013.

(3) Stamenkovic, V. R.; Mun, B. S.; Arenz, M.; Mayrhofer, K. J. J.; Lucas, C. A.; Wang, G. F.; Ross, P. N.; Markovic, N. M. Trends in Electrocatalysis on Extended and Nanoscale Pt-Bimetallic Alloy Surfaces. *Nat. Mater.* **2007**, *6*, 241–247.

(4) Chung, H. T.; Won, J. H.; Zelenay, P. Active and Stable Carbon Nanotube/nanoparticle Composite Electrocatalyst for Oxygen Reduction. *Nat. Commun.* **2013**, *4*, 1922.

(5) Yang, W.; Fellinger, T. P.; Antonietti, M. Efficient Metal-Free Oxygen Reduction in Alkaline Medium on High-Surface-Area Mesoporous Nitrogen-Doped Carbons Made from Ionic Liquids and Nucleobases. *J. Am. Chem. Soc.* **2011**, *133*, 206–209.

(6) Le Goff, A.; Artero, V.; Jousselme, B.; Phong, D. T.; Guillet, N.; Métayé, R.; Fihri, A.; Palacin, S.; Fontecave, M. From Hydrogenases to Noble Metal–Free Catalytic Nanomaterials for H_2 Production and Uptake. *Science.* **2009**, *326*, 1384–1387.

(7) Campbell, C. T. The Energetics of Supported Metal Nanoparticles: Relationships to Sintering Rates and Catalytic Activity. *Acc. Chem. Res.* **2013**, *46*, 1712–1719.

(8) Schlögl, R.; Abd Hamid, S. B. Nanocatalysis: Mature Science Revisited or Something Really New? *Angew. Chem. Int. Ed.* **2004**, *43*, 1628–1637.

(9) Flytzani-Stephanopoulos, M.; Gates, B. C. Atomically Dispersed Supported Metal Catalysts. *Annu. Rev. Chem. Biomol. Eng.* **2012**, *3*, 545–574.

(10) Yang, X.-F.; Wang, A.; Qiao, B.; Li, J.; Liu, J.; Zhang, T. Single-Atom Catalysts: A New Frontier in Heterogeneous Catalysis. *Acc. Chem. Res.* **2013**, *46*, 1740–1748.

(11) Flytzani-Stephanopoulos, M. Gold Atoms Stabilized on Various Supports Catalyze the Water–Gas Shift Reaction. *Acc. Chem. Res.* **2014**, *47*, 783–792.

(12) Neyman, K. M.; Inntam, C.; Nasluzov, V. A.; Kosarev, R.; Rösch, N. Adsorption of d-Metal Atoms on the Regular MgO(001) Surface: Density Functional Study of Clustermodels Embedded in an Elastic Polarizable Environment. *Appl. Phys. A* **2004**, *78*, 823–828.

(13) Bruix, A.; Nazari, F.; Neyman, K. M.; Illas, F. On the Adsorption and Formation of Pt Dimers on the CeO_2(111) Surface. *J. Chem. Phys.* **2011**, *135*, 244708.

(14) Fu, Q.; Saltsburg, H.; Flytzani-Stephanopoulos, M. Active Nonmetallic Au and Pt Species on Ceria-Based Water-Gas Shift Catalysts. *Science* **2003**, *301*, 935–938.

(15) Zhai, Y.; Pierre, D.; Si, R.; Deng, W.; Ferrin, P.; Nilekar, A. U.; Peng, G.; Herron, J. A.; Bell, D. C.; Saltsburg, H.; Mavrikakis, M.; Flytzani-Stephanopoulos, M. Alkali-Stabilized Pt-OHx Species Catalyze Low-

Temperature Water-Gas Shift Reactions. *Science.* **2010**, *329*, 1633–1637.

(16) Yang, M.; Li, S.; Wang, Y.; Herron, J. A.; Xu, Y.; Allard, L. F.; Lee, S.; Huang, J.; Mavrikakis, M.; Flytzani-Stephanopoulos, M. Catalytically Active Au-O(OH)x- Species Stabilized by Alkali Ions on Zeolites and Mesoporous Oxides. *Science.* **2014**, *346*, 1498–1501.

(17) Peterson, E. J.; DeLaRiva, A. T.; Lin, S.; Johnson, R. S.; Guo, H.; Miller, J. T.; Kwak, J. H.; Peden, C. H. F.; Kiefer, B.; Allard, L. F.; Ribeiro, F. H.; Datye, A. K. Low-Temperature Carbon Monoxide Oxidation Catalysed by Regenerable Atomically Dispersed Palladium on Alumina. *Nat. Commun.* **2014**, *5*, 4885.

(18) Qiao, B.; Wang, A.; Yang, X.; Allard, L. F.; Jiang, Z.; Cui, Y.; Liu, J.; Li, J.; Zhang, T. Single-Atom Catalysis of CO Oxidation Using Pt_1/FeO_x. *Nat. Chem.* **2011**, *3*, 634–641.

(19) Vilé, G.; Albani, D.; Nachtegaal, M.; Chen, Z.; Dontsova, D.; Antonietti, M.; López, N.; Pérez-Ramírez, J. A Stable Single-Site Palladium Catalyst for Hydrogenations. *Angew. Chem. Int. Ed.* **2015**, *54*, 11265–11269.

(20) Wei, H.; Liu, X.; Wang, A.; Zhang, L.; Qiao, B.; Yang, X.; Huang, Y.; Miao, S.; Liu, J.; Zhang, T. FeO_x-Supported Platinum Single-Atom and Pseudo-Single-Atom Catalysts for Chemoselective Hydrogenation of Functionalized Nitroarenes. *Nat. Commun.* **2014**, *5*, 5634.

(21) Bruix, A.; Lykhach, Y.; Matolínová, I.; Neitzel, A.; Skála, T.; Tsud, N.; Vorokhta, M.; Stetsovych, V.; Ševčíková, K.; Mysliveček, J.; Fiala, R.; Václavů, M.; Prince, K. C.; Bruyère, S.; Potin, V.; Illas, F.; Matolín, V.; Libuda, J.; Neyman, K. M. Maximum Noble-Metal Efficiency in Catalytic Materials: Atomically Dispersed Surface Platinum. *Angew. Chem. Int. Ed.* **2014**, *53*, 10525–10530.

(22) Aleksandrov, H. A.; Neyman, K. M.; Vayssilov, G. N. The Structure and Stability of Reduced and Oxidized Mononuclear Platinum Species on Nanostructured Ceria from Density Functional Modeling. *Phys. Chem. Chem. Phys.* **2015**, *17*, 14551–14560.

(23) Pan, Y.; Nilius, N.; Stiehler, C.; Freund, H.-J.; Goniakowski, J.; Noguera, C. Ceria Nanocrystals Exposing Wide (100) Facets: Structure and Polarity Compensation. *Adv. Mater. Interfaces* **2014**, *1*, 1400404.

(24) Kozlov, S. M.; Viñes, F.; Nilius, N.; Shaikhutdinov, S.; Neyman, K. M. Absolute Surface Step Energies: Accurate Theoretical Methods Applied to Ceria Nanoislands. *J. Phys. Chem. Lett.* **2012**, *3*, 1956–1961.

(25) Vayssilov, G. N.; Migani, A.; Neyman, K. Density Functional Modeling of the Interactions of Platinum Clusters with CeO_2 Nanoparticles of Different Size. *J. Phys. Chem. C* **2011**, *115*, 16081–16086.

(26) Vayssilov, G. N.; Lykhach, Y.; Migani, A.; Staudt, T.; Petrova, G. P.; Tsud, N.; Skála, T.; Bruix, A.; Illas, F.; Prince, K. C.; Matolín, V.; Neyman, K. M.; Libuda, J. Support Nanostructure Boosts Oxygen Transfer to Catalytically Active Platinum Nanoparticles. *Nat. Mater.* **2011**, *10*, 310–315.

(27) Migani, A.; Vayssilov, G. N.; Bromley, S. T.; Illas, F.; Neyman, K. M. Dramatic Reduction of the Oxygen Vacancy Formation Energy in Ceria Particles: A Possible Key to Their Remarkable Reactivity at the Nanoscale. *J. Mater. Chem.* **2010**, *20*, 10535–10546.

(28) Migani, A.; Vayssilov, G. N.; Bromley, S. T.; Illas, F.; Neyman, K. M. Greatly Facilitated Oxygen Vacancy Formation in Ceria Nanocrystallites. *Chem. Commun.* **2010**, *46*, 5936.

(29) Branda, M. M.; Ferullo, R. M.; Caus, M.; Illas, F. Relative Stabilities of Low Index and Stepped CeO_2 Surfaces from Hybrid and GGA + U Implementations of Density Functional Theory. *J. Phys. Chem. C* **2011**, *115*, 3716–3721.

(30) Mai, H. X.; Sun, L. D.; Zhang, Y. W.; Si, R.; Feng, W.; Zhang, H. P.; Liu, H. C.; Yan, C. H. Shape-Selective Synthesis and Oxygen Storage Behavior of Ceria Nanopolyhedra, Nanorods, and Nanocubes. *J. Phys. Chem. B* **2005**, *109*, 24380–24385.

(31) Bruix, A.; Neyman, K. M.; Illas, F. Adsorption, Oxidation State, and Diffusion of Pt Atoms on the CeO_2(111) Surface. *J. Phys. Chem. C* **2010**, *114*, 14202–14207.

(32) Sk, M. A.; Kozlov, S. M.; Lim, K. H.; Migani, A.; Neyman, K. M. Oxygen Vacancies in Self-Assemblies of Ceria Nanoparticles. *J. Mater. Chem. A* **2014**, *2*, 18329–18338.

(33) Nedyalkova, R.; Niznansky, D.; Roger, A. C. Iron-Ceria-Zirconia Fluorite Catalysts for Methane Selective Oxidation to Formaldehyde. *Catal. Commun.* **2009**, *10*, 1875–1880.

(34) Satsuma, A.; Yanagihara, M.; Ohyama, J.; Shimizu, K. Oxidation of CO over Ru/Ceria Prepared by Self-Dispersion of Ru Metal Powder into Nano-Sized Particle. *Catal. Today* **2013**, *201*, 62–67.

(35) Lin, S. S. Y.; Kim, D. H.; Engelhard, M. H.; Ha, S. Y. Water-Induced Formation of Cobalt Oxides over Supported Cobalt/ceria-Zirconia Catalysts under Ethanol-Steam Conditions. *J. Catal.* **2010**, *273*, 229–235.

(36) Haneda, M.; Shinoda, K.; Nagane, A.; Houshito, O.; Takagi, H.; Nakahara, Y.; Hiroe, K.; Fujitani, T.; Hamada, H. Catalytic Performance of Rhodium Supported on Ceria–zirconia Mixed Oxides for Reduction of NO by Propene. *J. Catal.* **2008**, *259*, 223–231.

(37) Huang, Y.; Wang, A.; Li, L.; Wang, X.; Su, D.; Zhang, T. "Ir-in-Ceria": A Highly Selective Catalyst for Preferential CO Oxidation. *J. Catal.* **2008**, *255*, 144–152.

(38) Carrasco, J.; López-Durán, D.; Liu, Z.; Duchoň, T.; Evans, J.; Senanayake, S. D.; Crumlin, E. J.; Matolín, V.; Rodríguez, J. A.; Ganduglia-Pirovano, M. V. In Situ and Theoretical Studies for the Dissociation of Water on an Active Ni/CeO_2 Catalyst: Importance of Strong Metal-Support Interactions for the Cleavage of O-H Bonds. *Angew. Chem. Int. Ed.* **2015**, *54*, 3917–3921.

(39) Colussi, S.; Gayen, A.; Camellone, M. F.; Boaro, M.; Llorca, J.; Fabris, S.; Trovarelli, A. Nanofaceted Pd-O Sites in Pd-Ce Surface Superstructures: Enhanced Activity in Catalytic Combustion of Methane. *Angew. Chem. Int. Ed.* **2009**, *48*, 8481–8484.

(40) Gulyaev, R. V.; Kardash, T. Y.; Malykhin, S. E.; Stonkus, O. A.; Ivanova, A. S.; Boronin, A. I. The Local Structure of $Pd_xCe_{1-x}O_{2-x-\delta}$ Solid Solutions. *Phys. Chem. Chem. Phys.* **2014**, *16*, 13523–13539.

(41) Nagai, Y.; Hirabayashi, T.; Dohmae, K.; Takagi, N.; Minami, T.; Shinjoh, H.; Matsumoto, S. Sintering Inhibition Mechanism of Platinum Supported on Ceria-Based Oxide and Pt-Oxide–support Interaction. *J. Catal.* **2006**, *242*, 103–109.

(42) Wu, T.; Pan, X.; Zhang, Y.; Miao, Z.; Zhang, B.; Li, J.; Yang, X. Investigation of the Redispersion of Pt Nanoparticles on Polyhedral Ceria Nanoparticles. *J. Phys. Chem. Lett.* **2014**, *5*, 2479–2483.

(43) Gao, Y.; Wang, W.; Chang, S.; Huang, W. Morphology Effect of CeO_2 Support in the Preparation, Metal-Support Interaction, and Catalytic Performance of Pt/CeO_2 Catalysts. *ChemCatChem* **2013**, *5*, 3610–3620.

(44) Elias, J. S.; Risch, M.; Giordano, L.; Mansour, A. N.; Shao-Horn, Y. Structure, Bonding, and Catalytic Activity of Monodisperse, Transition-Metal-Substituted CeO_2 Nanoparticles. *J. Am. Chem. Soc.* **2014**, *136*, 17193–17200.

(45) Müller-Buschbaum, H. Zur Kristallchemie Der Oxoargentate Und Silberoxometallate. *Z. Anorg. Allg. Chem.* **2004**, *630*, 2125–2175.

(46) Hu, P.; Huang, Z.; Amghouz, Z.; Makkee, M.; Xu, F.; Kapteijn, F.; Dikhtiarenko, A.; Chen, Y.; Gu, X.; Tang, X. Electronic Metal-Support Interactions in Single-Atom Catalysts. *Angew. Chemie Int. Ed.* **2014**, *53*, 3418–3421.

(47) Venezia, A. M.; Pantaleo, G.; Longo, A.; Di Carlo, G.; Casaletto, M. P.; Liotta, F. L.; Deganello, G. Relationship between Structure and CO Oxidation Activity of Ceria-Supported Gold Catalysts. *J. Phys. Chem. B* **2005**, *109*, 2821–2827.

(48) Branda, M. M.; Hernández, N. C.; Sanz, J. F.; Illas, F. Density Functional Theory Study of the Interaction of Cu, Ag, and Au Atoms with the Regular CeO_2 (111) Surface. *J. Phys. Chem. C* **2010**, *114*, 1934–1941.

(49) Shriver, D. F.; Atkins, P. W. *Inorganic Chemistry*; 3rd ed.; Oxford University Press, 1999.

(50) Chase, M. W. *NIST-JANAF Thermochemical Tables*; 4th Ed.; Journal of Physical and Chemical Reference Data, 1998.

(51) Kubaschewski, O.; Alcock, C. B. *Metallurgical Thermochemistry*; 5th Ed.; Pergamon Press, 1983.

(52) Preda, G.; Migani, A.; Neyman, K. M.; Bromley, S. T.; Illas, F.; Pacchioni, G. Formation of Superoxide Anions on Ceria Nanoparticles by Interaction of Molecular Oxygen with Ce^{3+} Sites. *J. Phys. Chem. C* **2011**, *115*, 5817–5822.

(53) Kullgren, J.; Hermansson, K.; Broqvist, P. Supercharged Low-Temperature Oxygen Storage Capacity of Ceria at the Nanoscale. *J. Phys. Chem. Lett.* **2013**, *4*, 604–608.

(54) Huang, X.; Beck, M. J. Determining the Oxidation State of Small, Hydroxylated Metal-Oxide Nanoparticles with Infrared Absorption Spectroscopy. *Chem. Mater.* **2015**, *27*, 2965–2972.

(55) Migani, A.; Vayssilov, G. N.; Bromley, S. T.; Illas, F.; Neyman, K. M. Greatly Facilitated Oxygen Vacancy Formation in Ceria Nanocrystallites. *Chem. Commun.* **2010**, *46*, 5936–5938.

(56) Fiala, R.; Figueroba, A.; Bruix, A.; Vaclavu, M.; Rednyk, A.; Khalakhan, I.; Vorokhta, M.; Lavkova, J.; Illas, F.; Potin, V.; Matolinova, I.; Neyman, K. M.; Matolin, V. High Efficiency of Pt^{2+}- CeO_2 Novel Thin Film Catalyst as Anode for Proton Exchange Membrane Fuel Cells. *Appl. Catal. B Environ.* **2016**, *197*, 262–270.

(57) Neitzel, A.; Figueroba, A.; Lykhach, Y.; Skála, T.; Vorokhta, M.; Tsud, N.; Mehl, S.; Ševčíková, K.; Prince, K. C.; Neyman, K. M.; Matolín, V.; Libuda, J. Atomically Dispersed Pd, Ni, and Pt Species in Ceria-Based Catalysts: Principal Differences in Stability and Reactivity. *J. Phys. Chem. C* **2016**, *120*, 9852–9862.

(58) Lykhach, Y.; Figueroba, A.; Farnesi Camellone, M.; Neitzel, A.; Skála, T.; Negreiros, F. R.; Vorokhta, M.; Tsud, N.; Prince, K. C.; Fabris, S.; Neyman, K. M.; Matolín, V.; Libuda, J. Reactivity of Atomically Dispersed Pt^{2+} Species towards H_2 : Model Pt−CeO_2 Fuel Cell Catalyst. *Phys. Chem. Chem. Phys.* **2016**.

(59) Kittel, C. *Introduction to Solid State Physics*; 8th Ed.; J. Wiley: Hoboken, NJ, 2005.

(60) Nilius, N.; Kozlov, S. M.; Jerratsch, J. F.; Baron, M.; Shao, X.; Viñes, F.; Shaikhutdinov, S.; Neyman, K. M.; Freund, H. J. Formation of One-Dimensional Electronic States along the Step Edges of CeO_2(111). *ACS Nano* **2012**, *6*, 1126–1133.

(61) Dvorák, F.; Camellone, M. F.; Tovt, A.; Tran, N.; Negreiros, F. R.; Vorokhta, M.; Skála, T.; Matolínová, I.; Myslivecek, J.; Matolín, V.; Fabris, S. Creating Single-Atom Pt-Ceria Catalysts by Surface Step Decoration. *Nat. Commun.* **2016**, *7*, 10801.

(62) Hatanaka, M.; Takahashi, N.; Tanabe, T.; Nagai, Y.; Dohmae, K.; Aoki, Y.; Yoshida, T.; Shinjoh, H. Reversible Changes in the Pt Oxidation State and Nanostructure on a Ceria-Based Supported Pt. *J. Catal.* **2009**, *266*, 182–190.

CHAPTER FOUR

Structure and redox stability of ceria nanoparticles doped by late transition metals

4.1. Introduction

As shown in the previous chapter, {100} nanofacets present at the surface of ceria are able to anchor a wide variety of transition metal atoms. Nevertheless, this is not the only way metal atoms can interact with ceria support. Alternatively, such metal atoms can substitute atoms of cerium in the crystalline lattice. This approach often referred to as doping has attracted considerable attention for preparing a new type of catalytic materials called noble metal ionic catalysts.[1-3]

Unlike more inert irreducible metal-oxide supports, such as MgO or Al_2O_3, CeO_2 can directly participate in chemical reactions due to its ability to release and uptake O atoms under reducing and oxidizing conditions, respectively. This feature, crucial for applications in catalysis and known as oxygen storage capacity (OSC), arises from the relatively facile reduction of Ce cations from the +4 to +3 oxidation state.

Dopants can be classified according to their oxidation states relative to that of the metal in the host material. Low-valence dopants exhibit a valence (oxidation state) in their own stable oxide that is lower than that of the cation they substitute in the host oxide.[4,5] Such dopants induce electron deficit on O anions, i.e. empty states (holes) at low energies near the valence band of the material. Energetically very favorable filling of these holes with electrons left by removed O atoms can facilitate the formation of oxygen vacancies (O_{vac}). Because the differences in oxidation states of the host and dopant metals spontaneously induce O vacancies, the latter are often referred to as charge compensating ones. In turn, high-valence dopants have a valence in their stable oxide larger than that of the cation they substitute.[4] In this case, the effect of the dopants largely depends on whether the host oxide is reducible or not. If the host oxide is non-reducible, the presence of the dopant makes it more difficult to remove O atoms from the host and may even induce the formation of charge compensating *metal* vacancies. If the host oxide is reducible, the difference in oxidation states can be compensated by the transfer of electrons from the dopant to the host cations, partially reducing them. When the dopant and the substituted cation exhibit the same valence, no clear trends can be established.[4] The synthesis and characterization of the different kinds of doped oxides is an active field of research and we refer to some of the extensive existing literature for further details.[4,6-9]

For many catalytic materials based on combinations of metals with metal-oxides, the former are found in the form of cations, which seems to play a crucial role in the catalytic performance.[1,2,4,10,11] Despite experimental evidences of the presence and activating nature of such cationic transition metal species, atomic-level data on the dopant species are rather scarce. The application of theoretical modeling methods based on the DFT can provide detailed information which allows identifying the structure and stability of these ionic species together with their role in the chemical reactivity.

The effect of M dopants on the reducibility of bulk and extended surfaces of ceria has been previously investigated by means of theoretical modeling.[4,12-18] Hermansson and co-workers performed DFT-based calculations to study the doping of bulk ceria with Pd, Pt, and Rh.[15,16] The authors associated the enhanced reducibility of doped ceria with the notable structural relaxation of the dopants inside the host lattice. Subsequent removal of O atoms yielded endothermic oxygen vacancy formation. Later, Scanlon et al. attributed the stability and easier reducibility of $Ce_{1-x}(Pd/Pt)_xO_2$ solid solutions to crystal field effects, whereby Pd and Pt dopants adopt a more stable square-planar coordination different from the characteristic cubic coordination of Ce atoms in the host oxide.[17] Such square-planar environment exhibits easily removable under-coordinated oxygen atoms, leading to notably exothermic O_{vac} formation for Pd-doped and Pt-doped ceria. According to these results, the formation of a charge compensating O_{vac} in the vicinity of the dopant and the concomitant reduction of the metal cations from +4 to +2 state are spontaneous processes. Doping ceria surfaces with Pd and Pt was also experimentally found to activate O atoms near the dopants, which facilitate the activation of methane.[19,20] Due to their small size, Ni dopants can be introduced in the lattice of ceria forming two different point defects, interstitial and substitutional. The oxidation state of the doping Ni atom was calculated to depend on the type of the point defect, yielding either Ni^{+} in the interstitial defect or Ni^{2+} in the substitutional one.[18] The doping in the substitutional defect was reported to be notably more favorable.

Despite strong efforts devoted to understanding metal-doped ceria, to the best of our knowledge computational studies published so far have only considered doping in the bulk or on extended surfaces of ceria. Nanoparticulate CeO_2 exposing various low-coordinated positions is ubiquitous in ceria-based catalytic materials. Thus, it is important to understand the peculiarities of metal-doping in NP models. Experimentally, nanostructured ceria can also be synthesized in the form of thin films

with rough surfaces.[21-23] These nanostructures can anchor and stabilize atomically dispersed transition metal atoms in surface positions, being more accessible to reactants. Following this idea, the effect of doping nanostructured ceria with Pt atoms has been computationally investigated by our group.[24] Combination of experimental and computational techniques enabled to determine the preference of Pt to substitute Ce^{4+} cations located at the surface of ceria NPs and to analyze their redox reactivity.

In the present Chapter we discuss calculations based on DFT performed to study the stability of four technologically relevant metal dopants (M = Pt, Pd, Ni, and Cu) substituting cerium atoms in different positions of an exemplary ceria NP. Ni and Cu represent two promising alternatives to catalysts based on platinum group metals. Hence, understanding their interaction with ceria can contribute to the development of new and more cost-effective materials. Our work also provides insights about how two redox processes relevant to operational conditions in fuel cells take place in such doped NP systems: the formation of oxygen vacancies and the dissociative adsorption of H_2.

4.2. Models

Details on the models used for representing ceria NPs can be found in Chapter 3. Four different positions for the substitution of cerium atoms have been considered: one in a bulk-like site of the ceria NP (D1), two at an edge (D2, D3) and one at a corner site (D4).

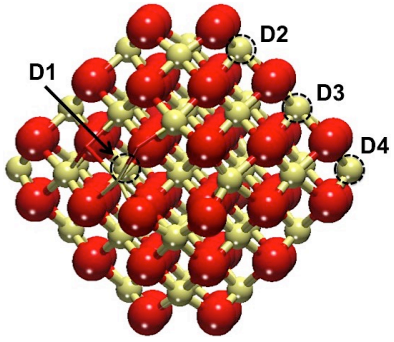

Figure 4.1. Cuboctahedral $Ce_{40}O_{80}$ NP chosen to model nanostructured ceria. Yellow and red spheres represent Ce^{4+} cations and O^{2-} anions, respectively. Different locations D1 – D4 for the substitution of cerium atoms upon doping are indicated with dashed circles.

Formation energies of oxygen vacancies E_{vac} have been calculated with respect to the energy of O_2 molecule, $E(O_2)$, as follows: $E_{vac} = \{E(M\text{-}Ce_{39}O_{79}) + 1/2[E(O_2)] - E(M\text{-}Ce_{39}O_{80})\}$, where $M\text{-}Ce_{39}O_{80}$ is the ceria NP with a metal atom substituting a cerium atom and $M\text{-}Ce_{39}O_{79}$ is the ceria NP with a metal atom substituting a cerium atom in the presence of an O_{vac} in one of the {100} nanofacets.

Adsorption energy of hydrogen $E_{ad}(H_2)$ has been calculated per H atom, $E_H = ½[E(H_2MCe_{39}O_{80}) - E(MCe_{39}O_{80}) - E(H_2)]$, with $E(H_2MCe_{39}O_{80})$ and $E(MCe_{39}O_{80})$ being the total calculated energies of the NP substrate hydrogenated with 2 adsorbed H atoms and the non-hydrogenated substrate, respectively.

To compare the doping energetics ΔE_{dop} for different metals we used the following process characterizing the energy required for substituting a Ce atom in the ceria NP by a doping M atom:

$$Ce_{40}O_{80} + M + O_2 \rightarrow MCe_{39}O_{80} + CeO_2 \ , \qquad (4.1)$$

where $Ce_{40}O_{80}$ and $MCe_{39}O_{80}$ are the pristine and M-doped ceria NPs, respectively, M is the atomic dopant reference with the energy $E(M) = E(M_{79})/79$, defined as the per-atom total energy value of a truncated-octahedral model metal particle of 79 atoms,[25] the reference energy of O_2 molecule is taken from Ref. 26 and the energy of a CeO_2 reference is $E(CeO_2) = E(Ce_{40}O_{80})/40$.

Analysis of ΔE_{dop} energies for reduced systems with either an O_{vac} or adsorbed H_2 has been performed considering the processes analogous to that of Eq. (4.1) for the unreduced systems $Ce_{40}O_{80}$ and $MCe_{39}O_{80}$:

$$Ce_{40}O_{79} + M + O_2 \rightarrow MCe_{39}O_{79} + CeO_2 \quad (4.2)$$

and

$$H_2Ce_{40}O_{80} + M + O_2 \rightarrow H_2MCe_{39}O_{80} + CeO_2\ , \quad (4.3)$$

where $Ce_{40}O_{79}$ and $MCe_{39}O_{79}$ are NPs with an O_{vac} in the same {100} nanofacet position of the pristine and M-doped ceria models, respectively, $H_2Ce_{40}O_{80}$ and $H_2MCe_{39}O_{80}$ are, respectively, pristine and M-doped NPs with adsorbed H_2, and M, CeO_2, and O_2 are defined in Eq. (4.1).

4.3. Results and discussion

In this section, we present the results obtained for the substitution of the four different transition M atoms in different positions of the ceria NP. We provide analysis of the data obtained on the energetic stability of the doping process together with the structural parameters of the resulting systems.

Unreduced $MCe_{39}O_{80}$ systems

We first discuss the unreduced (stoichiometric) $MCe_{39}O_{80}$ systems obtained by substitution of a Ce atom in the $Ce_{40}O_{80}$ NP by an atom of each studied M dopants (see Table 4.1 for the calculated energetic, electronic, and structural parameters).

Substitution in the inner site D1 can cause different scenarios involving the coordination of the dopant atoms. The D1 position is analogous to that of Ce^{4+} cations in bulk CeO_2. Therefore, it is more restricted towards restructuring than surface cationic sites due to the larger number of O atoms surrounding the inner cations and correspondingly less space available. Both Pt and Pd dopants adopt in the D1 site a 6+2 coordination, where M is bound to six O atoms forming its first coordination sphere, while leaving other two O atoms more distant. The 6+2 coordination for Pt in the D1 site is calculated to be the most stable, by 134 kJ mol^{-1} more stable than the (slightly distorted) cubic coordination by 8 nearby O atoms, which is analogous to the preferred coordination of Ce. Note that our earlier calculations, which did not address the 6+2 coordination, revealed the 8 coordination of Pt in cationic sites inside the same ceria NP as the most stable.[24] Based on our present results, inner Pt dopants in ceria NPs appear to be significantly (by 66 kJ mol^{-1}) more stable than the considered in Ref. 24, however, surface Pt dopants remain more stable even with respect to the 6+2 coordination of Pt. In turn, a structure with a Pd dopant surrounded by 8 nearby O^{2-} never resulted from our calculations performed similarly to Pt cases, hence we can consider the 8 coordinated Pd in ceria not to constitute a local minimum.

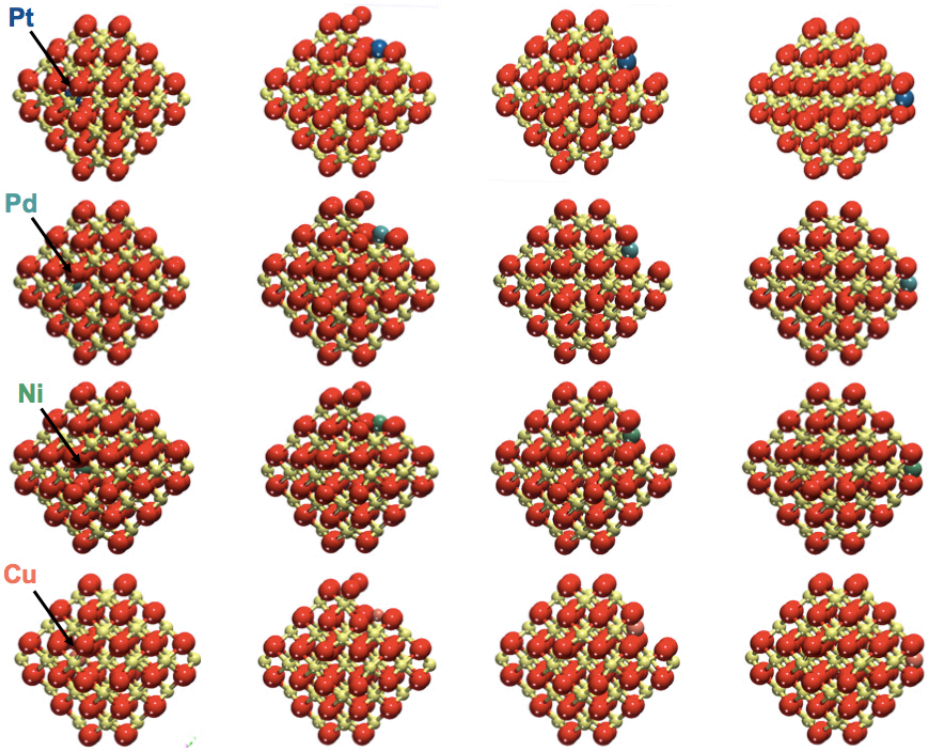

Figure 4.2. Structures of unreduced $MCe_{39}O_{80}$ ceria NPs with Pt, Pd, Ni and Cu dopants substituting Ce atoms in the interior (D1), edge (D2, D3) or corner positions (D4) indicated in Figure 4.1. Depicted atoms are O – red, Ce – yellow (+4) or light brown (+3).

Particle	D#	ΔE kJ mol^{-1}	ΔE_{dop} kJ mol^{-1}	q(M) a.u.	μ(M) μB	n(M)	M-O pm	m
$PtCe_{39}O_{80}$	D1	0	-19	1.66	0.00	4	204-209	6
	D2	53	34	1.20	0.51	3	195-202	4
	D3	-47	-66	1.39	0.78	3	188-203	4
	D4	-221	-240	1.32	0.78	3	191-202	4
$PdCe_{39}O_{80}$	D1	0	59	1.51	0.00	4	204-211	6
	D2	19	78	1.01	0.13	3	200-205	4
	D3	-66	-7	1.12	0.35	3	193-206	4
	D4	-228	-169	1.03	0.00	2	198-204	4
$NiCe_{39}O_{80}$	D1	0	19	1.28	0.61	3	179-187	4
	D2	-58	-39	1.18	0.59	3	181-190	4
	D3	-147	-129	1.27	0.72	3	180-187	4
	D4	-307	-288	1.24	0.73	3	182-186	4

$CuCe_{39}O_{80}$	D1	0	147	1.14	0.00	3	193-200	4
	D2	-129	17	1.18	0.00	3	186-188	4
	D3	-208	-62	1.15	0.00	3	185-188	4
	D4	-371	-225	1.26	0.00	3	187	4

Table 4.1. Calculated properties of $MCe_{39}O_{80}$ NPs with one Ce atom in the position D# substituted by a doping atom M = Pt, Pd, Ni, Cu (see Fig. 4.1). ΔE – energy with respect to the reference with M in D1 position; ΔE_{dop} – doping energy evaluated according to Eq. 1; q(M), μ(M), and n(M) – Bader charge, magnetization, and estimated oxidation state, respectively, of the atom M in ceria particle; M-O – range of interatomic distances between M and the nearest m O neighbours of it.

Unlike Pt and Pd, Ni and Cu in the D1 site show preference to bind to only four nearby O atoms, in a square planar fashion. The lattice distortion in the new square coordination leaves the other four O atoms more distant from M and thus less strongly bound.

As it can be noted for all studied dopants, substitution in surface positions of the ceria NP induces a change in the local coordination of the doping atoms. That is, Ce atoms located in edge (D2, D3) and corner (D4) positions of ceria are surrounded by 6 and 4 oxygen atoms, respectively. Nevertheless, it seems that all M dopants under scrutiny prefer to be bound to oxygen atoms arranged in a square-planar mode, lowering the number of M-O bonds rather than keeping the initial local coordination of Ce. Therefore, the high flexibility of surface atoms allows the substitute M to move out of the replaced Ce position and modify its local coordination.

The analysis of the Bader charge and magnetization values is helpful for estimating the oxidation state of each dopant metal M in different environments. Note that for the unreduced $MCe_{39}O_{80}$ models under scrutiny the formal oxidation state of all M dopant is expected to be +4, the same as the oxidation state of the substituted Ce atom. Nevertheless, it seems that such highly oxidized state can only be maintained by Pt and Pd atoms substituting inner Ce^{4+} cations. In these two cases, zero magnetization values of the M centres indicate the absence of unpaired electrons on them. In line with the high Bader charge values of 1.66 a.u. (Pt) and 1.51 a.u. (Pd), we can assign the +4 state to the inner substituting Pt and Pd dopants. This high oxidation state appears to become

unstable for doping metal atoms occupying surface cationic positions. For all four M atoms in positions D2-D4, the lower Bader charge values (1.0 – 1.3 a.u., Table 4.1) and non-zero magnetization (zero magnetization of Cu) indicate that some electron density has been transferred from nearby O atoms to the M centres. Electron holes caused by such electron transfer are manifested in the density of states (DOS) plots in Figs. 4.3-4.6. Presence of electron holes is also evidenced by the non-zero magnetic moment of O atoms (not shown). To this end, zero magnetization of Pd in the most open corner D4 position in combination with DOS plots in Fig. 4.4 revealing somewhat electron deficient O anions implies a +2 oxidation state of this dopant. Note that atomic Cu contains an odd number of electrons, at variance with an even number of electrons in Pt, Pd, and Ni atoms. Thus, zero magnetization of Cu in D1-D4 structures along with its relatively high Bader charge of 1.14-1.26 a.u. point to the oxidation state of Cu +3. To summarize, we also assign the oxidation state +3 to the dopants Pt, Pd and Ni in all other studied unreduced models of $MCe_{39}O_{80}$ except for Pt and Pd being +4 in the inner D1 positions and Pd acquiring +2 in the corner D4 position.

Surface doping positions are energetically favoured for all metal atoms with respect to the inner bulk-like D1 ones, with the corner D4 position being most stabilized, by 221, 228, 307 and 371 kJ mol^{-1} for Pt, Pd, Ni and Cu, respectively (Table 4.1).

The calculated ΔE_{dop} energies for dopants M in different positions of the unreduced $MCe_{39}O_{80}$ are shown in Table 4.1. Positive values point to the energetic preference of atom M to stay in metallic particles rather than doping ceria, whereas negative energies indicate favourable location of the dopant in the particular lattice position of ceria. Analysis of ΔE_{dop} for the unreduced doped ceria models $MCe_{39}O_{80}$ does not reveal clear trends. Substitution of inner Ce atom (in D1 position) is estimated to be energetically slightly favoured solely for Pt, ΔE_{dop} = -19 kJ mol^{-1}. Surface doping by all 4 metals appears to be energetically quite favourable, although the M dopants feature there uncommon +3 state with electron holes created in O2p states fully occupied in the pristine system $Ce_{40}O_{80}$. These electronic structure peculiarities can be the origin of small ΔE_{dop} values for sites D2 and D3, with the largest in magnitude ΔE_{dop} = -129 kJ mol^{-1} for Ni in position D3. Corner Ce atoms (sites D4) are most prone to be substituted by all considered M atoms, resulting in ΔE_{dop} equal to -240, -169, -288 and -225 kJ mol^{-1} for Pt, Pd, Ni and Cu dopants, respectively.

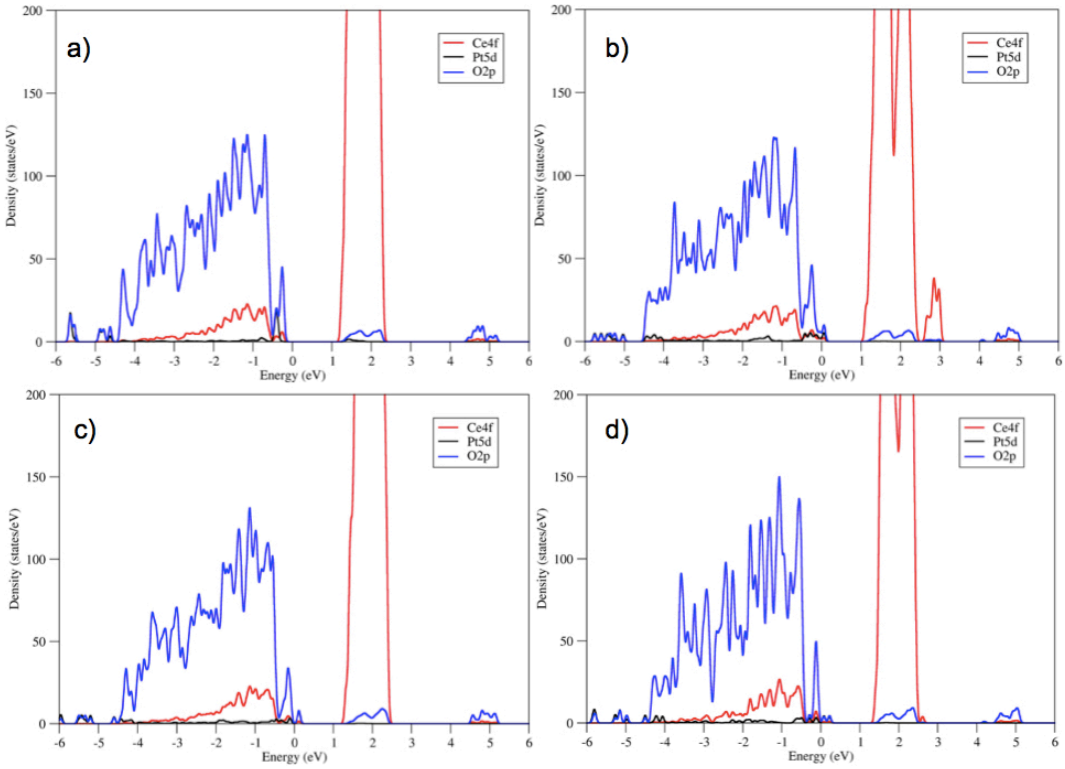

Figure 4.3. DOS plots of stoichiometric $PtCe_{39}O_{80}$ with Pt located in the following positions: a) D1, b) D2, c) D3, and d) D4.

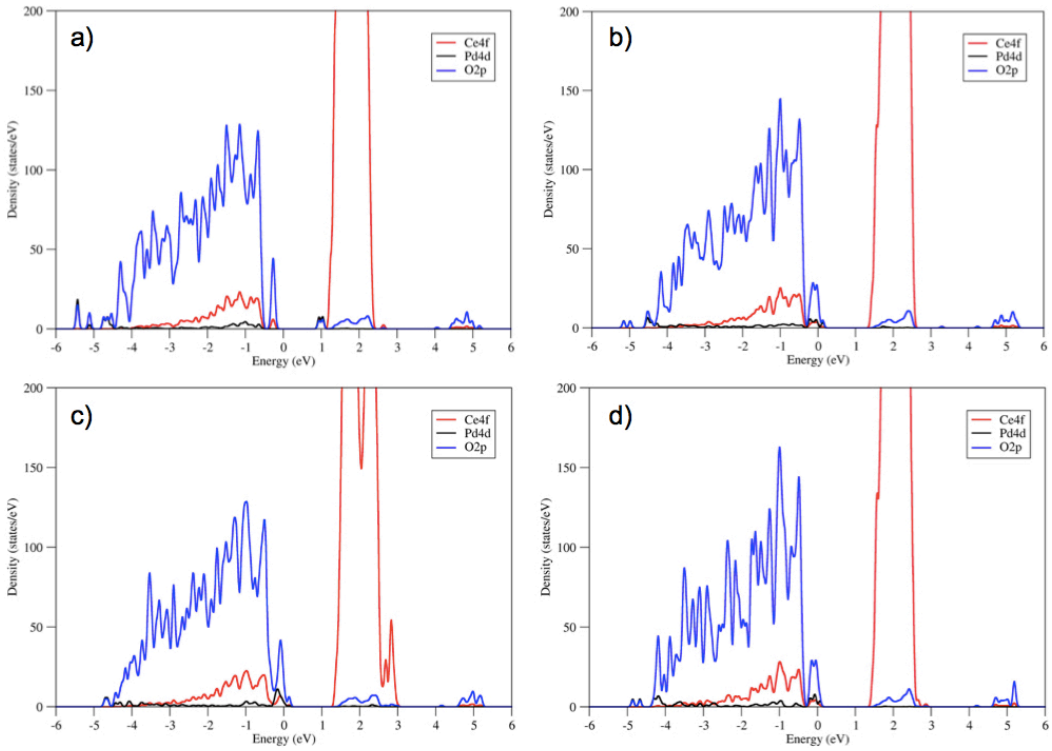

Figure 4.4. DOS plots of stoichiometric $PdCe_{39}O_{80}$ with Pd located in the following positions: a) D1, b) D2, c) D3, and d) D4.

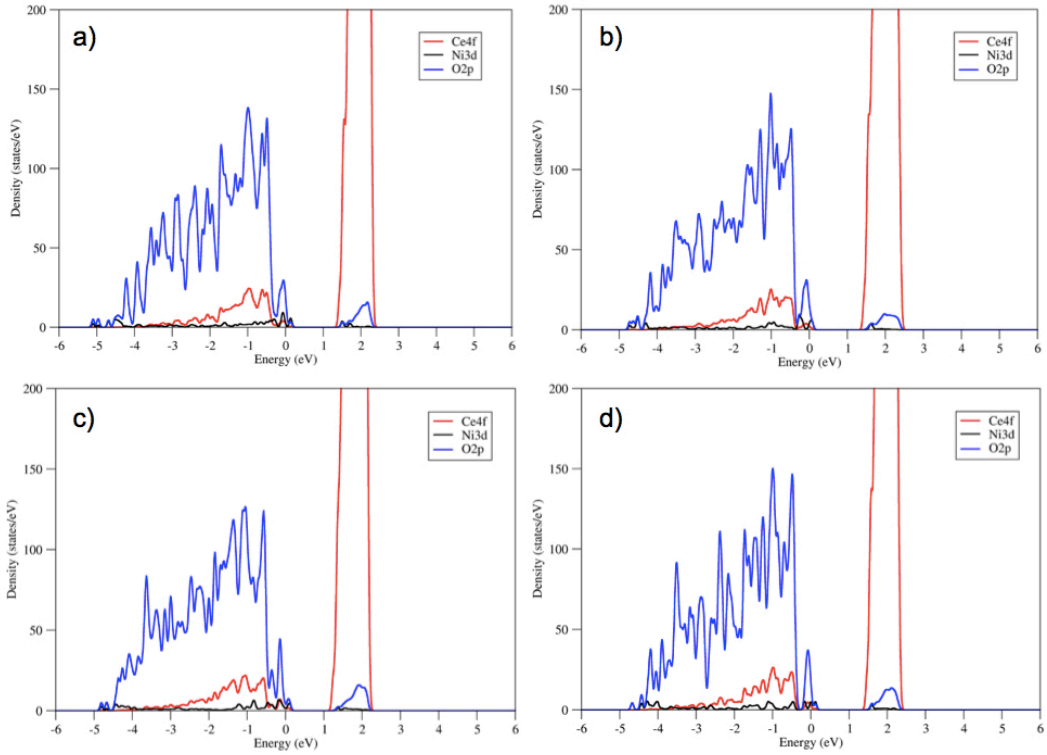

Figure 4.5. DOS plots of stoichiometric $NiCe_{39}O_{80}$ with Ni located in the following positions: a) D1, b) D2, c) D3, and d) D4.

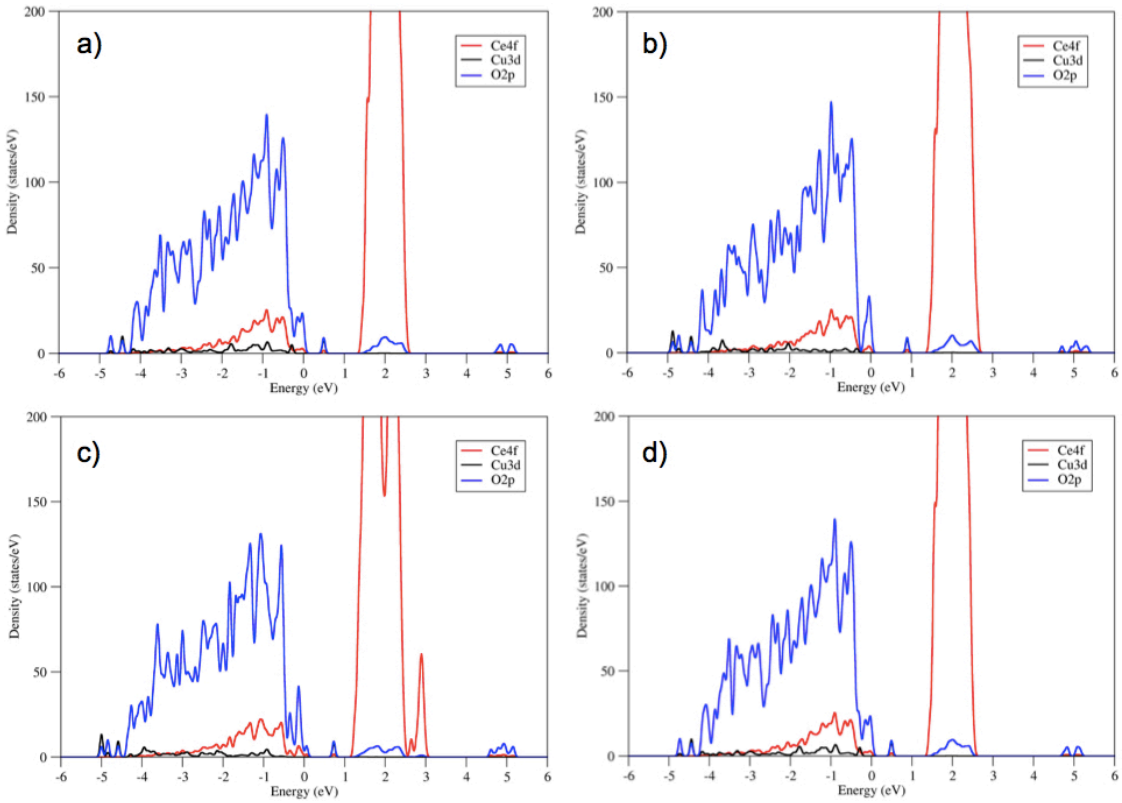

Figure 4.6. DOS plots of stoichiometric $CuCe_{39}O_{80}$ with Cu located in the following positions: a) D1, b) D2, c) D3, and d) D4.

The data discussed so far imply the diffusion of the dopants from inner cationic positions to the surface upon the preparation of the doped ceria-based nanomaterials. These diffusion processes should trigger the doping metal atoms to be preferentially exposed on the surface of the catalytic nanostructures and readily accessible to reactants participating in chemical processes mediated by them. However, the uncommon +3 oxidation state of M atoms and the withdrawal of electron density from O^{2-} anions suggest that the systems corresponding to the $MCe_{39}O_{80}$ models should be easily reducible under experimental conditions. To this end we discuss exemplary two-electron reduction processes such as the formation of an oxygen vacancy O_{vac} and dissociative homolytic adsorption of a H_2 molecule when exposed to hydrogen atmosphere, in view of their effects on the energies and structures of the $MCe_{39}O_{80}$ species.

Partially reduced $MCe_{39}O_{79}$ and $H_2/MCe_{39}O_{80}$ systems

First we analyze the effect of removing an O atom from a {100} nanofacet of the M-ceria NPs, which was calculated to be the most easily removable O atom from the pristine undoped ceria NPs.[27,28] The most stable structures of the resulting species with an O_{vac} are shown in Fig. 4.7. O_{vac} formation leaves in M-ceria systems two electrons capable of restoring the -2 state of O anions and to partially reduce M^{n+} or Ce^{4+} cations.

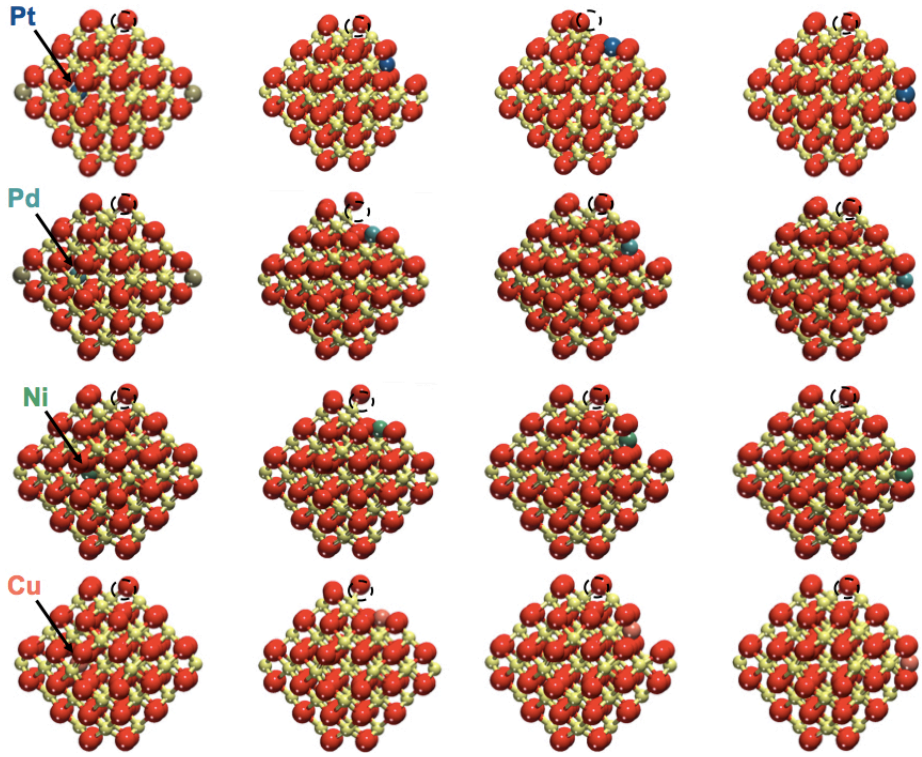

Figure 4.7. Most stable structures of $MCe_{39}O_{80}$ systems, where an O vacancy has been created by removing an O atom from the {100} nanofacet (denoted by a dashed circle).

Particle	D#	E_{vac} kJ mol^{-1}	ΔE kJ mol^{-1}	ΔE_{dop} kJ mol^{-1}	q(M) a.u.	μ(M) μB	n(M)	M-O pm	m
$PtCe_{39}O_{79}$	D1	100	0	4	1.67	0.00	4	204-209	6
	D2	-134	-181	-177	0.97	0.00	2	202-205	4
	D3	-16	-162	-159	0.93	0.00	2	202-204	4
	D4	-21	-342	-338	0.89	0.00	2	204-205	4
$PdCe_{39}O_{79}$	D1	77	0	59	1.52	0.00	4	205-210	6
	D2	-170	-227	-169	0.90	0.00	2	202-206	4
	D3	-70	-213	-154	0.94	0.00	2	202-204	4
	D4	-81	-386	-327	0.88	0.00	2	205-206	4
$NiCe_{39}O_{79}$	D1	-40	0	-98	1.11	0.00	2	186-187	4
	D2	-127	-145	-243	1.06	0.00	2	187-190	4
	D3	-30	-137	-236	1.06	0.00	2	188-189	4
	D4	-31	-298	-396	1.05	0.00	2	189-190	4
$CuCe_{39}O_{79}$	D1	-39	0	31	1.17	0.55	2	203-220	4
	D2	-93	-183	-152	1.03	0.48	2	194-199	4

D3	-13	-182	-152	1.07	0.49	2	195-198	4
D4	5	-328	-297	1.01	0.47	2	197-200	4

[a] E_{vac} = 77 kJ mol^{-1} for this O position in the pristine $Ce_{40}O_{80}$ particle[29]

Table 4.2. Calculated properties of ceria NPs with an oxygen vacancy O_{vac} in a {100} nanofacet and one Ce atom in the position D# substituted by a doping atom M = Pt, Pd, Ni, Cu (Fig. 4.7). E_{vac} – oxygen vacancy formation energy calculated with respect to the energies of $MCe_{39}O_{80}$ and $½O_2$;[a] other notations as in Table 4.1.

When a surface Ce atom (in positions D2-D4) is substituted by an M atom, according to Bader charge and magnetization analyses (Table 4.2, Figs. 4.8-4.11) electrons left by the released O atom reduce the dopant and restore the complete occupation of O2p shells without forming Ce^{3+} cations. All studied surface M dopants retain their local coordination upon this reduction process and feature +2 states, typical of species with a d^8 electron configuration. We assign Cu also the +2 state due to notable magnetization values inherent in the presence of an unpaired d electron. For $MCe_{39}O_{79}$ systems with the O_{vac}, similar to the unreduced $MCe_{39}O_{80}$ ones, M dopants in the surface D2-D4 positions are found to be energetically favored over those in the bulk-like positions D1 inside the NPs.

In the latter systems, only Pt and Pd dopants are calculated to keep their oxidation states after the formation of the O_{vac} (Table 4.2). In each case, two electrons of the removed O atom reduced two corner Ce^{4+} cations to Ce^{3+}, while Pt and Pd maintained their 6+2 coordination environment. Exothermic O_{vac} formation in the D1 Pt and Pd systems by 100 and 77 kJ mol^{-1}, respectively, indicates stability of the +4 oxidation states of these dopants substituting inner Ce cations. We note that this E_{vac} value for the system with inner Pt differs from the value of 34 kJ mol^{-1} (Ref. 24) due to the fact already mentioned in Section 3.1, that is, in the cited work the less stable 8-coordinated was used as a reference system. In turn, Ni dopant is unable to acquire the exceedingly high +4 oxidation state. Thus, in the course of the O_{vac} formation it accepts two electrons and becomes a +2 state, without forming Ce^{3+} cations.

Inclusion of the dopants in surface sites of ceria NPs results in strongly lowered E_{vac} values compared to the undoped NP with the lowest E_{vac} = 77 kJ mol^{-1}.[29] For instance (Table 4.2), inclusion of Pd in D2 position lowers the energy required to create

an O_{vac} in the {100} facet by 247 kJ mol^{-1} to -170 kJ mol^{-1}. Negative values indicate that the release of the O atom is spontaneous, so that the resulting O_{vac} is charge compensating. Ceria nano-architectures promote (lower coordinated) O atoms to become more easily removable and thus more reactive. The calculated oxidation states of M dopants in ceria (Table 4.2) agree with the XPS data, e.g. +4 and +2 for Pt,[30,31] +2 for Pd,[11,31,32] Ni,[31,33] and Cu.[10]

For substituting the internal D1 Ce atom, the only exothermic process is calculated for Ni, ΔE_{dop} = -98 kJ mol^{-1} (Table 4.2). For surface substitutions, removal of the O atom allows dopants to feature the proper oxidation state, which is reflected in favourable doping. Among studied dopants Ni features the highest in magnitude ΔE_{dop} energies of -243, -235, and -396 kJ mol^{-1} for D2, D3, and D4 positions, respectively. Corner Ce position D4 is the most favourably substituted by each considered M atom, with energies of -338, -327, -396, and -297 kJ mol^{-1} for Pt, Pd, Ni, and Cu, respectively.

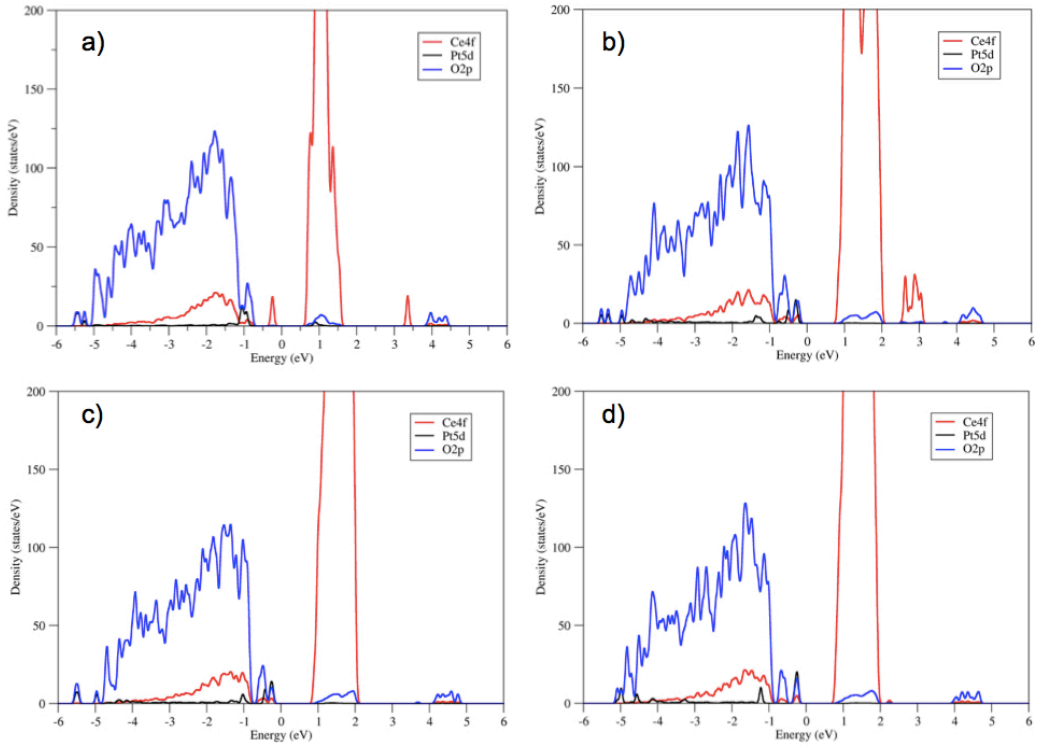

Figure 4.8. DOS plots of $PtCe_{39}O_{79}$ corresponding to with Pt located in the following positions: a) D1, b) D2, c) D3, and d) D4.

.

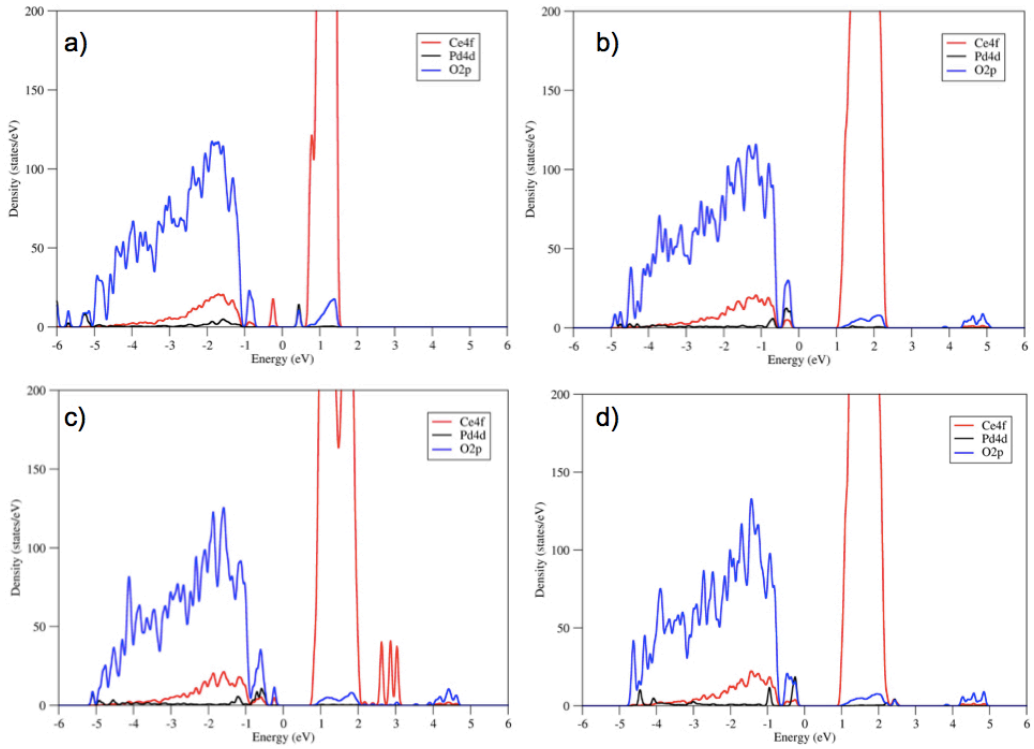

Figure 4.9. DOS plots of $PdCe_{39}O_{79}$ with Pd located in the following positions: a) D1, b) D2, c) D3, and d) D4.

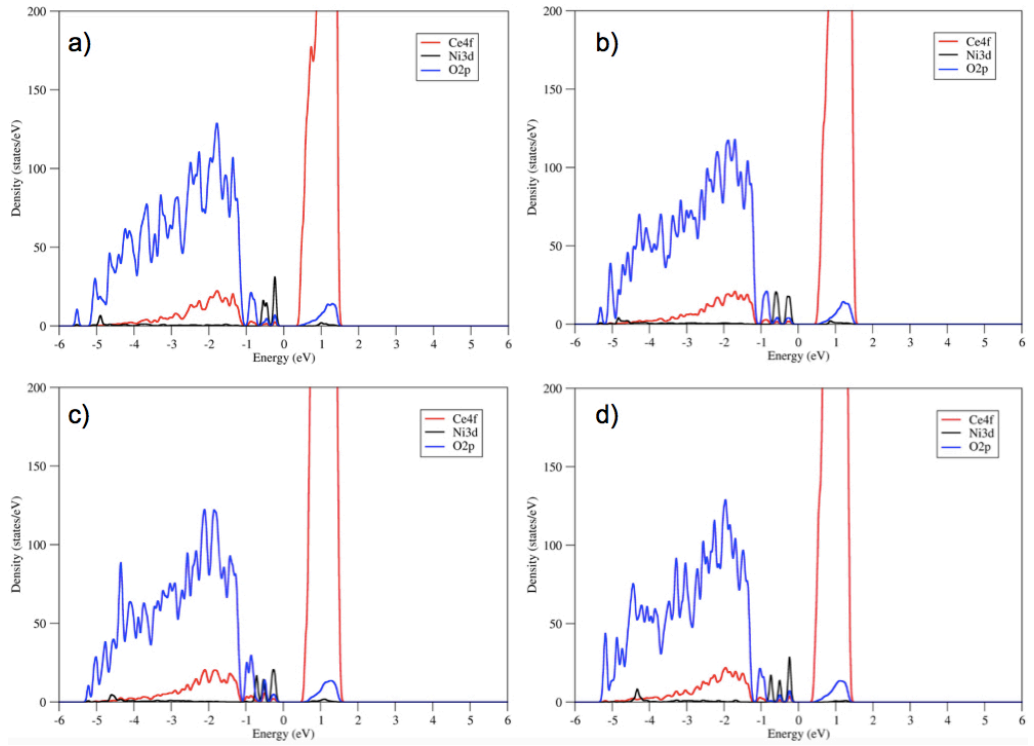

Figure 4.10. DOS plots of $NiCe_{39}O_{79}$ with Ni located in the following positions: a) D1, b) D2, c) D3, and d) D4.

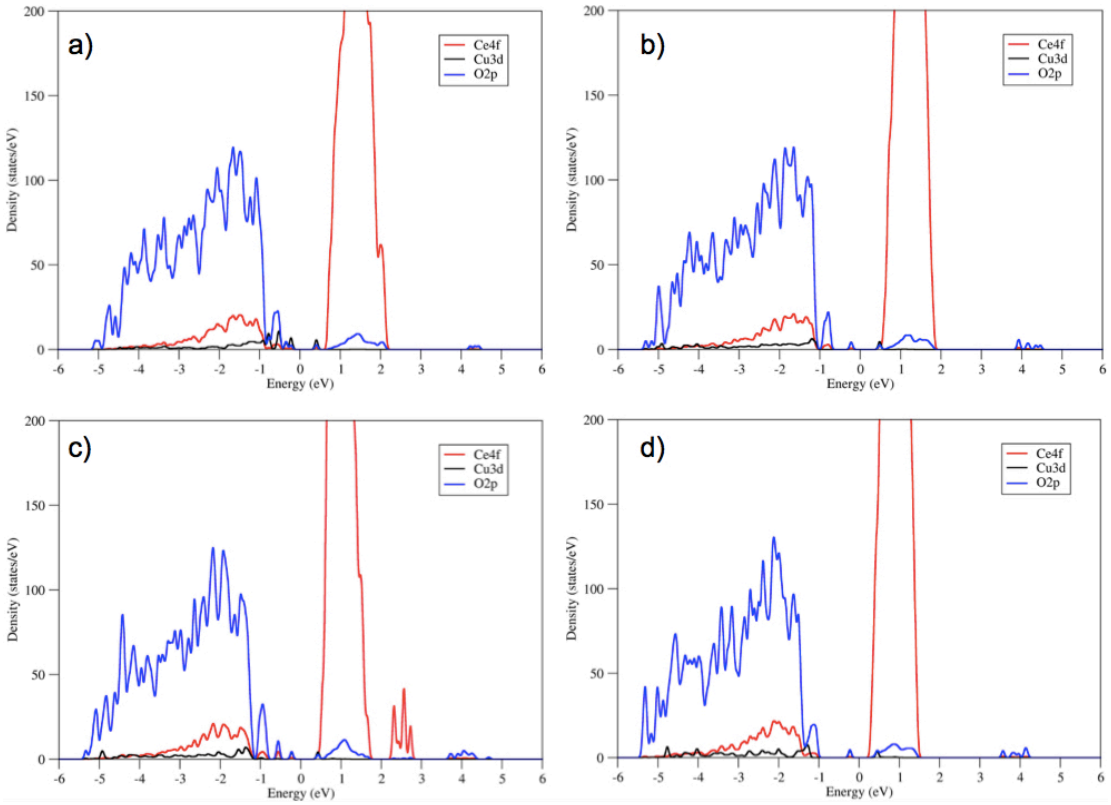

Figure 4.11. DOS plots of $NiCe_{39}O_{79}$ with Cu located in the following positions: a) D1, b) D2, c) D3, and d) D4.

Now we consider the reduction of the $MCe_{30}O_{80}$ NPs due to homolytic dissociative adsorption of H_2, modeled by putting two adsorbed H atoms on top of the two O^{2-} anions nearest to each other on the {100} nanofacet. This process, characterized by the adsorption energy E_H, is analogous to the just discussed O_{vac} formation. It also inserts two electrons in the system, but in a less structurally perturbative way, since no atoms are removed from the NP.

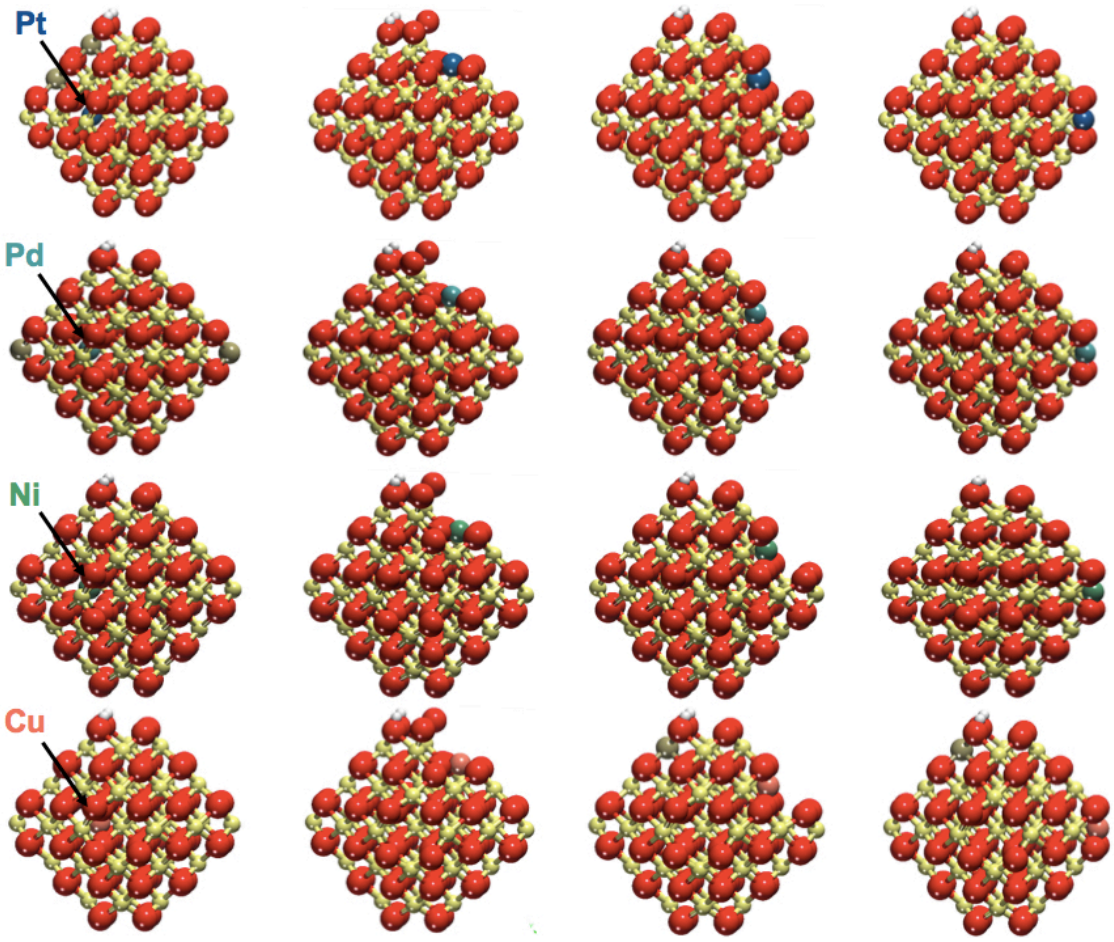

Figure 4.12. Overview of the most stable structures $H_2MCe_{39}O_{80}$ of systems formed upon homolytic dissociative adsorption of two hydrogen atoms in two nearby oxygen atoms of one of the {100} nanofacets.

Particle	D#	E_H kJ mol^{-1}	ΔE kJ mol^{-1}	ΔE_{dop} kJ mol^{-1}	q(M) a.u.	μ(M) μB	n(M)	M-O pm	m
$H_2PtCe_{39}O_{80}$	D1	-144	0	35	1.65	0.00	4	206-209	6
	D2	-249	-155	-121	0.94	0.00	2	202-205	4
	D3	-216	-189	-155	0.99	0.00	2	202-203	4
	D4	-214	-360	-325	0.89	0.00	2	205	4
$H_2PdCe_{39}O_{80}$	D1	-169	0	63	1.52	0.00	4	207-210	6
	D2	-266	-175	-112	0.91	0.00	2	203-205	4
	D3	-242	-212	-149	0.94	0.00	2	202-204	4

	D4	-243	-376	-313	0.83	0.00	2	205 4
$H_2NiCe_{39}O_{80}$	D1	-175	0	11	1.24	0.00	2	199-210 4
	D2	-245	-197	-186	1.05	0.00	2	188-189 4
	D3	-223	-237	-227	1.10	0.00	2	187-189 4
	D4	-216	-384	-374	1.12	0.39	2	185-190 4
$H_2CuCe_{39}O_{80}$	D1	-257	0	-25	1.11	0.51	2	195-198 4
	D2	-227	-69	-95	1.03	0.47	2	196-199 4
	D3	-212	-117	-143	1.18	0.03	3	186-189 4
	D4	-212	-280	-305	1.13	0.00	3	187-188 4

[a] E_H = -171 kJ mol^{-1} for these O positions in the pristine $Ce_{40}O_{80}$ particle.[24]

Table 4.3. Calculated properties of ceria NPs with H_2 dissociatively adsorbed on O atoms of a {100} nanofacet and one Ce atom in the position D# substituted by a doping atom M = Pt, Pd, Ni, Cu. E_H – adsorption energy per H atom, $E_H = ½[E(H_2MCe_{39}O_{80}) - E(MCe_{39}O_{80}) - E(H_2)]$;[a] other notations as in Table 4.1.

The adsorption of two H atoms on the $MCe_{30}O_{80}$ models similarly affects the oxidation states of the Pt, Pd, and Ni atoms (Table 3) as formation of an O_{vac} does: in the surface positions D2-D4 all these M atoms adopt the +2 state, with only inner site D1 dopants Pt and Pd featuring the +4 state in the common 6+2 coordination. Cu dopant is affected by the H adsorbates somewhat differently. For Cu in D3 and D4 positions the essentially zero magnetization is indicative of an odd oxidation state. Together with the slightly higher Bader charges than those in D1 and D2 positions, we assign +3 states to Cu dopant in D3 and D4 positions. Similarly to O_{vac} formation, presence of M dopants stabilizes the dissociative H_2 adsorption (Table 4.3) with respect to the adsorption on the pure ceria NP. For instance, Pt dopant in D2 position strengthens the H_2 adsorption by 78 to -249 kJ mol^{-1}. We associate such enhancement of the adsorption exothermicity with the factors that also stabilized the O_{vac} formation: somewhat depleted O2p states in $MCe_{39}O_{80}$ are easily filled and M dopants in uncommon oxidation states are favorably reduced by the dissociative adsorption of H_2. There, the considered reduction by H_2 can also be understood as a charge compensating reduction process.

In general, calculated E_H values for surface substitutions are higher in magnitude than E_H values of inner substitutions. This trend is not maintained only by Cu, for which E_H = -257 kJ mol^{-1} is higher than E_H values for surface substitutions by all other M.

Regarding doping energies, only Cu atom seems to be slightly energetically favoured to substitute an inner Ce atom, ΔE_{dop} = -25 kJ mol^{-1}. At variance, all surface substitutions by dopants M are found to be definitely exothermic. Surface doping by Ni is the most energetically favoured with ΔE_{dop} of -186, -227, and -374 kJ mol^{-1} for D2, D3, and D4 positions, respectively. For each considered M atom corner position D4 is the most prone to be substituted, with energies of -325, -313, -374, and -305 kJ mol^{-1} for Pt, Pd, Ni, and Cu, respectively.

4.4. Overview

Substitution of a Ce atom by a doping transition metal atom M = Pt, Pd, Ni, and Cu, in four different positions of the representative $Ce_{40}O_{80}$ NP has been investigated by means of DF calculations.

Our calculations showed that surface positions of the NP are more prone to accommodate the M dopants than bulk positions for all metals considered. In particular, the most stable substitutions take place at corner positions of the ceria NP, highlighting the relevance of under-coordinated sites for the stabilization of atomically dispersed transition metal atoms on ceria. Upon the substitution of a Ce^{4+} cation the +4 oxidation states of M dopants are energetically favorable only for Pd and Pt in bulk-like (inner) positions of the unreduced ceria NP.

We explored two redox processes to analyze the stability of the dopants in lower oxidation states and to study the effect of doping on the reducibility of the resulting system. In particular, we have considered the formation of oxygen vacancies and the dissociative adsorption of molecular hydrogen. An O vacancy has been created by removing one oxygen atom from the {100} nanofacet that contains the least coordinated, and thus, most weakly bound oxygen atoms in the ceria NP under scrutiny. Upon O vacancy formation, surface Pt, Pd and Ni dopants are calculated to feature +2 oxidation states and each is bound to four O^{2-} anions in a square-planar fashion. Pt and Pd dopants inside ceria particles can be stabilized in the +4 state as was previously detected by XPS measurements. In turn, we calculated Cu to feature +2 states in both surface and inner positions. Similarly to creating an O vacancy, the homolytic dissociative adsorption of H_2 also results in the donation of two electrons to the ceria particle. Not unexpectedly, similar oxidation states of the doping metals are found when H_2 species is dissociatively adsorbed. The only noticeable difference is that Cu could acquire either +2 or +3 oxidation state, depending on its location.

The present findings provide new insights into how atomically dispersed transition metals can be stabilized in Ce lattice positions at the surface of nanoparticulate ceria. These results indicate that combining doping with nanostructuring of ceria supports leads to catalytic materials where atomically dispersed metal dopants are stabilized with

local structures different from those in extended systems, suggesting new strategies for the preparation of cost-effective catalytic materials.

4.5. References

(1) Flytzani-Stephanopoulos, M.; Gates, B. C. Atomically Dispersed Supported Metal Catalysts. *Annu. Rev. Chem. Biomol. Eng.* **2012**, *3*, 545–574.

(2) Yang, X.-F.; Wang, A.; Qiao, B.; Li, J.; Liu, J.; Zhang, T. Single-Atom Catalysts: A New Frontier in Heterogeneous Catalysis. *Acc. Chem. Res.* **2013**, *46*, 1740–1748.

(3) Flytzani-Stephanopoulos, M. Gold Atoms Stabilized on Various Supports Catalyze the Water–Gas Shift Reaction. *Acc. Chem. Res.* **2014**, *47*, 783–792.

(4) Hu, Z.; Li, B.; Sun, X.; Metiu, H. Chemistry of Doped Oxides: The Activation of Surface Oxygen and the Chemical Compensation Effect. *J. Phys. Chem. C* **2011**, *115*, 3065–3074.

(5) McFarland, E. W.; Metiu, H. Catalysis by Doped Oxides. *Chem. Rev.* **2013**, *113*, 4391–4427.

(6) Delmon, B. Preparation of Heterogeneous Catalysts: Synthesis of Highly Dispersed Solids and Their Reactivity. *J. Therm. Anal. Cal.* **2007**, *90*, 49–65.

(7) Delmon, B. J.; Jacobs, P. A.; Poncelet, G. *Preparation of Catalysts*; Elsevier: Amsterdam, 1976.

(8) Pernicone, N.; Traina, F. *Applied Idustrial Catalysis*; Leach, B. E., E., Ed.; Academic press: New York, 1984.

(9) Richardson, G. T. *Principles of Catalyst Development*; Plenum: New York, 1989.

(10) Elias, J. S.; Risch, M.; Giordano, L.; Mansour, A. N.; Shao-Horn, Y. Structure, Bonding, and Catalytic Activity of Monodisperse, Transition-Metal-Substituted CeO_2 Nanoparticles. *J. Am. Chem. Soc.* **2014**, *136*, 17193–17200.

(11) Gulyaev, R. V.; Kardash, T. Y.; Malykhin, S. E.; Stonkus, O. A.; Ivanova, A. S.; Boronin, A. I. The Local Structure of $Pd_xCe_{1-x}O_{2-X-\Delta}$ Solid Solutions. *Phys. Chem. Chem. Phys.* **2014**, *16*, 13523–13539.

(12) Capdevila-Cortada, M.; Łodziana, Z.; Lopez, N. On the Performance of DFT+U Approaches in the Study of Catalytic Materials. *ACS Catal.* **2016**, acscatal.6b01907.

(13) Farra, R.; García-Melchor, M.; Eichelbaum, M.; Hashagen, M.; Frandsen, W.; Allan, J.; Girgsdies, F.; Szentmiklósi, L.; López, N.; Teschner, D. Promoted Ceria: A Structural, Catalytic, and Computational Study. *ACS Catal.* **2013**, *3*, 2256–2268.

(14) Capdevila-Cortada, M.; García-Melchor, M.; López, N. Unraveling the Structure Sensitivity in Methanol Conversion on CeO_2: A DFT+U Study. *J. Catal.* **2015**, *327*, 58–64.

(15) Yang, Z.; Luo, G.; Lu, Z.; Hermansson, K. Oxygen Vacancy Formation Energy in Pd-Doped Ceria: A DFT+U Study. *J. Chem. Phys.* **2007**, *127*, 74704.

(16) Yang, Z.; Luo, G.; Lu, Z.; Woo, T. K.; Hermansson, K. Structural and Electronic Properties of NM-Doped Ceria (NM = Pt, Rh): A First-Principles Study. *J. Phys. Condens. Matter* **2008**, *20*, 35210.

(17) Scanlon, D. O.; Morgan, B. J.; Watson, G. W. The Origin of the Enhanced Oxygen Storage Capacity of $Ce_{(1-x)}(Pd/Pt)_{(x)}O_2$. *Phys. Chem. Chem. Phys.* **2011**, *13*, 4279–4284.

(18) Wang, X.; Shen, M.; Wang, J.; Fabris, S. Enhanced Oxygen Buffering by Substitutional and Interstitial Ni Point Defects in Ceria: A First-Principles DFT+U Study. *J. Phys. Chem. C* **2010**, *114*, 10221–10228.

(19) Mayernick, A. D.; Janik, M. J. Methane Oxidation on Pd–Ceria: A DFT Study of the Mechanism over $Pd_xCe_{1-x}O_2$, Pd, and PdO. *J. Catal.* **2011**, *278*, 16–25.

(20) Tang, W.; Hu, Z.; Wang, M.; Stucky, G. D.; Metiu, H.; McFarland, E. W. Methane Complete and Partial Oxidation Catalyzed by Pt-Doped CeO_2. *J. Catal.* **2010**, *273*, 125–137.

(21) Schauermann, S.; Nilius, N.; Shaikhutdinov, S.; Freund, H. J. Nanoparticles for Heterogeneous Catalysis: New Mechanistic Insights. *Acc. Chem. Res.* **2013**, *46*, 1673–1681.

(22) Kuhlenbeck, H.; Shaikhutdinov, S.; Freund, H.-J. Well-Ordered Transition Metal Oxide Layers in Model Catalysis – A Series of Case Studies. *Chem. Rev.* **2013**, *113*, 3986–4034.

(23) Matolín, V.; Matolínová, I.; Václavů, M.; Khalakhan, I.; Vorokhta, M.; Fiala, R.; Piš, I.; Sofer, Z.; Poltierová-Vejpravová, J.; Mori, T.; Potin, V.; Yoshikawa, H.; Ueda, S.; Kobayashi, K. Platinum-Doped CeO_2 Thin Film Catalysts Prepared by Magnetron Sputtering. *Langmuir* **2010**, *26*, 12824–12831.

(24) Fiala, R.; Figueroba, A.; Bruix, A.; Vaclavu, M.; Rednyk, A.; Khalakhan, I.; Vorokhta, M.; Lavkova, J.; Illas, F.; Potin, V.; Matolinova, I.; Neyman, K. M.; Matolin, V. High Efficiency of Pt^{2+}- CeO_2 Novel Thin Film Catalyst as Anode for Proton Exchange Membrane Fuel Cells. *Appl. Catal. B Environ.* **2016**, *197*, 262–270.

(25) Figueroba, A.; Kovács, G.; Bruix, A.; Neyman, K. M. Towards Stable Single-Atom Catalysts: Strong Binding of Atomically Dispersed Transition Metals on the Surface of Nanostructured Ceria. *Catal. Sci. Technol.* **2016**, *6*, 6806 – 6813.

(26) Sk, M. A.; Kozlov, S. M.; Lim, K. H.; Migani, A.; Neyman, K. M. Oxygen Vacancies in Self-Assemblies of Ceria Nanoparticles. *J. Mater. Chem. A* **2014**, *2*, 18329–18338.

(27) Migani, A.; Vayssilov, G. N.; Bromley, S. T.; Illas, F.; Neyman, K. M. Greatly Facilitated Oxygen Vacancy Formation in Ceria Nanocrystallites. *Chem. Commun.* **2010**, *46*, 5936.

(28) Migani, A.; Vayssilov, G. N.; Bromley, S. T.; Illas, F.; Neyman, K. M. Dramatic Reduction of the Oxygen Vacancy Formation Energy in Ceria Particles: A Possible Key to Their Remarkable Reactivity at the Nanoscale. *J. Mater. Chem.* **2010**, *20*, 10535–10546.

(29) Vayssilov, G. N.; Migani, A.; Neyman, K. Density Functional Modeling of the Interactions of Platinum Clusters with CeO_2 Nanoparticles of Different Size. *J. Phys. Chem. C* **2011**, *115*, 16081–16086.

(30) Bruix, A.; Lykhach, Y.; Matolínová, I.; Neitzel, A.; Skála, T.; Tsud, N.; Vorokhta, M.; Stetsovych, V.; Ševčíková, K.; Myslivečeк, J.; Fiala, R.; Václavů, M.; Prince, K. C.; Bruyère, S.; Potin, V.; Illas, F.; Matolín, V.; Libuda, J.;

Neyman, K. M. Maximum Noble-Metal Efficiency in Catalytic Materials: Atomically Dispersed Surface Platinum. *Angew. Chemie Int. Ed.* **2014**, *53*, 10525–10530.

(31) Neitzel, A.; Figueroba, A.; Lykhach, Y.; Skála, T.; Vorokhta, M.; Tsud, N.; Mehl, S.; Ševčíková, K.; Prince, K. C.; Neyman, K. M.; Matolín, V.; Libuda, J. Atomically Dispersed Pd, Ni, and Pt Species in Ceria-Based Catalysts: Principal Differences in Stability and Reactivity. *J. Phys. Chem. C* **2016**, *120*, 9852–9862.

(32) Colussi, S.; Gayen, A.; Camellone, M. F.; Boaro, M.; Llorca, J.; Fabris, S.; Trovarelli, A. Nanofaceted Pd-O Sites in Pd-Ce Surface Superstructures: Enhanced Activity in Catalytic Combustion of Methane. *Angew. Chem. Int. Ed.* **2009**, *48*, 8481–8484.

(33) Carrasco, J.; López-Durán, D.; Liu, Z.; Duchoň, T.; Evans, J.; Senanayake, S. D.; Crumlin, E. J.; Matolín, V.; Rodríguez, J. A.; Ganduglia-Pirovano, M. V. In Situ and Theoretical Studies for the Dissociation of Water on an Active Ni/CeO_2 Catalyst: Importance of Strong Metal-Support Interactions for the Cleavage of O-H Bonds. *Angew. Chem. Int. Ed.* **2015**, *54*, 3917–3921.

CHAPTER FIVE

Interplay of Pt^{4+} and Pt^{2+} doping species in CeO_2: Role of nanostructuring

5.1. Introduction

Development of cost-efficient materials for low-temperature oxidation reactions is among the main objectives in catalysis science. Oxygen storage capacity (OSC) of the oxidation catalytic materials appears to be one of their most relevant properties. Materials with enhanced OSC are useful for achieving good conversion rates at relatively low temperatures.[1] One of the ways for tuning the OSC of an oxide catalyst support is to dope it with transition metal atoms. Transition metal dopants can be introduced in the lattice of the oxide support by substituting metal cations in it. This process facilitates release of O atoms located near the dopants due to the different local coordination environment the dopants induce. These more easily released O atoms are more reactive and mobile than other lattice O atoms, which can enhance performance of the corresponding oxidative catalysts.

One of the supports known for their high OSC is ceria. CeO_2-based materials are widely used in the production of TWCs,[2,3] low-temperature oxidation of CO,[4] water gas shift reaction and selective methanation,[5,6] CH_x oxidation[7] and other reactions. Enhancement of the OSC of ceria provides higher conversion efficiency and resistance to thermal ageing of catalysts, being able to remove exhaust gases such as hydrocarbons, CO and NO_x.[2,3] The ability of ceria to cycle between Ce^{4+} and Ce^{3+} states makes it a key component for applications in exhaust catalysts. Extensive research has been performed in this area. One of the pertinent questions is how the OSC of ceria functions at the atomic level. A deeper understanding of such processes may allow not only to boost the development of improved and more efficient TWCs but also to pave the ways for new catalysts for low-temperature oxidation reactions.

Many factors can modify the OSC of CeO_2-based materials. For instance, it was demonstrated that there exists a strong dependency of the OSC on the specific shape of ceria crystallites. This strongly suggests that CeO_2-based materials should be designed with preferential exposure of specific surface crystallographic facets, i.e., with higher fraction of reactive {100} and {110} facets, which feature low coordinated O atoms.[8]

Pure ceria is not stable at very high temperatures and partially loses its OSC properties.[2,3,9] One of the approaches to stabilize ceria at moderately high temperatures

in order to maintain the important OSC properties is to dope it with rare earth elements. Addition of small amount of La_2O_3 can improve heat resistance of ceria. This is related to the increase in the lattice constant of ceria host with increasing content of lanthanum, due to the larger ionic radius of La^{3+} with respect to that of the Ce^{4+} cation. Furthermore, O_{vac} are formed in order to compensate the +3 charge of La ions. These released O atoms can diffuse to the surface and be involved in catalytic oxidative processes.[10] Improvements in the OSC of ceria were also noticed after addition of ZrO_2.[11-14] Upon incorporation of increasing amounts of Zr ions, facilitated reduction of ceria was observed by TPR and XRD techniques. The formation of highly mobile O atoms is facilitated due to smaller ionic radius of Zr, which favors the presence of Ce^{3+} in the lattice of ceria by decreasing the strain associated with their formation.

As mentioned in Chapter 4, bulk and slab models have been used to computationally study effects metal dopants introduced in the lattice of ceria.[16-20]

To the best of our knowledge, published theoretical studies of the effects of metal doping on the OSC of ceria have been performed using either bulk or slab models. Hence, we consider worthwhile to study how the formation of oxygen vacancies is affected by the presence of Ce-substituting Pt atoms in nanoparticulate models. Such nano-architectures provide a number of both inner and surface sites, which can be relevant for tuning the OSC of ceria. For comparing the effects introduced by nanostructuring, we also have performed density-functional calculations of bulk models.

5.2. Models

Bulk ceria has been modeled using the optimal PW-91 lattice parameter of 548 pm[21] with a (2×2×2) sampling including 96 atoms in the supercell (Figure 5.1). The inclusion of one Pt atom in the lattice of the oxide support has been performed by substitution of one Ce atom.

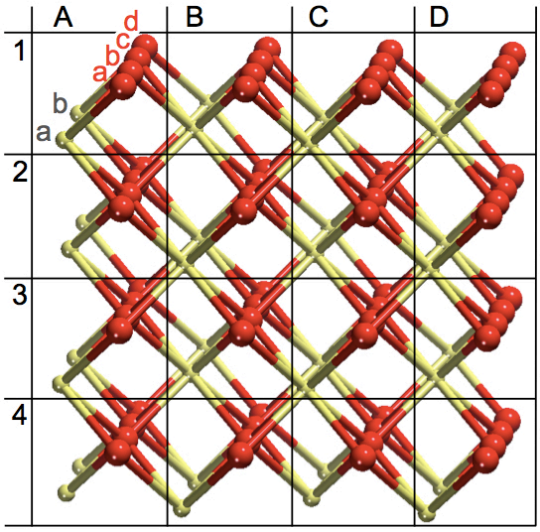

Figure 5.1. Overview of the (2×2×2) bulk cut used for modelling CeO_2. Yellow and red spheres correspond Ce and O atoms, respectively. Numbers, capital letters and small letters label crystal positions in order to define location of O vacancies and Ce^{3+} cations. As an example, O atoms located at the top-left side of the picture are denoted as A1a, A1b, A1c and A1d, respectively.

Details on the models used for representing ceria NPs can be found in Chapter 3. Similarly to the case of bulk systems, inclusion of one Pt atom in the lattice of ceria has been performed by substitution of one Ce atom.

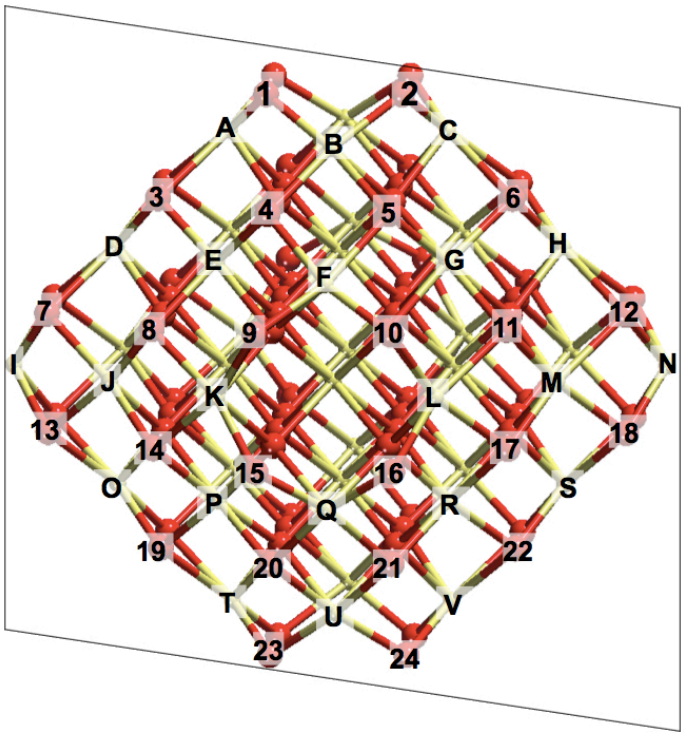

Figure 5.2. Overview of the $Ce_{40}O_{80}$ model. Yellow and red spheres correspond to Ce and O atoms, respectively. The transparent plane divides the nanoparticle in two symmetric halves. Numbers and capital letters label positions of O vacancies and Ce^{3+} cations, respectively.

5.3. Results and discussion

Here, we present the results for insertion of the noble metal Pt into the lattice of both bulk and NP ceria as Ce-substitutional defect. Different Pt-doped CeO_2 NP systems with increasing noble metal content are discussed. Comparative calculations of Pt-doped bulk ceria have been performed in order to emphasize effects arising upon the nanostructuring. To this end, we analyzed how the latter affects the OSC of ceria.

Bulk systems

Let us start analyzing the results calculated for the inclusion of a Pt atom in the lattice of bulk ceria. In the ceria FCC lattice, Ce^{4+} cations are surrounded by 8 O^{2-} anions (Figure 5.3a) with the optimized interatomic Ce-O distances of 237 pm. Substitution of a Ce atom by Pt one results in the Pt-O distances of 229 pm.

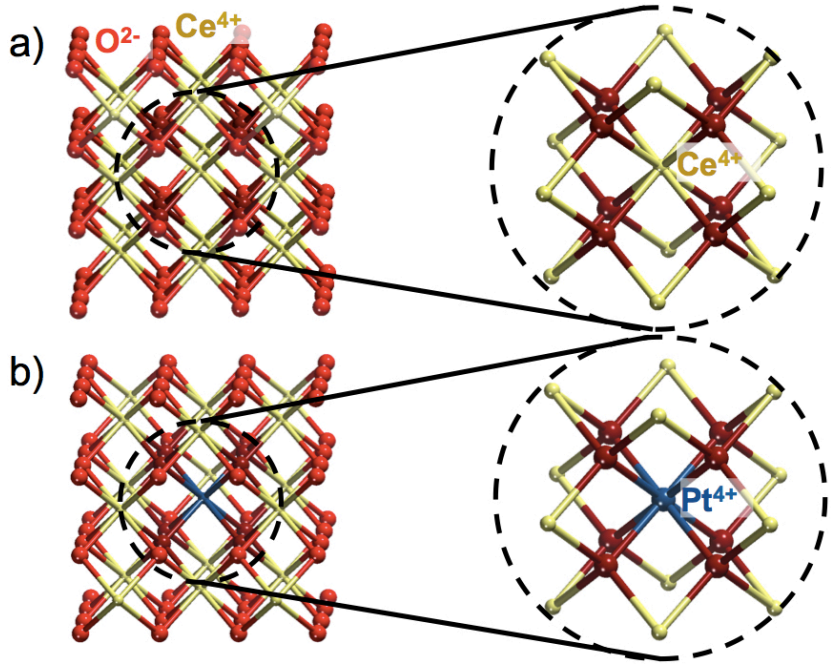

Figure 5.3. Overview of stoichiometric models a) CeO_2 and b) Pt/CeO_2. Yellow, red and blue spheres correspond to Ce, O and Pt atoms respectively. Dark red spheres indicate O^{2-} ions closest to substituted Ce and Pt.

System	ΔE, kJ mol^{-1}	E_{vac}, kJ mol^{-1}	*q*, a.u.	M-O, pm	O_{vac} ; Ce^{3+}
2×2×2					
CeO_2	-	-	2.37 (Ce^{4+})		-; -
CeO_2 O_{vac}	-	321	2.29 (Ce^{4+})	7×224-236	C3c; C3b,C4a
Pt/CeO_2	0	-	1.60 (Pt^{4+})	6×210, 2×294	-; -
Pt/CeO_2	164	-	1.33 (Pt^{4+})	8×229	-; -
Pt/CeO_2 O_{vac}	0	200	1.58 (Pt^{4+})	6×209, 1×292	C2c; C2b,A2a
Pt/CeO_2 O_{vac}	2	202	1.59 (Pt^{4+})	6×208-210, 1×296	C2c; C4a,D2a
Pt/CeO_2 O_{vac}	1	201	1.58 (Pt^{4+})	6×209, 1×292	C2c; A2a,C4a
Pt/CeO_2 O_{vac}	0	200	1.58 (Pt^{4+})	6×209, 1×292	C2c; C2b,C4a
Pt/CeO_2 $2O_{vac}$	-	223	1.57 (Pt^{4+})	6×207-210	B3b,C2c; B2a,B3b, C4a, D2a
Pt/CeO_2 $3O_{vac}$	-	198	0.87 (Pt^{2+})	4×207-208, 1×287	B2a,B3a,C4a,D2a
Pt/CeO_2 O_{vac}	-	103	1.03 (Pt^{2+})	4×200	C2c; -
Pt/CeO_2 $2O_{vac}$	-	265	1.00 (Pt^{2+})	4×199-200	C2b,C2c;C1a,D1a
Pt/CeO_2 $3O_{vac}$	-	257	0.97 (Pt^{2+})	4×199-200	C2b,C2c,C3b; C1a,D1a,D2a,D3a
3×3×3					
Pt/CeO_2	-	-	1.60 (Pt^{4+})	6×210-211, 2×290	-
Pt/CeO_2 O_{vac}	-	189	1.61 (Pt^{4+})	6×208-211, 1×296	C3c; C1b,C3a
Pt/CeO_2 O_{vac}	-	83	1.03 (Pt^{2+})	4×200	C2c; -

Table 5.1. Energies ΔE with respect to the most stable structure for each system and O vacancy formation energies E_{vac} of bare and Pt-doped ceria bulk structures. Bader charge *q* and oxidation state of Ce and Pt are also given. Ce-O and Pt-O are distances to O atoms located in the first coordination sphere. Positions of O vacancies and Ce^{3+} cations are indicated using labels introduced in Figure 5.1.

Pt atom substituting a Ce atom in stoichiometric (without O_{vac}) ceria by electro-neutrality has to feature the oxidation state of Ce, i.e. +4. Nevertheless, Bader charge of Pt atom in a cubic coordination environment is 1.33 a.u. (see Table 5.1). This charge value is lower than ca. 1.6 a.u. that Pt^{4+} cations exhibit in more typical environments. In addition, small magnetization values (of 0.08 μB) have been computed on each of the closest to Pt 8 O anions forming the first coordination sphere with Pt-O distances of 229 pm. Pt is known to feature such high oxidation state +4 in octahedral complexes. Thus, we distorted the initial coordination around Pt consisting of 8 O^{2-} by shortening 6 and elongating two Pt-O distances to give an octahedral [6+2] coordination. Local geometry optimization of this initial arrangement with Pt in the [6+2] coordination (Figure 5.4) resulted in a structure, which is by 164 kJ mol^{-1} more stable than the structure with Pt in a cubic-like coordination. In the octahedral coordination 6 Pt-O distances of 210 pm and 2 Pt-O distances of 294 pm (Table 5.1) are obtained. Pt accommodated in this [6+2] coordination environment features a Bader charge value of 1.60 a.u. (Table 5.1), without any magnetization of the nearby O atoms. We can thus associate the small magnetization values on the 8 O atoms with the instability of Pt in the +4 state, when it is located in the original cubic-like position of Ce. Substitutional Pt^{4+} cation in ceria, which stabilizes the octahedral environment, displaces two O atoms out of the first coordination sphere. These less coordinated O atoms become more weakly bound and are more easily released from the material.

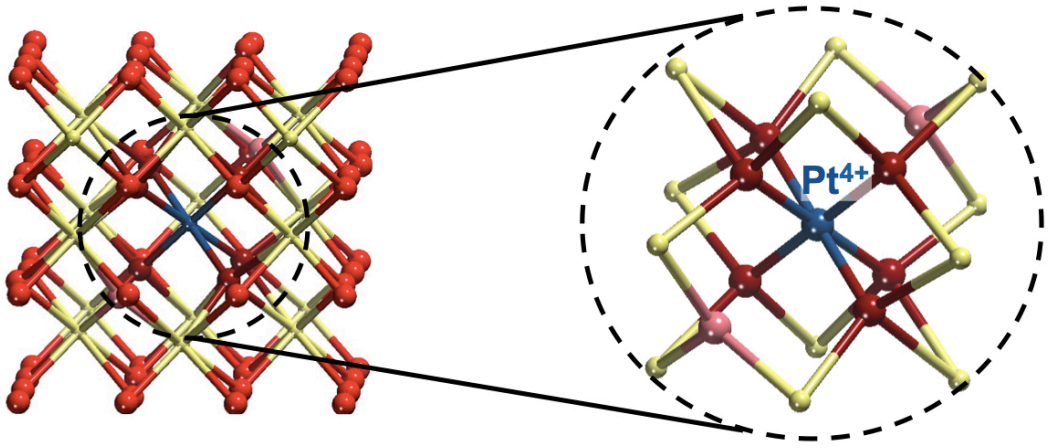

Figure 5.4. Pt/CeO_2 structure with Pt^{4+} featuring octahedral coordination of six nearby plus two more distant O atoms [6+2]. Yellow, red and blue spheres represent Ce, O and Pt atoms, respectively. Dark red and pink spheres correspond to the O^{2-} ions closest to and somewhat more distant from Pt, respectively.

Let us consider now how the OSC of bulk ceria is affected by the Pt dopant. To do so, we have compared the energy required for removing one of the O atoms from the first coordination sphere of either Ce or Pt (Figure 5.5). O vacancy formation energies E_{vac} are shown in Table 5.1. For releasing an O atom from bare ceria 321 kJ mol^{-1} is required. The removal of an O atom leaves two electrons in the system reducing two Ce^{4+} cations to Ce^{3+}. Ce-O bond lengths do not change significantly upon release of the O atom, all 7 being in the range of 226-234 pm (Table 5.1). When atomic Pt is introduced in the ceria lattice, the electrons left by the O atom can be accepted by two different entities resulting in the following reduction processes: 1) reduction of two Ce^{4+} cations to Ce^{3+}, with Pt maintaining the +4 state or 2) reduction of the noble metal to the +2 state, without formation of Ce^{3+} cations. In the first case, the energy required to form the O_{vac} is 200 kJ mol^{-1}. The presence of Pt causes a significant decrease (by 121 kJ mol^{-1}) of the energy required to form an O_{vac} in bulk ceria. Bader charge of Pt, 1.58 a.u., is barely changed compared to the stoichiometric situation, 1.60 a.u. Pt-O distances remain very similar upon O removal: 6 short 209 pm and one long 292 pm.

At variance, reduction of Pt^{4+} to Pt^{2+} induces a significant lattice distortion moving the metal atom away from the initial position of Ce. In this new environment, Pt^{2+} is located in the center of a square of four O^{2-} ions adopting a square-planar coordination and leaving three less coordinated O^{2-} ions. The reduction of Pt to the +2 state during this process is reflected in no Ce^{3+} cations formed and in lower Bader charge value for Pt, 1.03 a.u. Four Pt-O distances of 200 pm are obtained. Here, the energy required for removing an O atom drops dramatically, from 321 kJ mol^{-1} in the undoped system to 103 kJ mol^{-1}. The latter E_{vac} value is significantly lower than 200 kJ mol^{-1} calculated in the previously addressed situation with Pt^{4+}. We associate such facilitated reduction process with the energy cost required to form Ce^{3+} species, when Pt maintains the +4 state. Formation of Ce^{3+} ions causes steric constraints in the material due to their larger volume with respect to Ce^{4+}, which destabilize the entire system. Nevertheless, presence of Pt^{4+} in the lattice of bulk ceria is possible, due to the endothermicity of the both just discussed reduction processes. Even though, formation of Pt^{2+} species upon release of O atoms in bulk ceria is favored thermodynamically in our models.

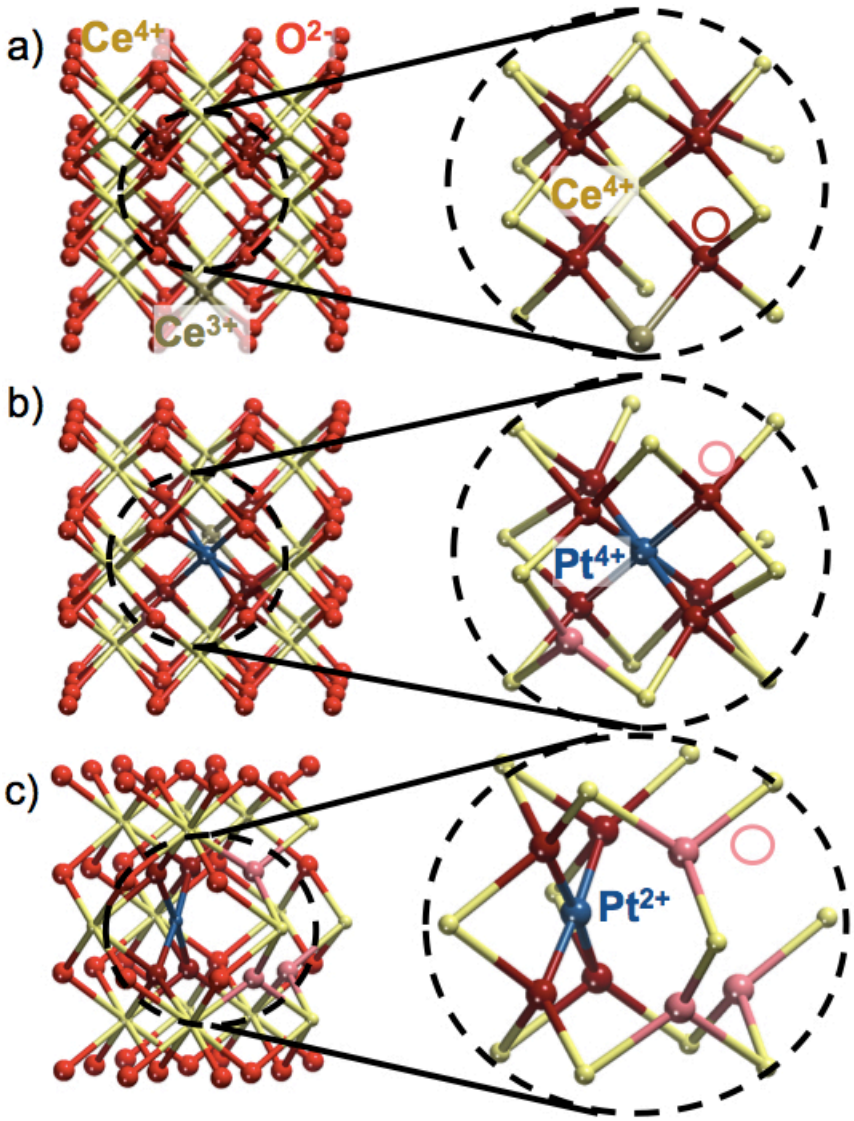

Figure 5.5. Structures calculated after formation of an O vacancy in bulk CeO_2 nearby a) Ce^{4+} cations; b) Pt^{4+} cation; c) Pt^{2+} cation. Yellow, red and blue spheres represent Ce, O and Pt atoms respectively. Dark red and pink spheres correspond to the O^{2-} ions closest to and somewhat distant from Pt, respectively. Position of the O_{vac} is indicated by an empty circle.

Curiously, the presence of substitutional Pt^{4+} species in bulk ceria is commonly considered by computational modelling to be unfavorable. Instability of Pt^{4+} was derived from the calculated result that the reduction of Pt^{4+} to Pt^{2+} takes place spontaneously upon exothermic formation of a charge compensating oxygen vacancy, E_{vac} = -72 kJ mol^{-1}.[19] Such behavior has been understood in terms of large lattice distortion at the Pt center required to form the square-planar [PtO_4] moiety. Forming the O_{vac} nearby a Pt^{4+} cation and two Ce^{3+} cations was computed to require 115 kJ mol^{-1}. Attempting to reproduce these computational findings, we noticed that results of work

[19] were obtained using for computing of the E_{vac} an initial state reference, where Pt is in the cubic environment of 8 O atoms. We calculated this cubic coordination to be 164 kJ mol^{-1} less stable than the [6+2] coordination. Therefore, the previously calculated to be exothermic O_{vac} formation resulting in Pt^{2+}, E_{vac} = -72 kJ mol^{-1}, turns out to be endothermic, E_{vac} = 103 kJ mol^{-1}, when a more stable initial state reference system with the [6+2] coordination environment of Pt dopant is used.

To consider formation of the second O_{vac} (Figure 5.6), we removed another low-coordinated O atom surrounding Pt. With Pt in the octahedral coordination 223 kJ mol^{-1} is required for removing the second O atom. It is 21 kJ mol^{-1} more than required to form the first O_{vac}. Such increase in E_{vac} is a consequence of the reduction of two extra Ce^{4+} cations to Ce^{3+} by electrons left in the system by the removed O. Bader charge of Pt, 1.57 a.u., and Pt-O distances, 207-210 pm, do not change noticeably upon formation of such second O_{vac}. Formation of the second vacancy nearby Pt in the square-planar coordination results in E_{vac} = 265 kJ mol^{-1}, which is 23 kJ mol^{-1} higher than for the first O_{vac}. Again, the E_{vac} increase can be associated with the presence of two extra Ce^{3+} cations in the lattice of ceria. Bader charge value of 1.00 a.u. and four short Pt-O distances of 199-200 pm are calculated.

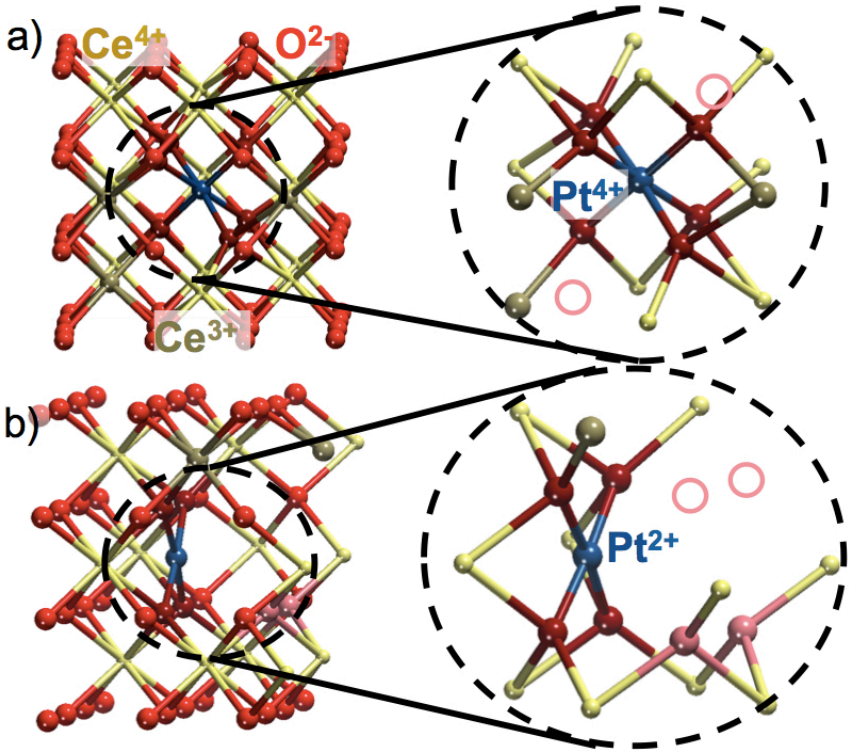

Figure 5.6. Structures calculated after formation of the second O vacancy in the doped CeO_2 nearby a) Pt^{4+} cation; b) Pt^{2+} cation. Yellow, red and blue spheres represent Ce, O and Pt atoms, respectively. Dark red and pink spheres correspond to the O^{2-} ions closest to and somewhat distant from Pt, respectively. Positions of O_{vac} are indicated by empty circles.

Formation of the third O vacancy near Pt^{4+} destroys the octahedral coordination of this M center (Figure 5.7a). Upon removal of the O atom, four of the remaining O atoms rearrange their bonds around Pt to form a square-planar [PtO_4] moiety. Pt can no longer be stabilized in the high oxidation state +4 and becomes reduced to the +2 state. This process is reflected in the Bader charge value of Pt decreasing in this specific coordination to 0.87 a.u. Therefore, octahedral coordination of Pt with 6 O atoms can only be maintained up to formation of two O_{vac}. Consequently, the electrons left in the system by the removal of the O atom are transferred to the dopant. 198 kJ mol^{-1} is calculated to require for formation of the third vacancy. Four short Pt-O distances of 207-208 pm plus one long distance of 287 pm are calculated. Meanwhile, formation of the third O_{vac} near Pt^{2+} requires 257 kJ mol^{-1}. This high value is a consequence of the reduction of extra Ce^{4+} cations. Pt center is essentially unaltered upon this reduction.

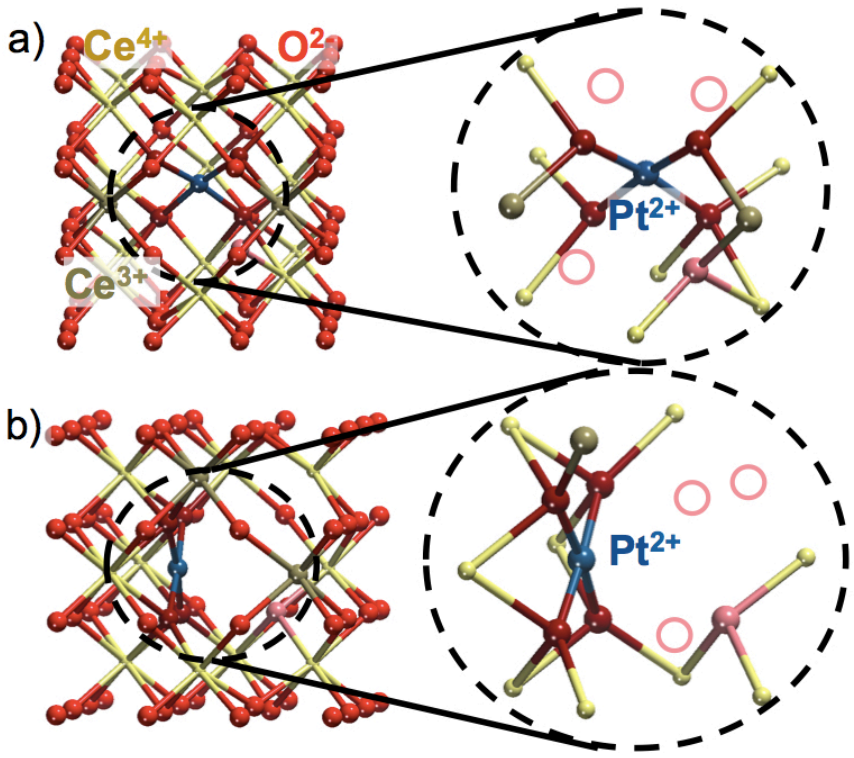

Figure 5.7. Structures calculated after formation of a third O vacancy in the doped CeO_2 nearby the previous a) Pt^{4+} cation; b) Pt^{2+} cation. Yellow, red and blue spheres represent Ce, O and Pt atoms respectively. Dark red and pink spheres correspond to the O^{2-} ions closest to and somewhat distant from Pt, respectively. Positions of O_{vac} are indicated by empty circles.

Nanoparticle systems

Next, our study of Pt-ceria doped systems has been extended using more realistic nanoparticulate models. Such models feature surface defects, which may notably affect the stability of doping centers and, concomitantly, the OSC. In order to account for the effects resulting from the nanostructuring, we employed $Ce_{40}O_{80}$ nanoparticle (Figure 5.2). Doping process has been modelled, like for bulk systems, by inserting a Pt atom as Ce-substitutional defect into the lattice of the ceria NP. Effects of Pt loading have also been considered by including one or four Pt atoms adsorbed at different {100} nanofacets of the ceria NP. Pt atoms adsorbed at such facets feature the +2 state. Two Ce^{4+} cations are reduced to Ce^{3+} per each Pt atom adsorbed.

One Pt atom at the surface of doped nanoparticulate ceria

We start by discussing results obtained for ceria NP systems with one Pt atom adsorbed at the surface. Ce^{4+} in the lattice of ceria NP binds to 8 O^{2-} anions with Ce-O distances of 228-235 pm. Adsorption of Pt on one of the {100} nanofacets results in formation of two Ce^{3+} centers. At variance from the stoichiometric bulk system, the [6+2] environment of Pt (Figure 5.8) is spontaneously obtained upon geometry optimization of the NP without introducing any distortion around the dopant. This result is related to low-coordinated atoms present on the surface. Structure of bulk ceria is much more rigid than that of NPs, thus being more resistant to distortions. The lattice distortions induced by displacements of the two under-coordinated O atoms can be much easier accommodated and distributed through the whole particle compared to the bulk. Pt is found again in the +4 state and features a Bader charge of 1.67 a.u. Octahedral coordination of Pt is obtained, with 6 short Pt-O distances of 205-208 pm and two long distances of 279 pm.

Similarly to bulk systems, formation of the O_{vac} can lead to two situations: 1) maintaining the +4 state of Pt with the concomitant reduction of two Ce^{4+} cations or 2) reduction of Pt^{4+} to Pt^{2+} with the associated large lattice distortion forming the [PtO_4] moiety (Figure 5.8). In bare ceria NP, formation of an O_{vac} requires 202 kJ mol^{-1}. Interestingly, release of one of the more distant O atoms around Pt^{4+} requires only 62 kJ mol^{-1}. This value is 138 kJ mol^{-1} smaller than the E_{vac} obtained for bulk. Enhancement in the OSC of ceria using Pt-doped NP models can be associated with the presence of surface Ce atoms. Lattice is much easier relaxed, if the electrons left by the O atom are accepted by surface Ce ions. Such ions are less coordinated than inner Ce ones, being able to properly distort their surrounding atoms. Pt features a Bader charge of 1.65 a.u. with 6 short Pt-O distances of 203-209 pm and a long one of 287 pm. Formation of the vacancy nearby Pt^{2+} results in E_{vac} = 101 kJ mol^{-1}, 39 kJ mol^{-1} higher than that in the presence of Pt^{4+}.

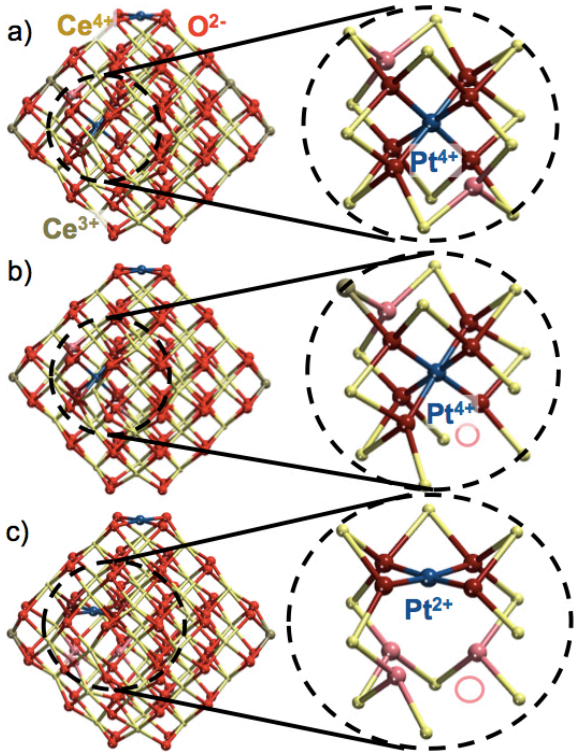

Figure 5.8. Structures of nanoparticles a) stoichiometric $Pt/PtCe_{39}O_{80}$ and b), c) $Pt/PtCe_{39}O_{79}$ in the presence of an O vacancy near b) Pt^{4+} cation; c) Pt^{2+} cation. Yellow, red and blue spheres represent Ce, O and Pt atoms respectively. Dark red and pink spheres correspond to the O^{2-} ions closest to and somewhat distant from Pt, respectively. Position of the O_{vac} is indicated by an empty circle.

The second O_{vac} has been created, like in the bulk systems, by removing one of the O atoms more distant from Pt (Figure 5.9). 191 kJ mol^{-1} is required for forming the second O_{vac} at Pt^{4+}. This value is 129 kJ mol^{-1} higher than calculated for the first O_{vac}. The +4 state of Pt is maintained via formation of two extra Ce^{3+} cations. Bader charge value of 1.67 a.u. for Pt and 6 Pt-O distances of 199-208 pm are computed. 134 kJ mol^{-1} is needed to create O_{vac} near the square-planar coordinated Pt^{2+}, which is substantially lower than the E_{vac} near Pt^{4+}. Therefore, even if the two different Pt-O entities can be formed, we expect the system to thermodynamically evolve preferentially to the $[PtO_4]$ moiety (with Pt^{2+}) upon formation of the second O vacancy.

System	ΔE, kJ mol^{-1}	E_{vac}, kJ mol^{-1}	*q*, a.u.	M-O, pm	O_{vac} ; Ce^{3+}
$Pt/Ce_{40}O_{80}$	-	-	2.34 (Ce^{4+})	8×228-235	-; I,N
$Pt/Ce_{40}O_{79}$	-	202	2.31 (Ce^{4+})	7×223-231	15″; D,I,N,P
$Pt/PtCe_{39}O_{80}$	-	-	1.67 (Pt^{4+})	6×205-208, 2×279	- ; I,N
$Pt/PtCe_{39}O_{80}$	11	-	1.66 (Pt^{4+})	6×205-209, 2×281-291	-; D,H
$Pt/PtCe_{39}O_{79}$	0	62	1.65 (Pt^{4+})	6×203-209, 1×287	15″; D,H,I,N
$Pt/PtCe_{39}O_{79}$	25	87	1.64 (Pt^{4+})	6×203-209, 1×286	15″; D,H,I,P
$Pt/PtCe_{39}O_{79}$	17	80	1.65 (Pt^{4+})	6×202-209, 1×288	15″; I,-J,M, N
$Pt/PtCe_{39}O_{79}$	37	100	1.65 (Pt^{4+})	6×202-209, 1×281	15″; I,±M,N
$Pt/PtCe_{39}O_{78}$	0	191	1.67 (Pt^{4+})	6×199-208	8″,15″; D,H,I,N,O,S
$Pt/PtCe_{39}O_{78}$	6	197	1.65 (Pt^{4+})	6×197-210	8″,15″; -B,D,-E,I,-J,O
$Pt/PtCe_{39}O_{78}$	13	204	1.65 (Pt^{4+})	6×201-208	8″,15″; I,±J,±M,N
$Pt/PtCe_{39}O_{77}$	-	148	0.94 (Pt^{2+})	4×199-208, 1×271	8″,9‴,15″; -B,D,H,I,-J,N
$Pt/PtCe_{39}O_{79}$	0	101	1.05 (Pt^{2+})	4×197-200	15″; I,N
$Pt/PtCe_{39}O_{78}$	0	134	1.04 (Pt^{2+})	4×196-198	15″,15‴; D,H,I,N
$Pt/PtCe_{39}O_{78}$	105	240	1.05 (Pt^{2+})	4×196-199	15″,15‴; C,-L,N,T
$Pt/PtCe_{39}O_{77}$	0	257	0.98 (Pt^{2+})	4×197-201	14″,15″,15‴; D,±J,N,-P,T

Table 5.2. Relative energies ΔE and O vacancy formation energies E_{vac} of $Pt/PtCe_{39}O_{80}$ nanoparticle structures. Bader charge *q* and oxidation state of Pt are also given. Pt-O distances are for O atoms in the first coordination sphere. Positions of O_{vac} and Ce^{3+} cations is indicated.

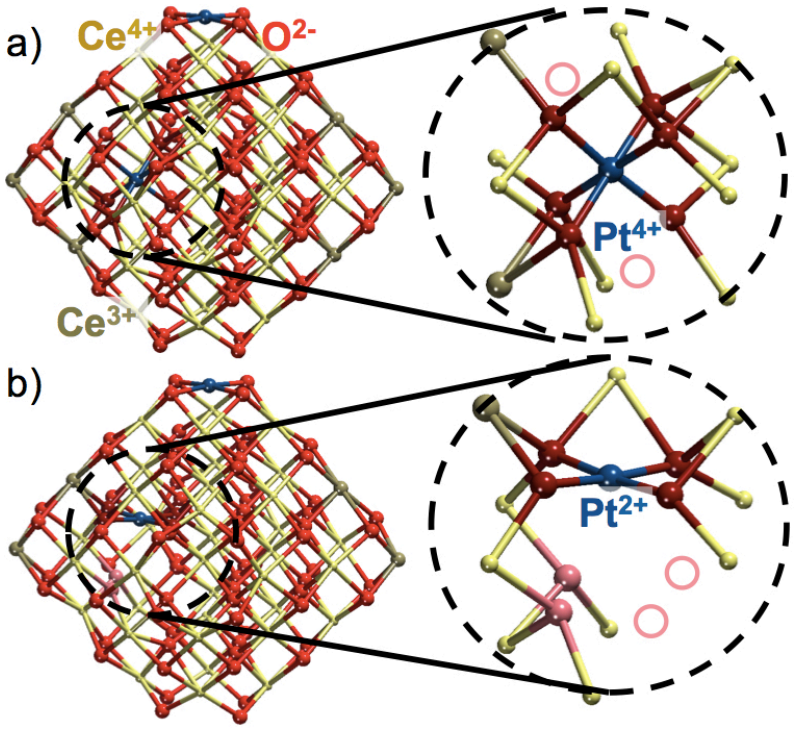

Figure 5.9. Structures of $Pt/PtCe_{39}O_{78}$ nanoparticles resulting from the formation of the second O vacancy near a) Pt^{4+} cation; b) Pt^{2+} cation. Yellow, red and blue spheres represent Ce, O and Pt atoms, respectively. Dark red and pink spheres correspond to the O^{2-} ions closest to and somewhat distant from Pt, respectively. Positions of O_{vac} are indicated by empty circles.

Formation of the third O_{vac} near Pt^{4+} destroys the octahedral coordination of the dopant (Figure 5.10a). Upon removal of the O atom, four of the remaining O atoms rearrange their bonds around Pt to form a square-planar [PtO_4] moiety similar to that discussed above. Pt no longer can keep the high oxidation state +4 and becomes reduced to Pt^{2+}. This process is manifested in the Bader charge value of Pt becoming in this specific coordination 0.94 a.u. Pt is no longer able to maintain the stable local coordination for featuring the +4 state and the electrons left upon removal of the O atom are transferred to the dopant. The reduction to the +2 state requires 148 kJ mol^{-1}. Four short Pt-O distances of 199-208 pm are obtained. Formation of the third O_{vac} near Pt^{2+} (Figure 5.10b) requires 257 kJ mol^{-1}. This high value is a consequence of the reduction of extra Ce^{4+}. The Pt^{2+} center is basically unaltered upon the latter reduction process.

Some conclusions can be drawn from the above-mentioned results. Pt^{4+} species can be formed upon inclusion of small amounts of Pt into the lattice of nanoparticulate ceria. We identified the local coordination of such species in the lattice of ceria, binding 6 O atoms in an octahedral fashion and leaving two more distant O atoms less coordinated. Unlike Pt-ceria bulk systems, maintaining the +4 state of Pt in NPs is plausible, up to formation of two O_{vac}. This enhanced stability Pt^{4+} is related to the presence of surface Ce cations. These cations are less coordinated than the Ce^{4+} cations in inner bulk-like positions. Thus, accommodation of electrons left upon removal of O atoms is easier on such surface Ce^{4+} cations. Thermodynamically driven evolution of Pt^{4+} to Pt^{2+} upon formation of two O vacancies indicates that Pt^{4+} and Pt^{2+} species can coexist in the material. Formation of the third O_{vac} completely destroys the octahedral coordination of 6 O atoms around Pt, making it unable to stay the +4 state. To summarize, nanostructuring of ceria triggers stabilization of Pt in the high oxidation state of +4 that can be maintained upon formation of up to two O vacancies.

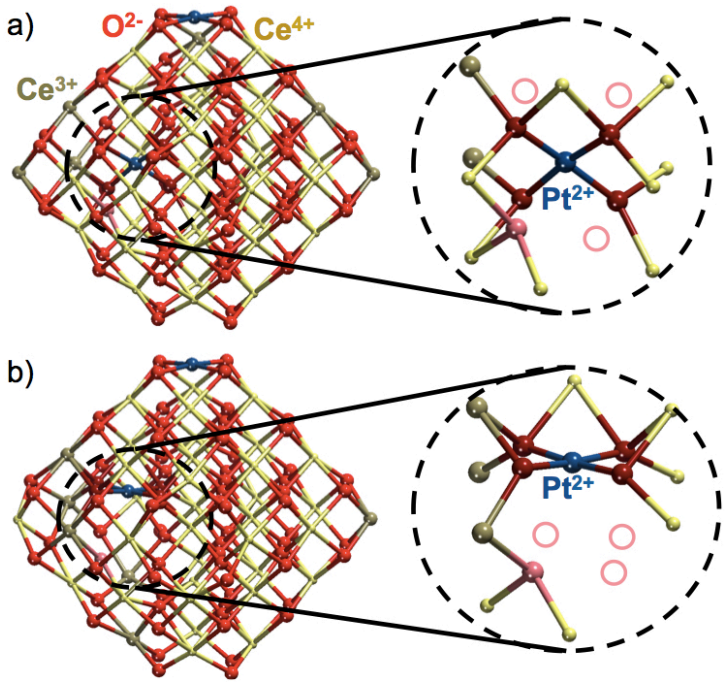

Figure 5.10. Structures of $Pt/PtCe_{39}O_{77}$ nanoparticles resulting from the formation of the third O vacancy near a) Pt^{4+} cation; b) Pt^{2+} cation. Yellow, red and blue spheres represent Ce, O and Pt atoms, respectively. Dark red and pink spheres correspond to the O^{2-} ions closest to and somewhat distant from Pt, respectively. Positions of O_{vac} are indicated by empty circles.

Four Pt atoms at the surface of doped nanoparticulate ceria

In the following we address how Pt coverage affects OSC of Pt-doped ceria NPs. To do so, we considered adsorption of four Pt atoms on different {100} nanofacets of the Pt-doped ceria NP. Ce^{4+} located inside ceria NP binds to 8 O^{2-} with Ce-O distances of 229-236 pm. These Ce-O distances are close to the distances when only one Pt atom is adsorbed on the ceria NP, as discussed above. Adsorption on the nanofacets of four Pt atoms becoming Pt^{2+} generates 8 Ce^{3+} centers. Again, the [6+2] arrangement of O atoms near the inner Pt dopant is obtained upon geometry optimization without any need of structure distortion at the dopant (Figure 5.11). Pt features the +4 state and Bader charge of 1.63 a.u. The coordination of Pt^{4+} is characterized by 6 short Pt-O distances of 207-210 pm (octahedral shell) and two long distances of 282 pm and 296 pm.

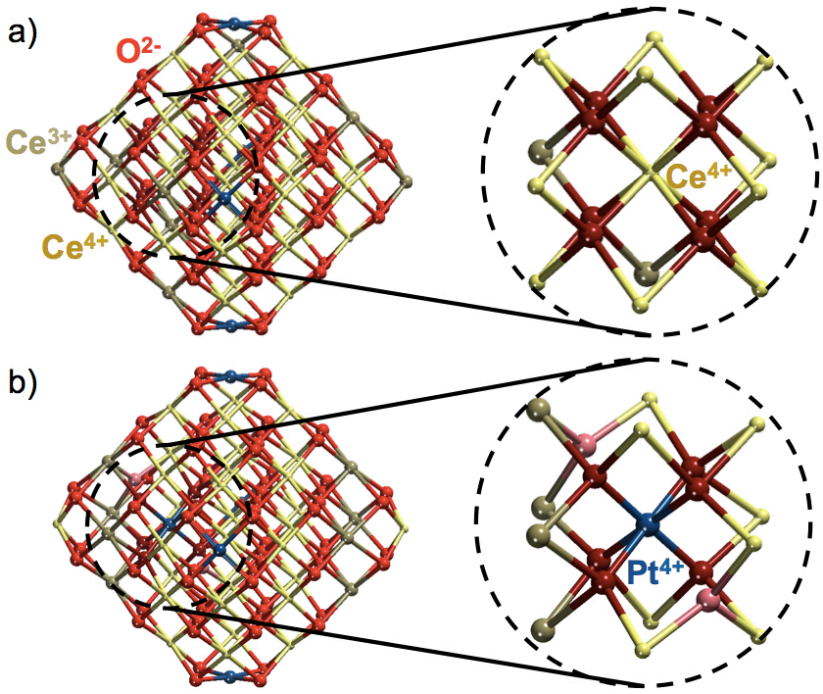

Figure 5.11. Stoichiometric models a) $Pt_4/Ce_{40}O_{80}$ and b) $Pt_4/PtCe_{39}O_{80}$. Yellow, red and blue spheres represent Ce, O and Pt atoms respectively. Dark red and pink spheres correspond to O^{2-} ions closest to and somewhat distant from Pt.

System	ΔE, kJ mol^{-1}	E_{vac}, kJ mol^{-1}	*q*, a.u.	M-O, pm	O_{vac} ; Ce^{3+}
$Pt_4/Ce_{40}O_{80}$	-	-	2.36 (Ce^{4+})	8 × 229-236	-; -B, H, I, -J, K, N, -P, T
$Pt_4/Ce_{40}O_{79}$	-	249	2.31 (Ce^{4+})	7 × 221-233	15’’; -B, H, I, -J, K, (K-L), M, N, P, T
$Pt_4/PtCe_{39}O_{80}$	0	-	1.63 (Pt^{4+})	6 × 207-210, 2 × 282-296	- ; D, H, ±J, ±M, O, S
$Pt_4/PtCe_{39}O_{80}$	1	-	1.65 (Pt^{4+})	6 × 206-210, 2 × 284-298	- ; D, H, -J, ±M, O, Q, S
$Pt_4/PtCe_{39}O_{80}$	27	-	1.65 (Pt^{4+})	6 × 205-210, 2 × 280-281	- ; B, D, I, -K, -L, M, N, T
$Pt_4/PtCe_{39}O_{79}$	0	121	1.64 (Pt^{4+})	6 × 205-208, 1 × 289	15’’; -B, H, I, -J, K, -M, N, ±P, T
$Pt_4/PtCe_{39}O_{79}$	74	195	1.62 (Pt^{4+})	6 × 206-209, 1 × 297	15’’; D, H, I, ±J, ±M, N, O, S
$Pt_4/PtCe_{39}O_{79}$	39	160	1.64 (Pt^{4+})	6 × 203-208, 1 × 285	8’’; -B, D, -E, H, I, -J, K, -M, N, T
$Pt_4/PtCe_{39}O_{78}$	0	144	1.64 (Pt^{4+})	6 × 204-208	8’’, 5’’; A, D, H, I, -J, ±K, ±M, P, S, T
$Pt_4/PtCe_{39}O_{78}$	22	166	1.63 (Pt^{4+})	6 × 204-209	8’’, 15’’; -B, D, -E, H, I, -J, K, M, N, P,-R, T
$Pt_4/PtCe_{39}O_{77}$	0	209	0.91 (Pt^{2+})	4 × 204-207, 1 × 271	8’’, 9’’’, 15’’; B, D, -E, H, I, -J, K, M, N, P, -R, T
$Pt_4/PtCe_{39}O_{79}$	0	116	1.03 (Pt^{2+})	4 × 198-201	15’’; D, H, ±J, ±M, O, S

$Pt_4/PtCe_{39}O_{79}$	52	168	1.04 (Pt^{2+})	4 × 198-200	15’’; C, D, F, -L, N, Q, T, V
$Pt_4/PtCe_{39}O_{78}$	0	226	1.02 (Pt^{2+})	4 × 197-201	15’’, 15’’’; C, D, F, J, -L, N, -P, Q’, T, V
$Pt_4/PtCe_{39}O_{77}$	0	219	0.97 (Pt^{2+})	4 × 198-201	14’’, 15’’, 15’’’; C, D, F, ±J, -L, N, O, -P, Q’, T, V

Table 5.3. Relative energies ΔE of and O vacancy formation energies E_{vac} in $Pt_4/Ce_{40}O_{80}$ and $Pt_4/PtCe_{39}O_{80}$ nanoparticles. Bader charge *q* and oxidation state of Pt are also given. Ce-O and Pt-O distances for O atoms located in the first coordination sphere are also given. Positions of O_{vac} and Ce^{3+} cations are denoted.

Formation of the first vacancy near a Ce^{4+} cation (Figure 5.12a) requires 249 kJ mol^{-1}. In turn, release of a more distant O atom around Pt^{4+} only costs 121 kJ mol^{-1} (Figure 5.12b). This is 59 kJ mol^{-1} more than the calculated for the discussed above NP model with one adsorbed Pt atom. The E_{vac} increase can be associated with the higher number of surface Ce^{3+} cations. The most prone to reduction Ce^{4+} cations are already reduced by the electrons of the surficial Pt atoms. Therefore, the noticed E_{vac} increase is caused by destabilizing effects of reducing less easily reducible surface Ce^{4+} cations and of the steric hindrance induced by the resulting Ce^{3+} species. Formation of the first vacancy near the Pt^{4+} dopant in this $Ce_{39}Pt_5O_{80}$ model resulting in Pt^{2+} is characterized by E_{vac} = 116 kJ mol^{-1} (Figure 5.12c).

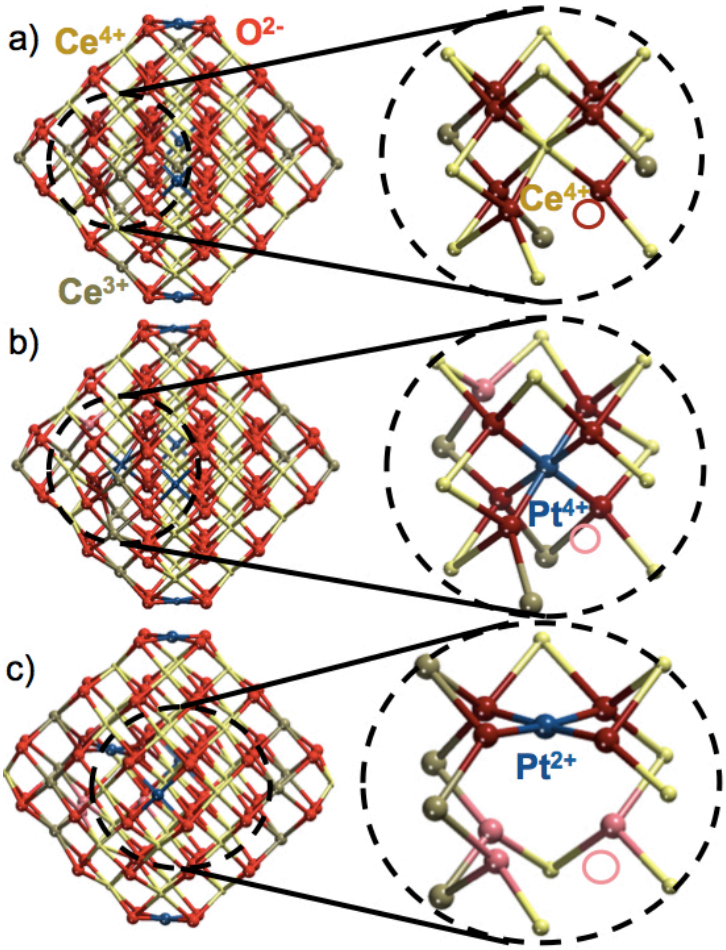

Figure 5.12. Structures of $Pt_4/Ce_{40}O_{79}$ and $Pt_4/PtCe_{39}O_{79}$ nanoparticles obtained after formation of one O vacancy near a) Ce^{4+} cation; b) Pt^{4+} cation; c) Pt^{2+} cation. Yellow, red and blue spheres represent Ce, O and Pt atoms respectively. Dark red and pink spheres correspond to the O^{2-} ions closest to and somewhat distant from Pt, respectively. Position of O_{vac} is indicated by an empty circle.

Formation of the second O_{vac} near Pt^{4+} (Figure 5.13) gives E_{vac} = 144 kJ mol^{-1}. This is 23 kJ mol^{-1} more than the energy required to form the first O_{vac}. The +4 state of Pt is maintained with concomitant formation of two extra Ce^{3+} cations. Bader charge of 1.64 a.u. for Pt and 6 Pt-O distances of 204-208 pm have been calculated. 226 kJ mol^{-1} is needed for removing the second O atom near the square-planar coordinated Pt^{2+} dopant, which noticeably changes neither its Bader charge of 1.02 a.u., nor the four Pt-O distances of 197-201 pm. Unlike the case with just one adsorbed Pt atom, the present model with four adsorbed Pt atoms shows notable thermodynamic preference to maintain inner Pt-dopant in the +4 state upon formation of the second O vacancy.

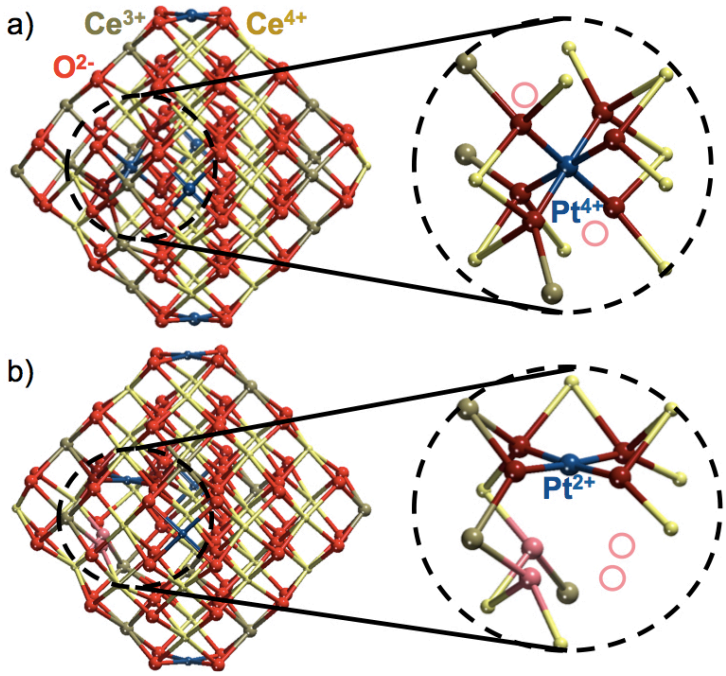

Figure 5.13. Structures of $Pt_4/PtCe_{39}O_{78}$ nanoparticles obtained after formation of the second O vacancy near a) Pt^{4+} cation; c) Pt^{2+} cation. Yellow, red and blue spheres represent Ce, O and Pt atoms respectively. Dark red and pink spheres correspond to the O^{2-} ions closest to and somewhat distant from Pt, respectively. Positions of O_{vac} are indicated by empty circles.

Again, formation of the third O vacancy near Pt^{4+} (with E_{vac} = 209 kJ mol^{-1}) is required for reducing it to Pt^{2+} (Figure 5.14a). Removal of the O atom induces the square-planar coordination of Pt^{2+} to four surrounding it O atoms. For Pt^{2+} in this

coordination Bader charge of 0.91 a.u. and four Pt-O distances of 204-207 pm are calculated. Notably, formation of the third O_{vac} near Pt^{2+} dopant (E_{vac} = 219 kJ mol^{-1}) is even a little more energy demanding than near the Pt^{4+} dopant.

As a general trend, increasing Pt coverage on the surface of ceria NP slightly decreases the OSC. This is reflected in somewhat higher E_{vac} values obtained for the present models compared with those, when only one Pt atom is adsorbed at the {100} nanofacet. At higher surface coverage by Pt, fewer Ce^{4+} cations remain available for reduction. Therefore, electrostatic and steric impediments make formation of O vacancies more energetically costly.

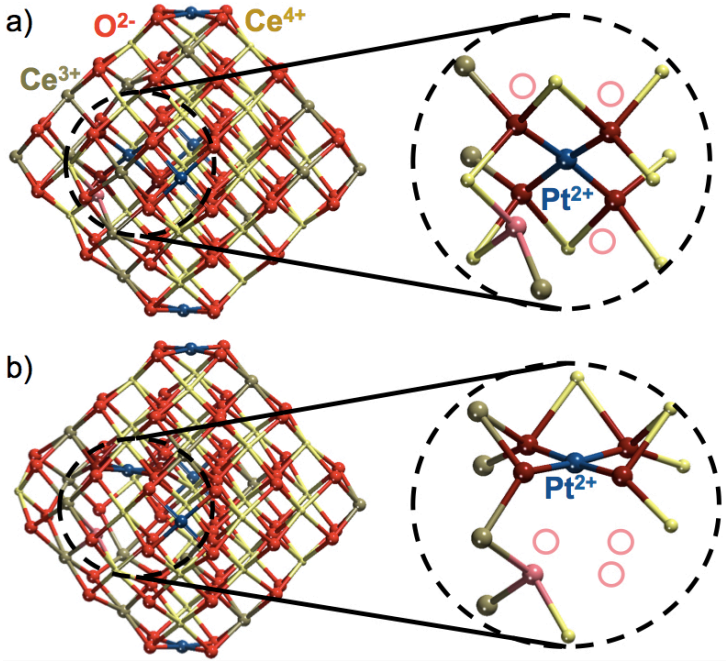

Figure 5.14. Structures of $Pt_4/PtCe_{39}O_{77}$ nanoparticles obtained after formation of the third O vacancy near a) Pt^{4+} cation; b) Pt^{2+} cation. Yellow, red and blue spheres represent Ce, O and Pt atoms respectively. Dark red and pink spheres correspond to the O^{2-} ions closest to and somewhat distant from Pt, respectively. Positions of O_{vac} are indicated by empty circles.

No Pt atoms at the surface of doped nanoparticulate ceria:

Finally, we consider results for Pt-doped ceria NP with no Pt atoms adsorbed on the surface (Table 5.4). Ce^{4+} located inside the pristine $Ce_{40}O_{80}$ NP binds 8 O^{2-} at Ce-O distances of 229-236 pm. The [6+2] arrangement of O anions around Pt^{4+} in this cationic position results from geometry optimization without any need of introducing extra distortion of the surrounding of the noble metal dopant (Figure 5.15), like for the other Pt-doped NP systems considered above. Pt^{4+} is found to feature Bader charge of 1.66 a.u. and octahedral coordination with six Pt-O distances of 204-209 pm and two more remote O atoms with the distances of 281 pm and 266 pm.

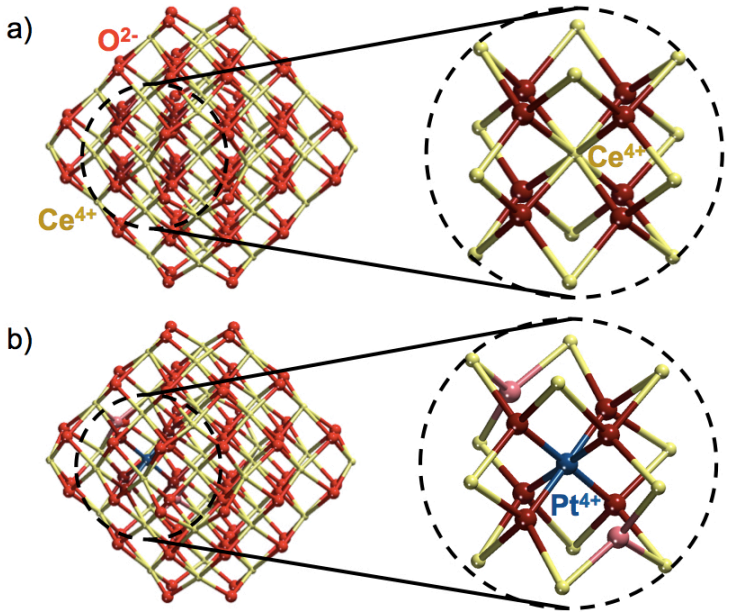

Figure 5.15. Overview of pristine a) $Ce_{40}O_{80}$ and b) $PtCe_{39}O_{80}$. Yellow, red and blue spheres represent Ce, O and Pt atoms respectively. Dark red and pink spheres correspond to O^{2-} ions closest to and somewhat distant from Pt.. Oxidation states of Ce and Pt are also denoted.

Formation of the first O vacancy near an inner Ce^{4+} cation (Figure 5.16a) requires 171 kJ mol^{-1}. In turn, release of one of the farther O atoms near Pt^{4+} (Figure 5.16b) needs only 32 kJ mol^{-1}. This dramatic decrease in the E_{vac} value compared to those obtained with Pt atoms adsorbed on the surface of the NP is related with the particularly easy reduction of two corner Ce^{4+} cations, which in the presence of the Pt adsorbates

have been already reduced to Ce^{3+}. These two Ce atoms are least coordinated among all other Ce atoms in the NP. Therefore, their reduction is strongly driven energetically. Bader charge of 1.66 a.u. and 6 short Pt-O distances of 203-209 pm and a longer distance of 281 pm are calculated for the Pt^{4+} dopant. Formation of the first O vacancy near the dopant becoming Pt^{2+} (Figure 5.14c) is characterized by E_{vac} = 107 kJ mol^{-1}, Pt^{2+} Bader charge of 1.07 a.u. and four nearest Pt-O distances of 197-199 pm.

System	ΔE, kJ mol^{-1}	E_{vac}, kJ mol^{-1}	*q*, a.u.	M-O, pm	O_{vac} ; Ce^{3+}
$Ce_{40}O_{80}$	-	-	2.34 (Ce^{4+})	8 × 229-236	-; -
$Ce_{40}O_{79}$	-	171	2.31 (Ce^{4+})	7 × 222-233	15’’; I, N
$PtCe_{39}O_{80}$	0	-	1.66 (Pt^{4+})	6 × 204-209, 2 × 281-286	-; -
$PtCe_{39}O_{80}$	112	-	1.53 (Pt^{4+})	4 × 207-212, 4 × 232-250	-; -
$PtCe_{39}O_{79}$	0	32	1.66 (Pt^{4+})	6 × 203-209, 1 × 281	15’’; I, N
$PtCe_{39}O_{78}$	0	141	1.66 (Pt^{4+})	6 × 202-209	8’’, 15’’; D, I, -J, N
$PtCe_{39}O_{77}$	0	174	0.94 (Pt^{2+})	4 × 201-207, 1 × 269	8’’, 9’’’, 15’’; D, I, -J, N
$PtCe_{39}O_{79}$	0	107	1.07 (Pt^{2+})	4 × 197-199	15’’; -
$PtCe_{39}O_{78}$	0	132	1.05 (Pt^{2+})	4 × 196-198	15’’, 15’’’; N, -P
$PtCe_{39}O_{77}$	0	225	1.01 (Pt^{2+})	4 × 196-200	14’’, 15’’, 15’’’; -J, -M, O, -P

Table 5.4. Relative energies ΔE and O vacancy formation energies E_{vac} of $Ce_{39}PtO_{80}$ nanoparticle structures. Bader charge *q* and oxidation state of Pt are also given. Ce-O and Pt-O distances considering O atoms located in the first coordination sphere are also given. Locations of O_{vac} and Ce^{3+} cations are denoted.

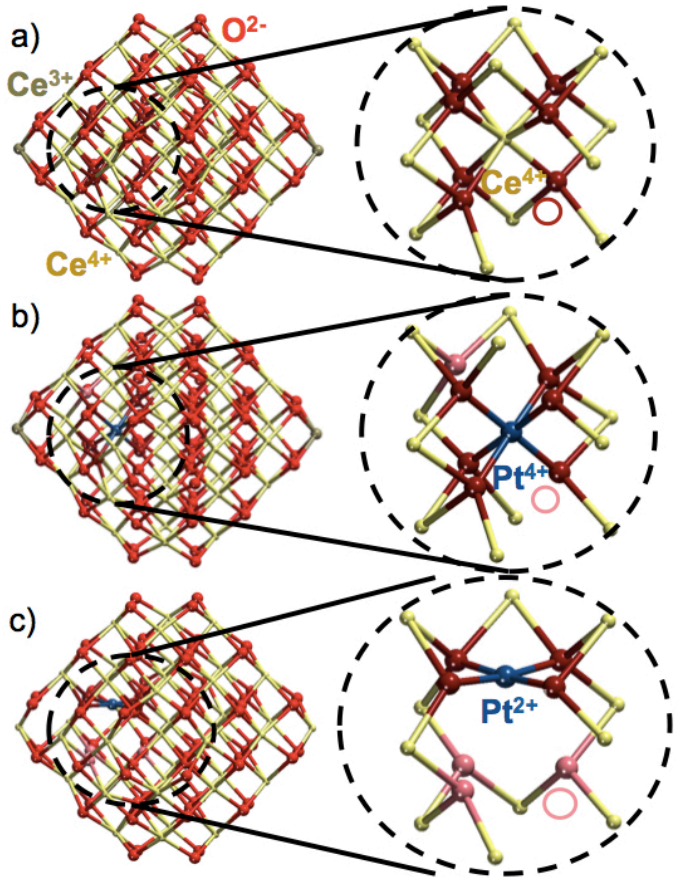

Figure 5.16. Structures after formation of an O vacancy in the $Ce_{40}O_{79}$ nanoparticle nearby a) Ce^{4+} cation; b) Pt^{4+} cation; c) Pt^{2+} cation. Yellow, red and blue spheres represent Ce, O and Pt atoms respectively. Dark red and pink spheres correspond to the O^{2-} ions closest to and somewhat distant from Pt, respectively. Location of O_{vac} is indicated by an empty circle.

Formation of the second O_{vac} near Pt^{4+} maintained in this oxidation state (Figure 5.17a) requires E_{vac} = 141 kJ mol^{-1}, which is 109 kJ mol^{-1} more than that for creating the first O_{vac}. The resulting structure with two O_{vac} is characterized by the Pt Bader charge of 1.66 a.u. and 6 Pt-O distances of 202-209 pm. Removal of the second O atom from the second coordination sphere of the square-planar coordinated Pt^{2+} is associated with its Bader charge of 1.05 a.u., four Pt-O distances of 196-198 pm and the energy cost of 132 kJ mol^{-1}. This value is only insignificantly lower than that calculated for the O vacancy creation near Pt^{4+}. Therefore, the energetic considerations indicate that the +4 state of the Pt dopant in the present case can survive even creation of the second O vacancy near the dopant.

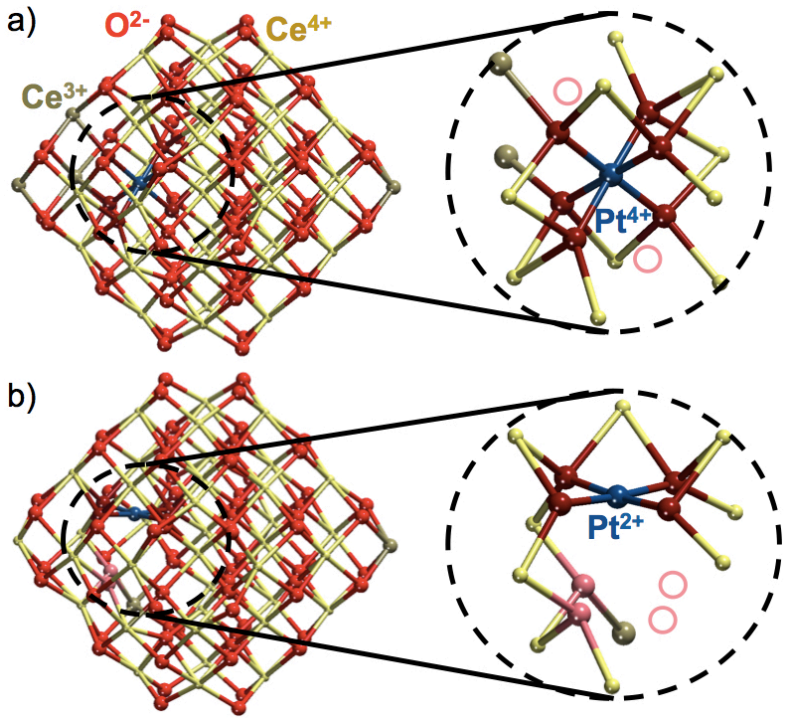

Figure 5.17. Structures after formation of a second O vacancy in the $PtCe_{39}O_{78}$ nanoparticle nearby a) Pt^{4+} cation; b) Pt^{2+} cation. Yellow, red and blue spheres represent Ce, O and Pt atoms respectively. Dark red and pink spheres correspond to the O^{2-} ions closest to and somewhat distant from Pt, respectively. Locations of O_{vac} are indicated by empty circles.

Finally, creation of the third O_{vac} near Pt^{4+} reduces the latter to Pt^{2+} (Figure 5.18a). Removal of the O atom from the configuration featuring Pt^{4+} requires 174 kJ mol^{-1}, furnishes the typical square-planar coordination of Pt^{2+} with four nearest O atoms at 201-207 pm and the Pt^{2+} Bader charge of 0.94 a.u. Notably, creation of the third O_{vac} near Pt^{2+} is more energetically demanding and requires 225 kJ mol^{-1}.

The results presented above strengthen the hypothesis that, not unexpectedly, the degree of reduction of ceria samples (i.e., the number of Ce^{3+} cations in the NPs under scrutiny) is one of the key factors governing the increase or decrease of the OSC capacity of ceria, also in the presence of such atomic dopants as Pt.

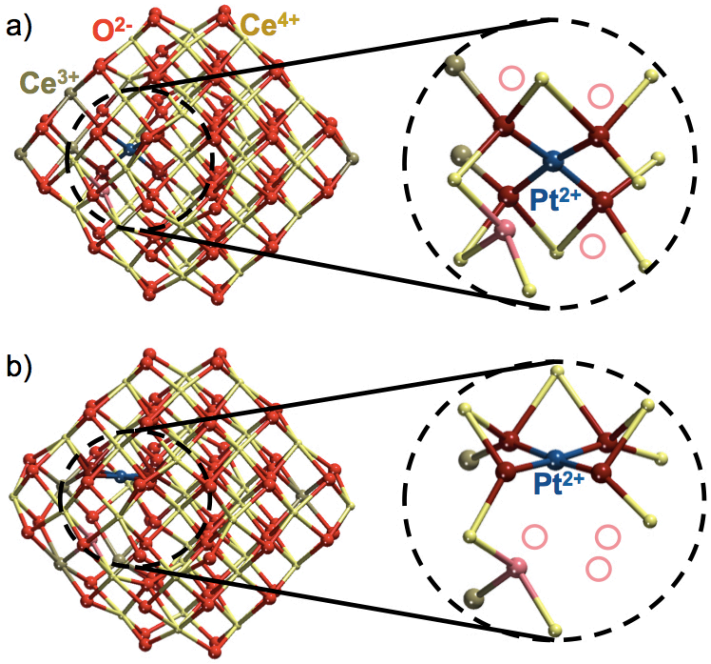

Figure 5.18. Structures after formation of a third O vacancy in the $PtCe_{39}O_{77}$ nanoparticle nearby the previous a) Pt^{4+} cation; b) Pt^{2+} cation. Yellow, red and blue spheres represent Ce, O and Pt atoms respectively. Dark red and pink spheres correspond to the O^{2-} ions closest to and somewhat distant from Pt, respectively. Locations of O_{vac} are indicated by empty circles.

5.4. Overview

In the present chapter we considered the effects of both doping of ceria with the noble metal Pt and its nanostructuring on the OSC. Results obtained for bulk ceria revealed that Pt can feature +4 oxidation state only in an octahedral coordination, binding 6 O atoms and leaving two more distant O atoms less-coordinated. In the case of one O vacancy, Pt^{4+} notably prefers to be reduced to Pt^{2+} and to modify the coordination environment through strong lattice distortion. Pt moves out of the lattice position of Ce to adopt the +2 state and the square-planar coordination, binding four nearest O atoms and leaving the other three O atoms in the second coordination sphere.

Nanostructuring of Pt-doped ceria causes several effects on the OSC of the material. Pt^{4+} species in ceria nanoparticles is able to sustain formation of up to two nearby O vacancies. For all studied NP models calculated E_{vac} values are lower than those for the bulk models. Formation of the third O vacancy destroys the inherent octahedral coordination of Pt^{4+} cation, reduces the latter to the +2 state and creates a typical square-planar coordination with nearby four O^{2-} anions. Thus, the nanostructuring leads to enhancement of the OSC of Pt-doped ceria. The origin of such improved OSC is related to the presence of surface Ce atoms. Low-coordinated surface Ce^{4+} cations are more easily reducible than bulk Ce^{4+} ones and accept electrons left upon oxygen release quite facile. Furthermore, more voluminous Ce^{3+} cations can be better structurally accommodated as low-coordinated surface atoms.

Regarding the calculated data for different Pt loadings, E_{vac} values generally increase with increasing Pt coverage. For instance, higher Pt coverage results in a higher number of surface Ce^{3+} cations. Thus, there is a direct relation between the higher E_{vac} values and the number of Ce^{3+} cations.

These results deepen the atomic-level understanding about how doping processes affect the OSC of ceria. Nanostructuring of ceria appears to play a key role in the enhancement of OSC. By means of the nanostructuring, one can tune the propensity of ceria to release and store oxygen. Doping of ceria by noble metals such as Pt is an efficient approach to further increase the OSC. At variance with the published up to now calculated data, we found Pt^{4+} species to play an

important role in the oxygen storage processes, modifying the local coordination of the substituted Ce^{4+} cations to a [6+2] octahedral configuration. These two more distant O atoms located outside the first coordination sphere of the Pt^{4+} dopant are prone to be easily released and are expected to be able to participate in various oxidation reactions already at quite low temperatures.

References

(1) Trovarelli, A. Structural and Oxygen Storage/Release Properties of CeO_2-Based Solid Solutions. *Comments Inorg. Chem.* **1999**, *20*, 263–284.

(2) Kašpar, J.; Fornasiero, P.; Graziani, M. Use of CeO_2-Based Oxides in the Three-Way Catalysis. *Catal. Today* **1999**, *50*, 285.

(3) Gandhi, H. S.; Graham, G. W.; McCabe, R. W. Automotive Exhaust Catalysis. *J. Catal.* **2003**, *216*, 433–442.

(4) Gulyaev, R. V.; Stadnichenko, A. I.; Slavinskaya, E. M.; Ivanova, A. S.; Koscheev, S. V.; Boronin, A. I. In Situ Preparation and Investigation of Pd/CeO_2 Catalysts for the Low-Temperature Oxidation of CO. *Appl. Catal. A Gen.* **2012**, *439–440*, 41–50.

(5) Fu, Q.; Weber, A.; Flytzani-Stephanopoulos, M. Nanostructured $Au-CeO_2$ Catalysts for Low-Temperature Water-Gas Shift. *Catal. Letters* **2001**, *77*, 87–95.

(6) Cargnello, M.; Montini, T.; Polizzi, S.; Wieder, N. L.; Gorte, R. J.; Graziani, M.; Fornasiero, P. Novel Embedded $Pd@CeO_2$ Catalysts: A Way to Active and Stable Catalysts. *Dalton Trans.* **2010**, *39*, 2122–2127.

(7) Luo, J. Y.; Meng, M.; Yao, J. S.; Li, X. G.; Zha, Y. Q.; Wang, X.; Zhang, T. Y. One-Step Synthesis of Nanostructured Pd-Doped Mixed Oxides MO_x-CeO_2 (M = Mn, Fe, Co, Ni, Cu) for Efficient CO and C_3H_8 Total Oxidation. *Appl. Catal. B Environ.* **2009**, *87*, 92–103.

(8) Mai, H. X.; Sun, L. D.; Zhang, Y. W.; Si, R.; Feng, W.; Zhang, H. P.; Liu, H. C.; Yan, C. H. Shape-Selective Synthesis and Oxygen Storage Behavior of Ceria Nanopolyhedra, Nanorods, and Nanocubes. *J. Phys. Chem. B* **2005**, *109*, 24380–24385.

(9) Gorte, R. J. Ceria in Catalysis: From Automotive Applications to the Water-Gas Shift Reaction. *AlChE J.* **2010**, *56*, 1126–1135.

(10) Sugiura, M. Oxygen Storage Materials for Automotive Catalysts: Ceria-Zirconia Solid Solutions. *Catal. Surv. from Asia* **2003**, *7*, 77–87.

(11) Hori, C. E.; Permana, H.; Ng, K. Y. S.; Brenner, A.; More, K.; Rahmoeller, K. M.; Belton, D. Thermal Stability of Oxygen Storage Properties in a Mixed CeO_2-ZrO_2 System. *Appl. Catal. B-Environmental* **1998**, *16*, 105–117.

(12) Murota, T.; Hasegawa, T.; Aozasa, S.; Matsui, H.; Motoyama, M. Production Method of Cerium Oxide with High Storage Capacity of Oxygen and Its Mechanism. *J. Alloys Compd.* **1993**, *193*, 298–299.

(13) Fornasiero, P.; Dimonte, R.; Rao, G. R.; Kaspar, J.; Meriani, S.; Trovarelli, A.; Graziani, M. Rh-Loaded CeO_2-ZrO_2 Solid-Solutions as Highly Efficient Oxygen Exchangers: Dependence of the Reduction Behavior and the Oxygen Storage Capacity on the Structural-Properties. *J. Catal.* **1995**, *151*, 168–177.

(14) Ozawa, M.; Kimura, M.; Isogai, A. The Application of Ce-Zr Oxide Solid Solution to Oxygen Storage Promoters in Automotive Catalysts. *J. Alloys Compd.* **1993**, *193*, 73–75.

(15) Mamontov, E.; Egami, T.; Pennsyl, V.; Brezny, R.; Koranne, M.; Grace, W. R.; Grace, C.; Da, V.; Tyagi, S. Lattice Defects and Oxygen Storage Capacity of Nanocrystalline Ceria and Ceria-Zirconia. *J. Phys. Chem. B* **2000**, *104*, 11110–

11116.

(16) Yang, Z.; Luo, G.; Lu, Z.; Hermansson, K. Oxygen Vacancy Formation Energy in Pd-Doped Ceria: A DFT+U Study. *J. Chem. Phys.* **2007**, *127*, 74704.

(17) Yang, Z.; Luo, G.; Lu, Z.; Woo, T. K.; Hermansson, K. Structural and Electronic Properties of NM-Doped Ceria (NM = Pt, Rh): A First-Principles Study. *J. Phys. Condens. Matter* **2008**, *20*.

(18) Yang, Z. X.; Ma, D. W.; Yu, X. H.; Hermansson, K. The Main Factors Influencing the O Vacancy Formation on the Ir Doped Ceria Surface: A DFT+U Study. *Eur. Phys. J. B* **2010**, *77*, 373–380.

(19) Scanlon, D. O.; Morgan, B. J.; Watson, G. W. The Origin of the Enhanced Oxygen Storage Capacity of $Ce_{(1-x)}(Pd/Pt)_{(x)}O_2$. *Phys. Chem. Chem. Phys.* **2011**, *13*, 4279–4284.

(20) Kehoe, A. B.; Scanlon, D. O.; Watson, G. W. Role of Lattice Distortions in the Oxygen Storage Capacity of Divalently Doped CeO_2. *Chem. Mater.* **2011**, *23*, 4464–4468.

(21) Loschen, C.; Carrasco, J.; Neyman, K. M.; Illas, F. First-Principles LDA+U and GGA+U Study of Cerium Oxides: Dependence on the Effective U Parameter. *Phys. Rev. B* **2007**, *75*, 35115.

CHAPTER SIX

Destabilization of cationic surficial Pt^{2+} species to metallic Pt^{0}

6.1. Introduction

In Chapter 3, we addressed the propensity of a series of transition metal atoms to be stabilized in specific surface sites of nanostructured ceria.[1] As a reminder, {100} nanofacets of ceria are found to be able to accommodate various transition metal atoms in the form of cationic species. The ceria NP plays for the anchored metal atoms a role analogous to that of a polydentate ligand. Adsorption on these sites results in oxidation of the metal atoms with the concomitant reduction of Ce^{4+} cations to Ce^{3+}.

Atomic dispersion of precious metals is a promising way for designing cost-efficient materials. As mentioned in previous chapters of the Thesis, SACs are the extreme way of maximizing the efficiency of metal content. Cationic metal species dispersed at the surface of the support are readily available for reactants. One of important applications of SACs materials is their usage in proton exchange membrane fuel cells.[2,3] In particular, presence of such atomically dispersed metal species was proposed to control the observed high specific power and thermal stability of Pt-CeO_2 anode catalysts. There, Pt^{2+} species are found to be anchored at {100} nanofacets of ceria in square-planar coordination,[3,4] binding four surficial O^{2-} anions. In order to uncover the specific role of the Pt^{2+} species, reactivity studies of Pt-CeO_2 films towards molecular hydrogen dissociation were performed.[4-6] Surprisingly, it was found that Pt^{2+} species are unable to catalyze dissociation of hydrogen, but traces of metallic Pt are needed to trigger the process.[6] Even if cationic Pt^{2+} species are not confirmed to serve as the active site for that specific reaction, they are stable enough to survive several cycles of fuel cell tests, revealing strongly suppressed formation of metallic Pt particles.[4] In turn, reduction of Pt^{2+} species to ultra-small Pt clusters was observed under electrochemical conditions.[7] These results point to a dynamic structural transformation of Pt-CeO_2 catalysts under alternating reducing/oxidizing conditions.

In the present chapter, we examine possible factors involved in the reduction of Pt^{2+} species, which may generate small Pt particles catalytically active in a number of chemical reactions. Various reduction processes, which may destabilize these highly stable metal cations, have been taken into account. As was discussed in Chapter 4, formation of O_{vac} results in reduction of either the adsorbed noble metal or Ce^{4+} cations of the ceria NP. Formation of several oxygen vacancies may induce significant

destabilization of the adsorbed noble metal species. Furthermore, we take into account the effect of metal loading on the reducibility of the ceria NPs. Finally, the third process has also been studied, which is adsorption of Sn atoms near cationic Pt species. The presented results provide insights in the possible causes of the reduction of cationic metal species and open a controllable route to prepare sub-nanometer metal particles on ceria supports, which can be used, among other technological applications, for dissociation of hydrogen on Pt-CeO_2 based fuel cell anode catalysts.

6.2. Models

General description of the models used for representing ceria NPs can be found in Chapter 3.

Adsorption energies $E_{ad}(M)$ of Sn and Pt atoms on ceria NP have been calculated as $E_{ad}(M) = E(M_1\text{-}Pt_xSn_yCe_{40}O_{80}) - E(M_1) - E(Pt_xSn_yCe_{40}O_{80})$, where $E(M_1)$ is the total ground-state energy of an isolated metal atom M_1 = Sn or Pt, $E(M_1\text{-}Pt_xSn_yCe_{40}O_{80})$ and $E(Pt_xSn_yCe_{40}O_{80})$ are total energies of the ceria NPs containing x Pt atoms ($x \leq 1$) and y Sn atoms ($y \leq 3$) with and without M_1, respectively.

6.3. Results and discussion

In the following, effects of various reduction processes on the stability of surficial Pt^{2+} species are discussed. The model NP with labeled positions of O vacancies and Ce^{4+} cations is shown in Figure 6.1. As we have seen in Chapter 3, adsorption of Pt atom on the {100} nanofacet of ceria NP is strongly favored, E_{ad} = -7.02 eV. Upon adsorption of the metal atom reduction of two Ce^{4+} cations in corner positions takes place with the concomitant oxidation of the noble metal to the +2 state.

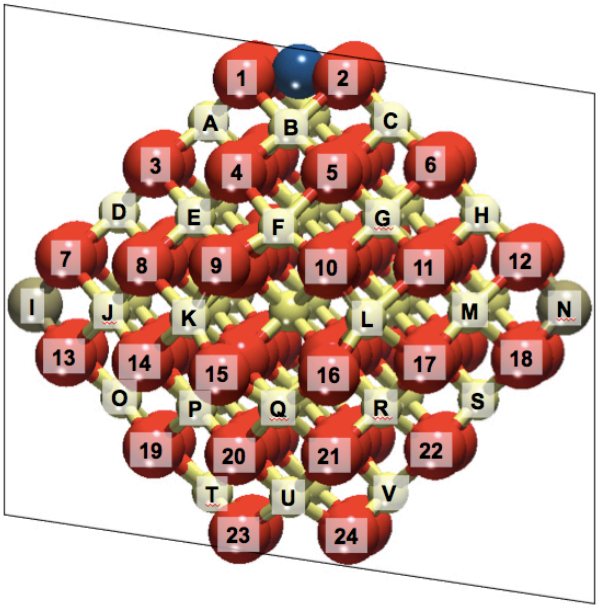

Figure 6.1. Sketch of the $Ce_{40}O_{80}$ model with Pt atom adsorbed on a {100} nanofacet. Yellow, brown, blue and red spheres correspond to Ce^{4+}, Ce^{3+}, Pt^{n+} and O^{2-} species, respectively. The transparent plane divides the nanoparticle in two symmetric halves. Numbers label conceivable positions of O vacancies and letters specify locations of the concomitantly formed Ce^{3+} cations.

As a quite approximate criterion for resistance of the adsorbed Pt^{2+} moiety against aggregation in metallic particle, we can use difference of the adsorption energy and of the bulk cohesive energy of Pt, which is equal to -5.85 eV.[8] According to such estimate the aggregation of Pt^{2+} adsorbed on a {100} facet of unreduced ceria is disfavoured by 1.17 eV. The formation of a single O_{vac} outside this {100} nanofacet, e.g. in positions 5 or 10 in Figure 6.1, appears to be energetically insufficient to trigger the reduction of the Pt^{2+} cation (Table 6.1). Yet, E_{ad} of atomic Pt in the +2 state falls notably below the

cohesive energy (to -4.5 – -5 eV), for O_{vac} created inside the square formed by four O^{2-} anions of the {100} nanofacet (position 2, Figure 6.1). Such weakening of the adsorption is due to the loss of the square-planar coordination of the Pt^{2+} cation. However, energy required for removing one of these four O atoms (> 2.8 eV) is much higher than that for creating a vacancy outside the {100} nanofacet (1.57 eV in position 10 and 2.24 eV in position 5). This strongly suggests that at least the initial formation of O vacancies should preferentially take place outside the Pt-O_4 moiety.

Pt state	O_{vac} positions	Ce^{3+} positions	E_{ad}, eV	E_{vac}, eV
Pt^{2+}	–	I, N	-7.016	
Pt^{2+}	10	F, I, L, N	-6.242	1.565
Pt^{2+}	5	E, H, I, N	-6.601	2.240
Pt^{2+}	5	E, G, H, I	-6.547	2.294
Pt^{2+}	5	G, I, M, N	-6.315	2.526
Pt^{2+}	5	G, I, J, N	-6.473	2.369
Pt^{2+}	5	G, H, I, N	-6.465	2.376
Pt^{2+}	5	D, G, I, N	-6.593	2.248
Pt^{2+}	5	E, I, M, N	-6.472	2.369
Pt^{2+}	5	A, C, E, N	-6.237	2.605
Pt^{2+}	5	D, E, I, N	-6.476	2.365
Pt^{2+}	5	H, I, J, N	-6.507	2.334
Pt^{2+}	5	D, I, J, N	-6.304	2.537
Pt^{2+}	2	A, C, I, N	-4.993	2.825
Pt^{+}	2	D, H, N	-4.630	3.187
Pt^{+}	2	D, I, N	-4.623	3.194
Pt^{+}	2	D, H, -M	-4.545	3.273

Table 6.1. Adsorption energies E_{ad} of atomic Pt and energies of oxygen vacancy O_{vac} formation E_{vac} in the Pt-$Ce_{40}O_{80}$ model.

In order to account for the effect of Pt loading, we performed calculations using the 4Pt-$Ce_{40}O_{80}$ model (Figure 6.2). There, each of four {100} nanofacets is filled with one Pt^{2+} cation. This results in the reduction of 8 Ce^{4+} cations to the +3 state.

Pt state	O_{vac} positions	Ce^{3+} positions	E_{ad}, eV	E_{vac}, eV
4 Pt^{2+}		-B,H,I,-J,K,N,-P,T	-6.585	
1 Pt^{+}, 3 Pt^{2+}	2	D,G,H,±J,±M,O,S	-6.100 (-4.550*/-6.617**)	2.969
1 Pt^{+}, 3 Pt^{2+}	2	E,I,±K,±M,N,O,S	-5.992 (-4.115*/-6.617**)	3.403
1 Pt^{+}, 3 Pt^{2+}	2	D,H,±J,±M,O,R,S	-6.060 (-4.387*/-6.617**)	3.131
4 Pt^{2+}	5	D,E,G,H,±J,±M,O,S	-6.299	2.175
1 Pt^{0}, 3 Pt^{2+}	±2	A,C,D,H,±J,±M,O,S	-6.137 (-4.778*/-6.589**)	2.326
1 Pt^{+}, 3 Pt^{2+}	±2	C,D,F′,H,±J,±M,O,S	-6.053 (-4.445*/-6.589**)	2.492
1 Pt^{+}, 3 Pt^{2+}	2, -1	D,-E,G,H,±J,±M,O,S	-6.218 (-5.252*/-6.540**)	2.163
1 Pt^{+}, 3 Pt^{2+}	2, -1	D,H,I,±J,±M,N,O,S	-5.997 (-4.368*/-6.540**)	2.606
4 Pt^{2+}	4, 21, -5, -20	±B,-E,-F,G,H,I,-J, K,N,-P,±Q, R,T,U	-5.765	2.965

4 Pt^{2+}	6, 19, -3, -22	-B,C,D,G,H,I,-J,K, N,O,±P, -R,S,T,V	-6.019	2.947
3 Pt^{0}, 1 Pt^{+}	2, 15, -16, -23	-F,G,H,I,J,-M,O,-P,S	-5.340	-3.019
4 Pt^{2+}	±4, ±5, ±20, ±21	±B,C,±E,±F,G,H,I,-J,K,-L,N,±P,±Q,Q′,±R,T,±U	-4.569	3.400
4 Pt^{2+}	±3, ±6, ±19, ±22	A,-B,C,D,E,±G,H,I,±J,K, ±M,N,O,±P,±R,S,T,-U,V	-4.559	3.405

Table 6.2. Energies of Pt adsorption E_{ad} and O_{vac} formation E_{vac} for 4Pt-$Ce_{40}O_{80-n}$ model. The O_{vac} positions with signs "+" and "-" are in front or behind the transparent plane in Figure 6.2, respectively. The sign "±" indicates two symmetric O_{vac} positions, one in front of the plane and another behind it. $^{*}E_{ad}$ for the Pt atom near the O_{vac}. $^{**}E_{ad}$ average for the 3 Pt atoms distant from the O_{vac}. Ce^{3+} ions labelled F′ and Q′ are located between F and -F and between Q and -Q, respectively.

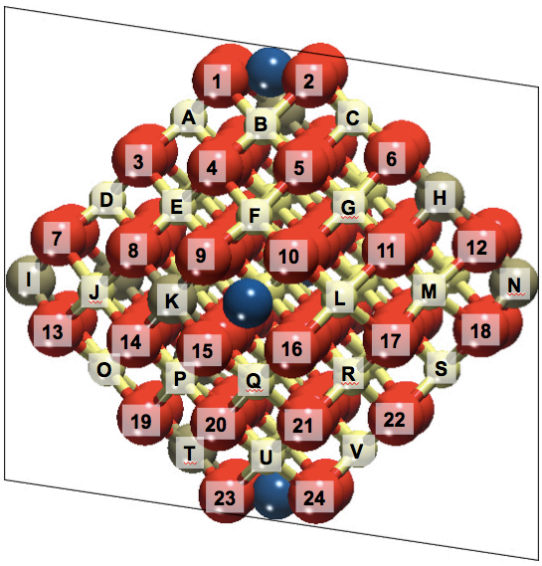

Figure 6.2. Sketch of the $Ce_{40}O_{80}$ model with four Pt atoms adsorbed on four {100} nanofacets. Yellow, brown, blue and red spheres correspond to Ce^{4+}, Ce^{3+}, Pt^{n+} and O^{2-} ions, respectively. The transparent plane divides the nanoparticle in two symmetric halves. Numbers and capital letters label positions of O vacancies and Ce^{3+} cations, respectively.

Average E_{ad} = -6.59 eV per Pt atom in the absence of O vacancies is 0.42 eV lower in magnitude than calculated for the model with a single Pt^{2+} adsorbate. The weakening of adsorption is caused by the presence of a substantial number of reduced Ce^{3+} species. This effect has been already analyzed in Chapter 5. When a single Pt atom is adsorbed on one of the {100} nanofacets, corner Ce^{4+} cations are able to easily uptake two electrons from it. In turn, when Pt atoms are adsorbed on each of four available {100} nanofacet sites, only one of the Pt atoms is able to transfer two of its valence electrons to the corner Ce^{4+} cations. The 6 electrons from the remaining three Pt adsorbates are transferred to other surface Ce^{4+} cations of the NP, with ca. 0.1 eV relative energy loss per Pt atom. Creation of an O_{vac} in position 2 (i.e., removing an O atom from the {100} nanofacet site) results in substantially weaker adsorption of the nearby Pt atom, E_{ad} = -4.55 eV. Notably, the other three Pt atoms are barely affected by the formation of the vacancy in this specific position, with E_{ad} = -6.62 eV. Similarly to the case with only one adsorbed Pt atom, E_{vac} energies obtained are rather high (2.97 – 3.40 eV) compared to that when an O atom is removed outside the Pt-O_4 moiety (e.g., 2.18 eV in position 5). For this external O_{vac} position average E_{ad} values for each Pt atom are -6.30 eV, which is ca. 0.3 eV less in magnitude than obtained without O_{vac}, related with the presence of two extra Ce^{3+} cations. The unlikely removal of two O atoms from the same {100} nanofacet would result in E_{ad} values of the nearby Pt atoms lower than the cohesive energy of Pt (-5.25 eV for positions 2, -1 and -4.78 eV for positions ±2). Importantly, formation of two O vacancies per Pt^{2+} cation even not nearby a Pt atom can take the E_{ad} value well below the cohesive energy. This is the case, for instance, upon creation of eight O vacancies (positions ±4, ±5, ±20, ±21 or ±3, ±6, ±22, ±19). This is an indication that the onset of Pt^{2+} reduction occurs when approximately two oxygen vacancies are created in ceria NPs per Pt^{2+} site.

In collaboration with our experimental partners (group of Prof. Libuda, Uni. Erlangen-Nürnberg), we were able to estimate the ratio between the numbers of O vacancies and Pt^{2+} cations at the onset of Pt^{2+} reduction.[6] Using the temperature-dependent change in the Ce^{3+} concentration one can calculate the concentration of oxygen vacancies produced by oxygen spillover. Taking into account other effects emerging during the growth of Pt^{2+}-CeO_2 films,[3,9] a ratio of 1.5 between the concentrations of oxygen vacancies and Pt^{2+} ions in the temperature region of 450 and 500 K was obtained. This

value is in good agreement with the above mentioned estimate from our density-functional calculations.

#	E_{ad}, kJ mol^{-1}	Sn-O, pm	n
a	-665	2×228, 2×229	2
b	-483	211, 216, 225	2
c	-407	2×209, 251	2
d	-284	196, 199, 201, 203	4
e	286	2×221, 222, 223, 2×257, 2×258	2

Table 6.3. Adsorption energy E_{ad}, Sn-O nearest interatomic distances and oxidation state n for Sn atom located in positions illustrated in panels # of Figure 6.3.

Finally, results regarding the interplay between atomic Pt, Sn and Ce species in different oxidation states are presented. First, we studied the interaction of a single Sn atom with the ceria NP. As can be seen in Figure 6.3, several optimized structures with a Sn atom adsorbed at different sites of $Ce_{40}O_{80}$ NP were calculated in order to determine the most strongly anchoring adsorption site. These studies include the adsorption of Sn at the surface (a-c), as well as its incorporation in sub-surface (d) and in inner (e) interstitial sites of the ceria NP.

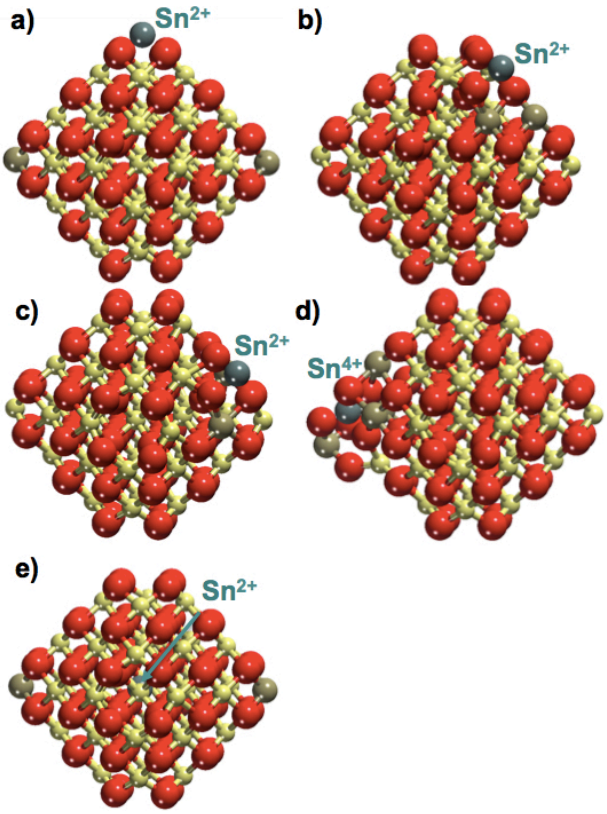

Figure 6.3. Structure of $Ce_{40}O_{80}$ NP with an atom Sn adsorbed at {100} (a), {111} (b), and edge (c) sites on the surface, or located in interstitial sites in the sub-surface (d) and inner (e) regions. Yellow, brown, red and grey spheres represent Ce^{4+}, Ce^{3+}, O^{2-} and Sn species, respectively.

The adsorption of a Sn atom at the surface of $Ce_{40}O_{80}$ NP yields a Sn^{2+} ion accompanied by the reduction of two Ce^{4+} cations to the +3 state. Behaviour of Sn interacting with the {100} nanofacet of ceria is quite similar to the behaviour of other transition metals studied in Chapter 3. Three energetically favorable adsorption configurations associated with the cationic Sn^{2+} at the {100} (a), {111} (b), and edge (c) sites of the ceria NP are calculated, with E_{ad} of -665, -483, and -407 kJ mol^{-1}, respectively (Table 6.3).

In contrast, incorporation of atomic Sn in interstitial sites either sub-surface (Figure 6.3d) or deeper inside (Figure 6.3e) is strongly disfavored with respect to the just discussed surface configurations. In fact, insertion of a Sn atom inside the NP is endothermic by 286 kJ mol^{-1}. Here, Sn^{2+} cation is bound to four O neighbours with Sn-O distances of 221-223 pm, whereas the bonds with the other four O neighbours are longer by 35 pm. According to angle resolved X-ray photoelectron spectroscopy (ARXPS) studies performed by our experimental partners (group of Prof. Libuda), bulk

diffusion of Sn^{2+} ions occurs once all available for Sn surface positions on a Pt-CeO_2 film are occupied.[10] Consequently, the film contains large number of Ce^{3+} species with elongated Ce-O distances. We can speculate that under the just mentioned conditions, when no surface sites are anymore available for Sn, the interstitial sites will become more energetically favorable and possibly able to accommodate Sn atoms.

A moderately favorable configuration of Sn inserted in an interstitial site was found in the sub-surface region of the NP (Figure 6d). This insertion induces strong structural stress, which facilitates further oxidation of Sn to the +4 state with the concomitant reduction of two extra Ce^{4+} cation to +3. Nevertheless, the Sn^{4+} species are expected to be partially reduced in the presence of atomic Sn adsorbed on the ceria NPs.

The optimized structures of Sn interacting with the $Ce_{40}O_{80}$ NP in the presence of Pt^{2+} species are shown in Figure 6.4. Pt^{2+} cations are strongly adsorbed at the {100} sites of ceria NP forming the PtO_4 moiety (Figure 6.4a),[1,3] as already discussed.

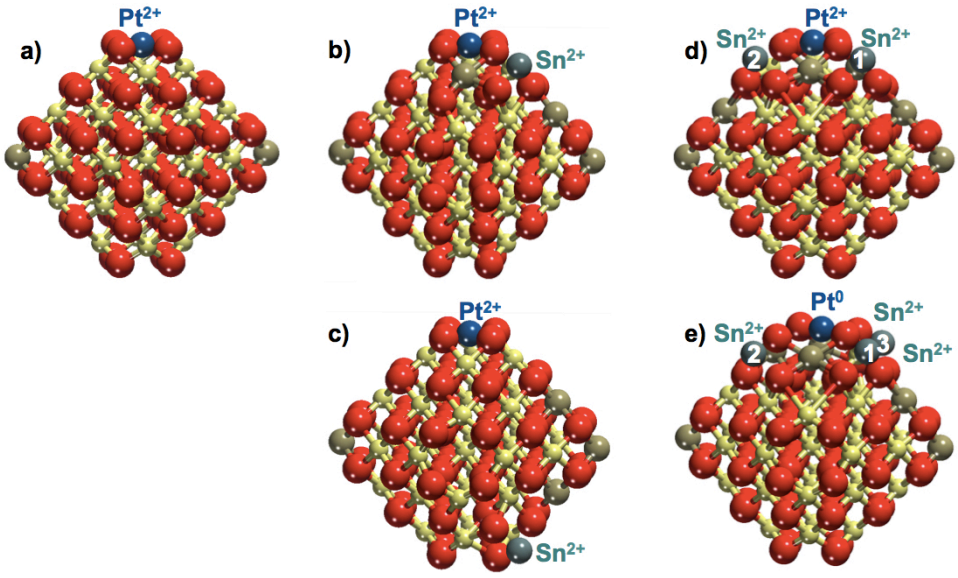

Figure 6.4. Sketches of Pt-$Ce_{40}O_{80}$ NP with different number of adsorbed Sn atoms: (a) no adsorbed Sn, (b-c) one adsorbed Sn atom, (d) two adsorbed Sn atoms and (e) three adsorbed Sn atoms. Yellow, brown, red and grey spheres represent Ce^{4+}, Ce^{3+}, O^{2-} and Sn ions, respectively. Numbers in (d) and (e) label different Sn atoms.

#	E_{ad} Sn, kJ mol^{-1}	E_{ad} Pt, kJ mol^{-1}	Sn^x-O, pm	n Sn	n Pt
a		-678		2	2
b	-406	-597	210, 217, 230	2	2

c	-501	-692	211, 217, 221	2	2
d	-339	-461	1: 213, 214, 235	2	2
			2: 213, 216, 228		
e	-380	-378	1: 214, 218, 222	2	0
			2: 204, 225, 227		
			3: 207, 214, 229		

Table 6.4. Adsorption energy E_{ad} of Sn and Pt atoms, Sn-O nearest distances and oxidation state n of Sn and Pt for Sn locations indicated in panels # of Figure 6.4. x is the label of Sn atom in Figure 6.4 d,e.

In the presence of Pt^{2+} species, we considered adsorption of Sn on the second most stable site, i.e. at {111} facets (Figure 6.3b). In particular, we investigated adsorption of Sn near Pt^{2+} cation (Figure 6.4b) and at the opposite side of the NP (Figure 6.4c).

Adsorption of Sn in the vicinity of Pt^{2+} weakens adsorption of Pt by 81 kJ mol^{-1}, with Pt maintaining the +2 state (Table 6.4). As expected, adsorption of Sn at the opposite side of the NP (Figure 6.4c) barely affects the stability of Pt^{2+}. Adsorption of the second Sn atom in the vicinity of Pt^{2+} notably weakens the adsorption of Pt, E_{ad} = -461 kJ mol^{-1} (Figure 6.4d). If we compare this value with that of atomic Pt^0 at the {100} nanofacet, -328 kJ mol^{-1},[3] we can explain why adsorption of two Sn atoms does not trigger reduction of Pt^{2+} cations to metallic Pt. It is noteworthy that the stability of Pt^{2+} is strongly correlated with the Pt-O bond length within the square-planar arrangement. When two Sn^{2+} cations are adsorbed in the vicinity of a Pt^{2+}, two of the four Pt-O bonds are elongated by ca. 20 pm. Even if this effect weakens the bond, Pt can still maintain the planar coordination. Finally, adsorption of the third Sn atom nearby Pt^{2+} (Figure 6.4e) enables its reduction to Pt^0, yielding E_{ad} = -378 kJ mol^{-1}. Formation of Pt^0 induces rearrangement of the local coordination of O atoms, forming a linear PtO_2 moiety with Pt-O distances of 200 to 217 pm. Note, that the other two O^{2-} anions are strongly displaced from their original positions in the {100} nanofacet, resulting in Pt-O distances of 303-327 pm. Interestingly, the adsorption of the third Sn atom seems to be slightly favored with respect to the average E_{ad} of the first two Sn atoms. This can be associated with the fact that the third Sn atom binds to an O^{2-} anion, which is more weakly bound to Pt and, thus, it can interact more strongly with Sn.

Our density-functional calculations reveal that Pt^{2+} species adsorbed on the {100} nanofacet forming the square-planar PtO_4 moiety are able to sustain adsorption up to three Sn atoms in their vicinity without being reduced. At this point the reduction yields atomic Pt^0 coordinated by two oxygen anions. These results agree with the experimental findings obtained under UHV conditions, which suggest that presence of 6 Ce^{3+} ions or, in other words, at least three Sn atoms per Pt^{2+} species are necessary for triggering reduction of Pt^{2+} to Pt^0.

6.4. Overview

In the current chapter stability of cationic surficial Pt^{2+} species towards several destabilizing reduction effects has been studied. Such effects are i) formation of various O_{vac}, ii) increased Pt loading and iii) adsorption of Sn atoms in the vicinity of the Pt^{2+} species.

Surface O atoms located at {100} nanofacets appear to be the most labile ones and, thus, the most prone to be released by the NP. This feature can be associated with the lower coordination of such O atoms compared with the rest of O atoms. Nevertheless, formation of $[PtO_4]$ moieties at such {100} nanofacets strongly hinders formation of O vacancies there due to the strong interaction of Pt^{2+} with four O^{2-} anions forming its coordination sphere. Formation of an O_{vac} is accompanied by the reduction of two Ce^{4+} cations to Ce^{3+}. Results obtained using the $Ce_{40}O_{80}$ model show that there exists a threshold that needs to be overcome for reduction of Pt^{2+} species to metallic Pt^0. Such threshold is expected to be around the cohesive energy of metallic Pt, -5.85 eV. Thus, reduction of Pt^{2+} species should be favored, when the E_{ad} of Pt falls below the cohesive energy value upon formation of various number of O_{vac}. Analysis of the calculated data reveals that Pt^{2+} species are destabilized, when ca. two O_{vac} are formed in Pt-CeO_2 NPs per Pt atom. These results agree with the experimental data provided by our collaborating partners. Destabilization of Pt^{2+} species is then associated with the formation of a number of Ce^{3+} cations. The latter are noticeably larger than Ce^{4+} ones and, thus, can substantially modify the structure of the NP. Only after formation of a significant number of Ce^{3+} cations Pt^{2+} species start to be prone to accept electrons left by the removed O atom.

The effect of metal loading on Pt^{2+} species is analogous to the effect caused by formation of O_{vac}. Adsorption of Pt at {100} nanofacets results in oxidation of the metal, with the concomitant formation of two Ce^{3+} cations. There is a threshold, from which Pt^{2+} cations might accept electrons instead of Ce^{4+}.

Finally, adsorption of Sn atoms in the vicinity of Pt^{2+} cations has been analyzed. It appears that the onset of the Pt^{2+} reduction is again determined by the concentration of Ce^{3+} cations in the NP. In this specific case, formation of around 6 Ce^{3+} cations in the

direct vicinity of Pt^{2+} species seems to trigger reduction of Pt^{2+} to Pt^{0}. These results are also in good agreement with the data of our experimental partners. In the presence of Pt^{2+}, Sn is found to be adsorbed as Sn^{2+} at {111} facets of ceria NP. Stability of Pt^{2+} species is strongly dependent on the presence of Sn^{2+} in the direct vicinity.

The results presented in this Chapter provide new insights in the stability of atomically dispersed Pt species on ceria. A deeper understanding of the possible destabilizing effects causing Pt^{2+} reduction to Pt^{0} has been achieved. Despite that materials with atomically dispersed metals are useful for many applications, metal particles are often required as active sites for chemical reactions. Results of this Chapter, combined with experimental developments of our collaborating partners, open a controllable route to prepare sub-nanometer metal particles on ceria supports. Such advanced nanomaterials can be used, among other important applications, to dissociate hydrogen on Pt-CeO_2 based fuel cell anode catalysts.

6.5. References

(1) Figueroba, A.; Kovács, G.; Bruix, A.; Neyman, K. M. Towards Stable Single-Atom Catalysts: Strong Binding of Atomically Dispersed Transition Metals on the Surface of Nanostructured Ceria. *Catal. Sci. Technol.* **2016**, *6*, 6806 – 6813.

(2) Jones, J.; Xiong, H.; DeLaRiva, A. T.; Peterson, E. J.; Pham, H.; Challa, S. R.; Qi, G.; Oh, S.; Wiebenga, M. H.; Pereira Hernández, X. I.; Wang, Y.; Datye, A. K. Thermally Stable Single-Atom Platinum-on-Ceria Catalysts via Atom Trapping. *Science (80-.).* **2016**, *353*, 150–154.

(3) Bruix, A.; Lykhach, Y.; Matolínová, I.; Neitzel, A.; Skála, T.; Tsud, N.; Vorokhta, M.; Stetsovych, V.; Ševčíková, K.; Mysliveček, J.; Fiala, R.; Václavů, M.; Prince, K. C.; Bruyère, S.; Potin, V.; Illas, F.; Matolín, V.; Libuda, J.; Neyman, K. M. Maximum Noble-Metal Efficiency in Catalytic Materials: Atomically Dispersed Surface Platinum. *Angew. Chemie Int. Ed.* **2014**, *53*, 10525–10530.

(4) Fiala, R.; Figueroba, A.; Bruix, A.; Vaclavu, M.; Rednyk, A.; Khalakhan, I.; Vorokhta, M.; Lavkova, J.; Illas, F.; Potin, V.; Matolinova, I.; Neyman, K. M.; Matolin, V. High Efficiency of Pt^{2+}- CeO_2 Novel Thin Film Catalyst as Anode for Proton Exchange Membrane Fuel Cells. *Appl. Catal. B Environ.* **2016**, *197*, 262–270.

(5) Neitzel, A.; Figueroba, A.; Lykhach, Y.; Skála, T.; Vorokhta, M.; Tsud, N.; Mehl, S.; Ševčíková, K.; Prince, K. C.; Neyman, K. M.; Matolín, V.; Libuda, J. Atomically Dispersed Pd, Ni, and Pt Species in Ceria-Based Catalysts: Principal Differences in Stability and Reactivity. *J. Phys. Chem. C* **2016**, *120*, 9852–9862.

(6) Lykhach, Y.; Figueroba, A.; Farnesi Camellone, M.; Neitzel, A.; Skála, T.; Negreiros, F. R.; Vorokhta, M.; Tsud, N.; Prince, K. C.; Fabris, S.; Neyman, K. M.; Matolín, V.; Libuda, J. Reactivity of Atomically Dispersed Pt^{2+} Species towards H_2 : Model Pt−CeO_2 Fuel Cell Catalyst. *Phys. Chem. Chem. Phys.* **2016**.

(7) Brummel, O.; Waidhas, F.; Faisal, F.; Fiala, R.; Vorokhta, M.; Khalakhan, I.; Dubau, M.; Figueroba, A.; Kovacs, G.; Aleksandrov, H. A.; Vayssilov, G. N.; Kozlov, S. M.; Neyman, K. M.; Matolín, V.; Libuda, J. Stabilization of Small Platinum Nanoparticles on Pt-CeO_2 Thin Film Electrocatalysts During Methanol Oxidation. *J. Phys. Chem. C* **2016**, acs.jpcc.6b05962.

(8) Kittel, C. *Introduction to Solid State Physics*; 8th Ed.; J. Wiley: Hoboken, NJ, 2005.

(9) Vayssilov, G. N.; Lykhach, Y.; Migani, A.; Staudt, T.; Petrova, G. P.; Tsud, N.; Skála, T.; Bruix, A.; Illas, F.; Prince, K. C.; Matolín, V.; Neyman, K. M.; Libuda, J. Support Nanostructure Boosts Oxygen Transfer to Catalytically Active Platinum Nanoparticles. *Nat. Mater.* **2011**, *10*, 310–315.

(10) Lykhach, Y.; Figueroba, A.; Skála, T.; Duchoň, T.; Tsud, N.; Aulická, M.; Neitzel, A.; Veltruská, K.; Prince, K. C.; Matolín, V.; Neyman, K. M.; Libuda, J. Redox-Mediated Conversion of Atomically Dispersed Platinum to Sub-Nanometer Particles. *J. Mater. Chem. A* **2017**, doi:10.1039/c7ta02204b.

CHAPTER SEVEN

Using vibrations of CO probe molecules for characterization of Pt-CeO_2 thin films

7.1. Introduction

Characterization of catalytic materials is a crucial step in the development of catalysts. In particular, catalytic performance of metal/metal-oxide composites is controlled by the size, shape, and ordering of the supported metal species. Rates of surface chemical reactions often strongly depend on the form in which the active metal is present, either as nanoparticles, small clusters, or dispersed single atoms. A broad arsenal of experimental tools and approaches is available to characterize catalysts. IR spectroscopy of adsorbed CO as probe molecule is one of the common characterization techniques. In this method the change (shift) of the stretching vibrational frequency of CO molecules upon their adsorption on the surface of the catalytic material is monitored.[1] The C-O frequency shift (along with the intensity variation), very sensitive to details of the interaction between CO molecule and metal particles, enables obtaining crucial information on the oxidation state,[2] structure[3], and size[4,5] of the latter.

Regarding applications in fuel cell technology, anodes based on Pt-CeO_2 thin films with low Pt loading show excellent activity and good stability in proton exchange membrane fuel cells.[6,7] Of key importance is that these kinds of anodes are resistant to CO poisoning.[8] Obviously, it is essential to properly characterize such composites at microscopic level in order to understand atomic details of reaction mechanisms of the underlying catalytic processes and the roles both metal and support play.

C-O frequencies are affected by many factors upon adsorption of a CO molecule on platinum particles. The first is the nature of the adsorption site of the CO molecule. On extended Pt surfaces, for instance, CO is commonly adsorbed linearly on just one Pt atom called on-top site. CO can also be adsorbed between two Pt atoms (bridge site) or over the center of a group formed by three or four Pt atoms (three-fold or four-fold hollow sites, respectively). Another factor significantly influencing the C-O frequency is the oxidation state of and electronic density on Pt atom(s) forming the adsorption site. The bonding between CO molecule and Pt results from the balance of σ- and π-interactions. Surface complexes of CO with cationic Pt^{n+} exhibit almost no back π-bonding, the σ-bonding being the major interaction. This is translated, in terms of C-O bond strength, in an increase of the C-O stretching frequency. In turn, the back π-bonding is the main component in reduced Pt^0 species, inducing a decrease in the C-O

frequency. Therefore, a general trend for C-O stretching frequency is: the lower the oxidation state of the transition metal atoms of the adsorption site, the more red-shifted the CO stretching mode is.[1] Finally, coordination number of the metal atoms of the adsorption site and CO coverage also affect the frequency values modifying the local environment around the CO molecule.

Another factor has to be taken into account when analyzing vibrational frequencies of CO adsorbed on supported Pt particles: the support itself. The presence of the support affects in various ways the Pt particle, not only structurally but electronically, especially when the support plays a non-spectator role. For instance, metallic Pt particles on ceria show strong electronic metal support interactions.[9] As mentioned in the previous chapters, Ce^{4+} cations are able to accept electrons from the metal species and be reduced to the +3 state, producing a charge transfer between Pt particles and the ceria support. The size of the Pt particles is shown to play a major role in determining the transferred charge, which contributes to change the activity and stability of the Pt aggregates.[9]

In the following, we analyze our results obtained using density-functional modeling for the adsorption of a probe CO molecule on a wide range of Pt species and compare them with the pertinent experimental data of our collaboration partners. We theoretically address six bare Pt aggregates of different sizes: Pt_8, Pt_{34}, Pt_{79}, Pt_{116}, Pt_{140}, and Pt_{201}. In order to elucidate the influence of the ceria support on the adsorption properties of CO, we have also modelled Pt_8 and Pt_{34} particles supported on the CeO_2(111) surface. These results deepen the understanding of the structure of the Pt/CeO_2 based thin film electrocatalysts used for oxidation of methanol.[10]

7.2. Models

We performed a systematic density functional study of bonding, structural and vibrational properties of CO molecule adsorbed on Pt particles of different size. We investigated adsorption of CO at all types of on-top sites of bare Pt_8, Pt_{34}, Pt_{79}, Pt_{116}, Pt_{140}, and Pt_{201} particles. To address how the presence of a reducible metal-oxide support modifies the adsorption properties of CO we also calculated CO adsorbed at all kinds of on-top sites of supported $Pt_8/CeO_2(111)$ and $Pt_{34}/CeO_2(111)$. Optimized structures of all considered models of Pt particles are sketched in Figure 7.1.

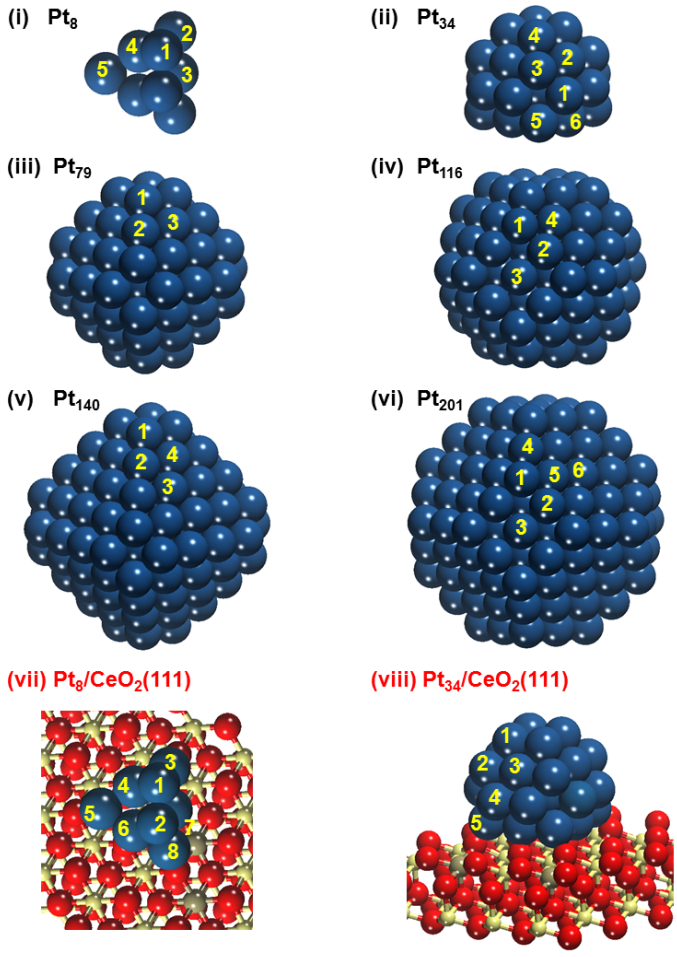

Figure 7.1. Structures of bare and ceria-supported model Pt particles used to model adsorption of CO molecule in various on-top configurations. The numbers indicate the symmetrically non-equivalent Pt atoms as different adsorption sites for on-top CO molecule. Yellow, brown, red, and blue spheres represent Ce^{4+} cations, Ce^{3+} cations, O^{2-} anions, and Pt atoms, respectively.

The calculated CO adsorption energies are defined in such a way that negative values correspond to exothermic adsorption interaction. $Pt_n/CeO_2(111)$ systems with two electrons transferred from each Pt_n particle to the ceria support, thus featuring two Ce^{3+} cations, have been considered as references. Transfer of one electron more or one electron less was estimated to change the total energy of the $Pt_n/CeO_2(111)$ reference at most by 0.1 eV.[9] No corrections for the zero-point energies were applied. The stretching frequencies of CO adsorbates have been calculated numerically in a harmonic approximation via consecutive displacements of C and O atoms by 3 pm in the three Cartesian directions. Inclusion of displacements of the Pt atom on-top of which CO probe is adsorbed in the C-O frequency calculations shifts frequency values at most by 1 cm^{-1}.

To study supported Pt particles, a slab model of $CeO_2(111)$ surface with p(4×4) supercell consisting of six atomic layers, i.e., two O-Ce-O tri-layers, was employed. There, the atoms of the tri-layer closest to the deposited Pt species were relaxed during the geometry optimization, while atoms of the other tri-layer were kept fixed. The lattice parameter of the slab was fixed to reproduce the experimental Ce-Ce (and O-O) nearest distances of 382 pm.

7.3. Results of density functional calculations

System	Site (a)	N_{sites} (b)	N_c[Pt] (c)	E_{ads} (eV) (d)	ν(C-O) (cm^{-1}) (d)
Pt_8	1	2	4	-2.79	2028
	2	2	3	-2.43	2032
	3	1	6	-2.88	2033
	4	2	5	-2.56	2040
	5	1	2	-1.95	2016
Pt_{34}	1	8	6	-2.21	2038
	2	4	9	-1.97	2054
	3	4	6	-2.23	2043
	4	4	6	-2.15	2041
	5	4	5	-2.14	2038
	6	4	7	-2.09	2047
Pt_{79}	1	24	6	-2.20	2043
	2	12	7	-2.10	2047
	3	24	9	-1.99	2069
Pt_{116}	1	24	6	-2.21	2042
	2	24	7	-1.97	2047
	3	6	9	-1.95	2062
	4	24	9	-1.75	2063
Pt_{140}	1	24	6	-2.27	2043
	2	24	7	-1.96	2052
	3	24	9	-1.64	2072
	4	24	9	-1.69	2067
Pt_{201}	1	24	6	-2.05	2039
	2	24	7	-1.98	2046
	3	6	8	-1.74	2056
	4	24	7	-2.04	2044
	5	48	9	-1.70	2068
	6	8	9	-1.53	2076
$Pt_8/CeO_2(111)$	1	1	4	-2.30	2029
	2	1	4	-2.29	2022
	3	1	3	-1.52	2025
	4	1	5	-2.12	2024
	5	1	2	-1.87	2047
	6	1	5	-2.07	2023
	7	1	6	-0.88	2050
	8	1	3	-1.17	2019
$Pt_{34}/CeO_2(111)$	1	4	6	-2.44	2039
	2	4	6	-2.38	2036
	3	4	9	-1.76	2057
	4	8	6	-2.28	2028
	5	4	5	-1.75	2025

Table 7.1. Calculated CO vibrational frequencies and adsorption energies for all symmetrically non-equivalent on-top sites of bare and supported Pt particles: a) Label of the site according to Figure 7.1; b) number of symmetry equivalent sites of the Pt particle N_{sites}; c) coordination number with respect to other Pt atoms N_c(Pt); d) CO binding energy relative to CO in the gas phase; e) calculated CO stretching frequency values corrected with respect to the gas-phase experimental value ν(C-O) = ω(C-O)+14

cm^{-1}; solely these calculated frequency values ν(C-O) are discussed in the present chapter. Calculated electronic states of both supported Pt_8 and Pt_{34} on the CeO_2(111) surface reveal two electron transferred from the Pt particles to the support, with the concomitant reduction of two Ce^{4+} cations to Ce^{3+}. This number is not modified by CO adsorption in most of the Pt sites. Only when CO is adsorbed in sites 4 and 6 of the supported Pt_8 particles the number of Ce^{3+} cations decrease to one, while in site 4 of the Pt_{34} particle it increases to three. All the attempts to converge states with two electrons donated to the ceria surface failed in these three special cases.

Results of our density functional calculations are summarized in Table 7.1. Clear site-dependence of CO stretching frequencies can be seen for larger Pt_{79}, Pt_{116}, Pt_{140}, and Pt_{201} particles exposing relatively well-defined facets, with Pt atoms exhibiting higher coordination number. The adsorption strength for on-top CO molecule follows the trend corner > edge > terrace sites. Generally, the increase of CO stretching frequency follows the same order. Therefore, the coordination number of the Pt atom accommodating adsorbed CO appears to be the main factor of changing the CO frequency values.

Analyzing smaller Pt particles, one can also identify interesting results. At variance with the largest studied Pt aggregates, these particles expose only very small and distorted facets. There, CO adsorption energy and stretching frequency also correlate with the Pt coordination number. However, C-O frequency on-top of Pt atom featuring the highest coordination number 9 on the Pt_{34} particle (site 2) is red-shifted by 22 cm^{-1} compared to that on the central Pt atom of the facets on the largest Pt_{201} particle (site 6). When dealing with such small particles as Pt_8, one notices their high structural flexibility resulting in easily distorted form upon CO adsorption. Nevertheless, the same general trend holds even for such small species: CO frequency is red-shifted when the coordination number of the Pt atom interacting with the CO molecule is decreased.

From a practical point of view, calculations of bare Pt particles in the gas phase are not very demanding and can be performed over a large range of sizes. Nevertheless, usage of bare models is not always sufficient for addressing all significant interactions and effects taking place in the catalytic composites. In modeling studies like this, one has to also explore possible effects of the ceria support on Pt particles, which are

expected to become quite important especially for small particles. Despite modeling of ceria-supported Pt particles is computationally very demanding, we managed to study the smallest ones Pt_8 and Pt_{34} particles supported on a $CeO_2(111)$ slab. As was already mentioned, interaction of Pt particles and $CeO_2(111)$ surface is accompanied by significant electron transfer from the metal to the ceria support.[9] In other words, $CeO_2(111)$ support spontaneously oxidizes the Pt particles upon their formation or deposition. This electron transfer, mainly influencing Pt atoms near or at the interface, is able to modify both the adsorption energy and vibrational frequency of the CO probe molecule. Comparison of calculated data for CO adsorption on bare and supported Pt_8 and Pt_{34} particles (Table 7.1) reveals notably larger site-dependent variations in both the adsorption energies and stretching frequencies for the supported species. Thus, the electronic metal-support interaction appears to be the major cause of these stronger variations of the observables. CO stretching frequencies computed on supported Pt particles follow the same trends as described above for the bare Pt particles.

Figure 7.2 illustrates the size- and site-dependences of the calculated CO stretching frequency. In Figure 7.2a one can see all individual (corrected) calculated CO stretching frequencies. For larger Pt particles (from Pt_{79} to Pt_{201}) the spread in the frequency values mainly originates from the presence of different on-top adsorption sites: terrace, edge and corner ones. However, small particles Pt_8 and Pt_{34} do not expose sites on regular extended facets and thus exhibit a more pronounced shift of the frequency range. The same observation is also valid for the average stretching frequency for each Pt particle. The average CO stretching frequency is plotted in Figure 7.2b together with its standard deviation (note that the total number of sites on each particle has been taken into account). Average frequency values only slightly change for particle sizes larger than Pt_{79}, whereas a drastic decreased can be observed for smaller particles. The presence of the $CeO_2(111)$ support (red data points in Figure 7.2) causes only small changes in the average CO frequency, but induces a substantial increase in the spread (standard deviation) due to the electronic metal-support interactions and accompanying effects. In Figure 7.2c the dependence of the CO stretching frequency on the Pt coordination number is shown. In general, good correlation between these quantities is found, besides larger deviation for supported particles as a result of the metal-support interactions.

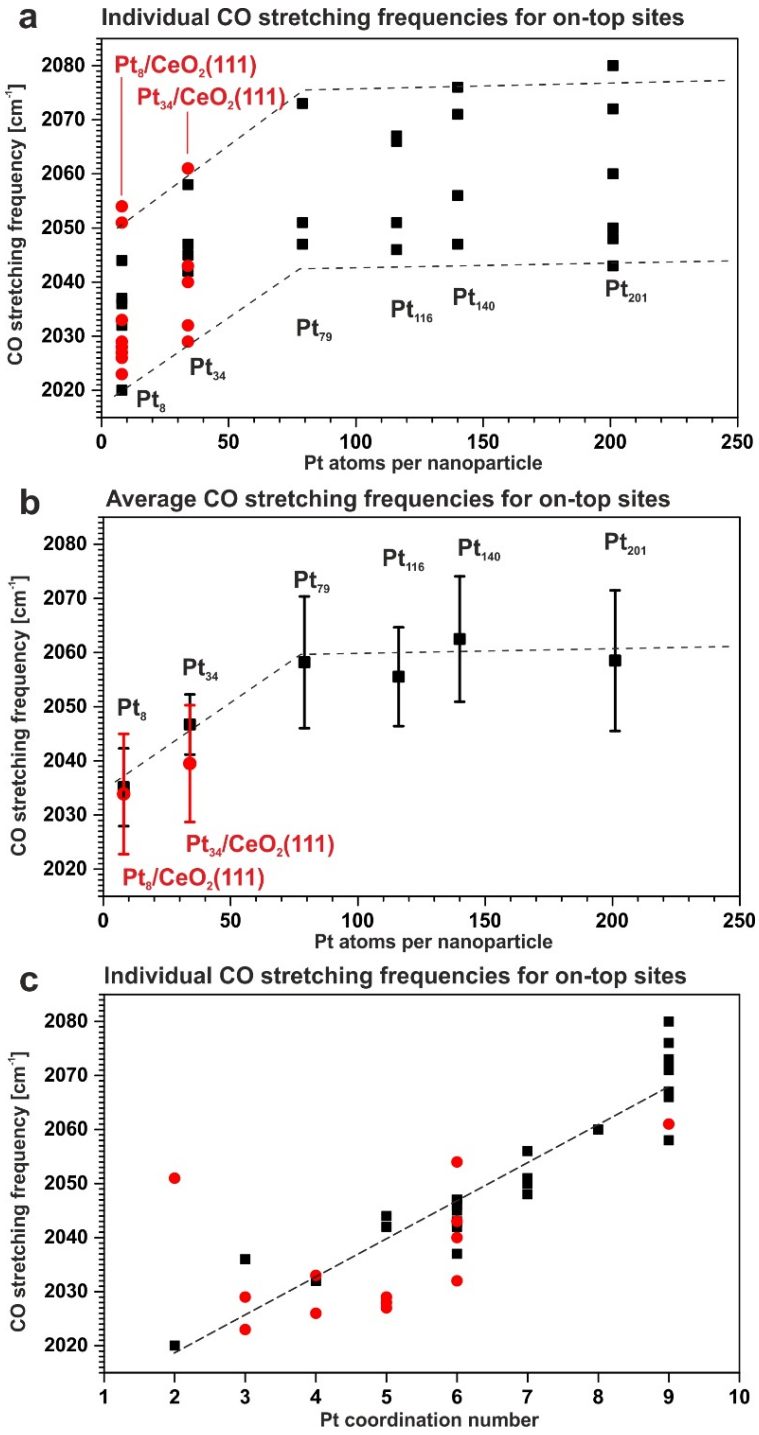

Figure 7.2. Summary of the calculated stretching frequencies on different on-top sites of each Pt model particle (black, bare particles; red, supported particles): a) CO stretching frequencies on all on-top sites of each particle and the corresponding tendency visualized by dashed lines; b) average on-top stretching frequencies and their standard deviation taking into account weights of all on-top sites in each particle; c)

correlation between the CO stretching frequency and the Pt coordination number with respect to neighboring Pt atoms.

7.4. Comparison of calculated and experimental results

In the following we compare the calculated results with the experimental results obtained in the group of Prof. Libuda (Friedrich-Alexander-Universität Erlangen-Nürnberg, Germany), which motivated the present computational study of CO adsorption and vibrations. A direct comparison of the calculated and measured IR data is somewhat complicated, because density-functional calculations describe the low CO coverage limit, with only a single adsorbed CO molecule on each Pt particle. Thus, static and dynamic coupling effects are neglected. Yet, some conclusions regarding the particle size can be derived from the relative band shift. More specifically, experiments performed for samples of Pt(15%)-CeO_x/C/Au show a shift in the CO band of -26 cm^{-1}, in good agreement with the CO band shift calculated for the smallest Pt_8 and Pt_{34} particles (see Figure 7.3).[10] Furthermore, the absence of regular facet CO signals is also consistent with the computational models for small Pt sizes. IR spectra of Pt particles seems to match properly for samples of Pt(8%)- and Pt(15%)-CeO_x/C/Au, and are consistent with particles containing up to 30 Pt atoms. For Pt particles of those two different samples, a diameter below 1 nm has been estimated. This type of species can be denoted as sub-nanometer sized facet-less particles. For Pt_{79} and larger particles, the pronounced calculated CO facet band is also consistent with the CO spectra for on samples of Pt(21%)-CeO_x/C/Au, with higher Pt concentration (Figure 7.3).

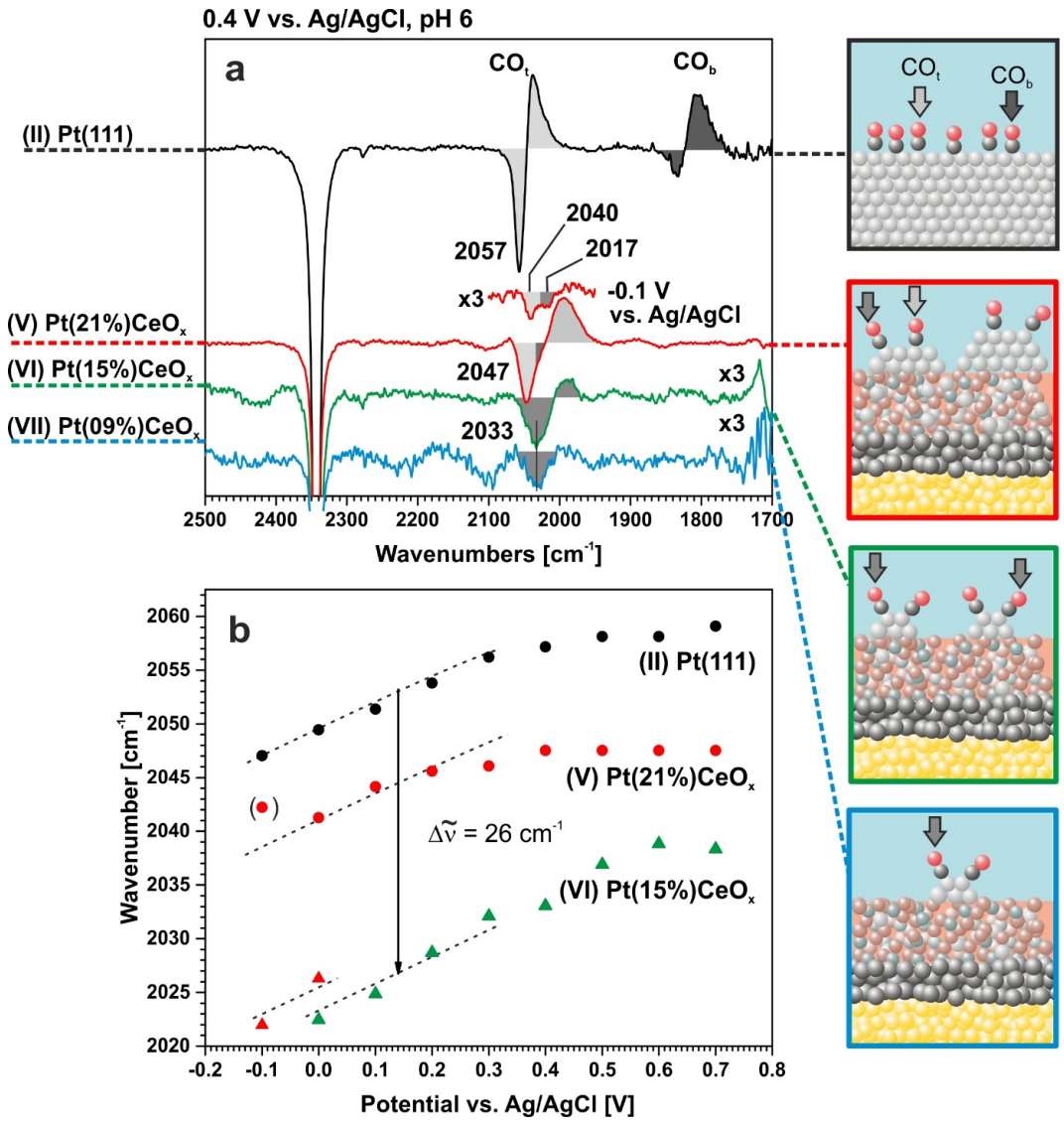

Figure 7.3. Electrochemical IR spectra taken during methanol oxidation on Pt-CeO_x electrocatalysts with different Pt concentration at pH 6. a) IR spectra at an electrode potential of 0.4 $V_{Ag/AgCl}$ and b) peak position of the on-top CO band as function of the electrode potential.[10]

In general, the stability of the supported Pt particles on the CeO_2 support should diminish with decreasing their size. In turn, their propensity to sinter should increase. One can then expect that sub-nano Pt particles in samples of Pt(15%)-CeO_x/C/Au are less stable than larger metal aggregates in samples of Pt(21%)-CeO_x/C/Au. Interestingly, the data obtained after cycling experiments on both types of samples (see Figure 7.4) reveal enhanced stability of sub-nano Pt particles with low Pt concentration under such conditions. The enhanced stability is a result of the strong interactions between the Pt particles and the ceria support.

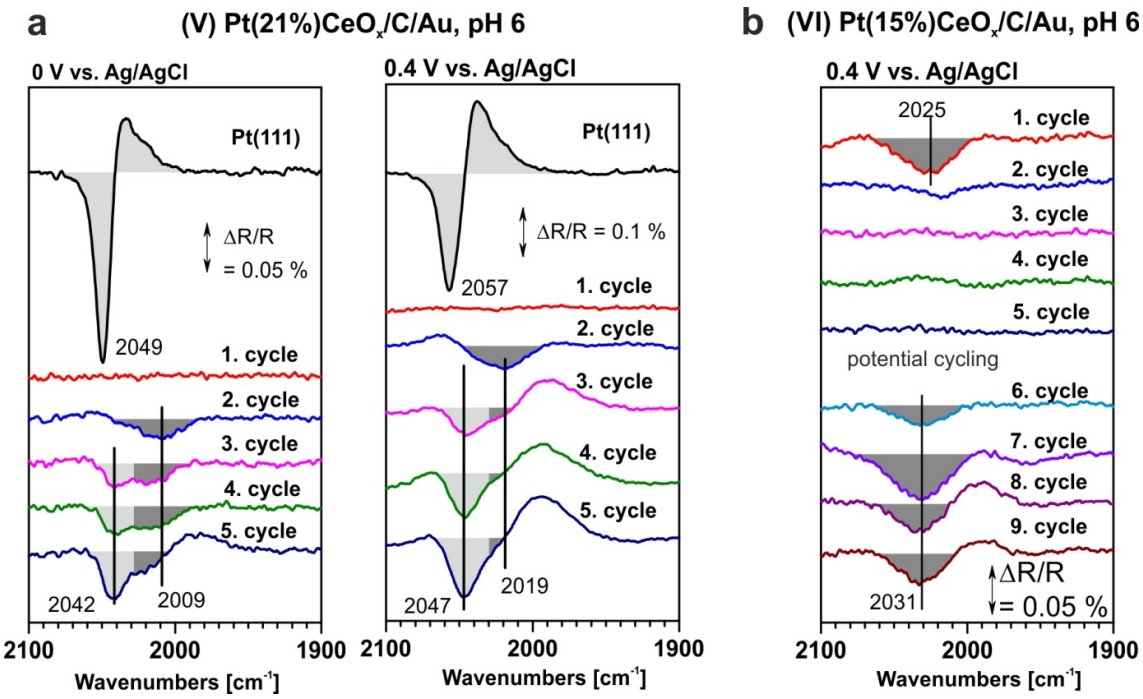

Figure 7.4. Stability of Pt particles on Pt-CeO_x film electrocatalysts with different Pt concentration: Electrochemical IR spectra taken during methanol oxidation cycling on samples a) Pt(21%)-CeO_x/C/Au and b) Pt(15%)-CeO_x/C/Au.[10]

7.4. Overview

Systems related to the usage of CO as a probe molecule for investigating the stability and surface properties of Pt-CeO_2 electrocatalysts for methanol oxidation have been modeled by means of density-functional calculations. It has been shown that on-top CO stretching frequency closely correlates with the coordination number of Pt and, to some extent, with the particle size.

Comparison between experimental and calculated results suggests that the experimentally studied sub-nano Pt particles are formed of ca. 30 or less Pt atoms, featuring sizes of up to 1 nm. Formation of Pt particles with extended (111) terraces is predicted for aggregates containing at least ca. 80 atoms. At low Pt concentration (<15 atom %Pt) sub-nano Pt particles are very stable under conditions of potential cycling, whereas sintering is expected for particles formed at higher Pt concentration (>20 atom %Pt). This is an indication that the ceria support can efficiently stabilize even the smallest Pt particles under the harsh electrochemical conditions.

The present density-functional calculations guided the experimentalists in their better understanding and characterization of the surface structure and composition of Pt-CeO_2 nanomaterials under scrutiny, including the formation and aggregation processes the metal species undergo.

7.5. References

(1) Hadjiivanov, K. I.; Vayssilov, G. N. Characterization of Oxide Surfaces and Zeolites by Carbon Monoxide as an IR Probe Molecule. *Adv. Catal.* **2002**, *47*, 307–511.

(2) Hoffmann, F. Infrared Reflection-Absorption Spectroscopy of Adsorbed Molecules. *Surf. Sci. Rep.* **1983**, *3*, 107.

(3) Greenler, R. G.; Burch, K. D.; Kretzschmar, K.; Klauser, R.; Bradshaw, A. M.; Hayden, B. E. Stepped Single-Crystal Surfaces as Models for Small Catalyst Particles. *Surf. Sci.* **1985**, *152*, 338–345.

(4) Rice, C.; Tong; Oldfield, E.; Wieckowski, A.; Hahn, F.; Gloaguen, F.; Léger, J.-M.; Lamy, C. In Situ Infrared Study of Carbon Monoxide Adsorbed onto Commercial Fuel-Cell-Grade Carbon-Supported Platinum Nanoparticles: Correlation with ^{13}C NMR Results. *J. Phys. Chem. B* **2000**, *104*, 5803–5807.

(5) Arenz, M.; Mayrhofer, K. J. J.; Stamenkovic, V.; Blizanac, B. B.; Tomoyuki, T.; Ross, P. N.; Markovic, N. M. The Effect of the Particle Size on the Kinetics of CO Electrooxidation on High Surface Area Pt Catalysts. *J. Am. Chem. Soc.* **2005**, *127*, 6819–6829.

(6) Fiala, R.; Vaclavu, M.; Rednyk, A.; Khalakhan, I.; Vorokhta, M.; Lavkova, J.; Potin, V.; Matolinova, I.; Matolin, V. Pt–CeO_x Thin Film Catalysts for PEMFC. *Catal. Today* **2015**, *240*, 236–241.

(7) Václavů, M.; Matolínová, I.; Myslivecek, J.; Fiala, R.; Matolín, V. Anode Material for Hydrogen Polymer Membrane Fuel Cell: Pt–CeO_2 RF-Sputtered Thin Films. *J. Electrochem. Soc.* **2009**, *156*, B938.

(8) Fiala, R.; Matolinova, I.; Matolin, V.; Sevcikova, K.; Yoshikawa, H.; Tapan, A. Electro-Oxidation Activity of Pt-CeO_x Carbon Supported Catalysts. *Int. J. Electrochem. Sci.* **2013**, *8*, 10204–10218.

(9) Lykhach, Y.; Kozlov, S. M.; Skála, T.; Tovt, A.; Stetsovych, V.; Tsud, N.; Dvořák, F.; Johánek, V.; Neitzel, A.; Mysliveček, J.; Fabris, S.; Matolín, V.; Neyman, K. M.; Libuda, J. Counting Electrons on Supported Nanoparticles. *Nat. Mater.* **2016**, *15*, 284–288.

(10) Brummel, O.; Waidhas, F.; Faisal, F.; Fiala, R.; Vorokhta, M.; Khalakhan, I.; Dubau, M.; Figueroba, A.; Kovacs, G.; Aleksandrov, H. A.; Vayssilov, G. N.; Kozlov, S. M.; Neyman, K. M.; Matolín, V.; Libuda, J. Stabilization of Small Platinum Nanoparticles on Pt-CeO_2 Thin Film Electrocatalysts During Methanol Oxidation. *J. Phys. Chem. C* **2016**, *120*, 19723–19736.

CHAPTER EIGHT

Conclusions

The following conclusions have been drawn from the results presented in this thesis:

- Adsorption sites at the {100} nanofacets of ceria nanoparticles can effectively anchor a wide range of transition metal atoms in the form of M^{n+} cations. Oxidation of the M centers takes place with the concomitant reduction of n Ce^{4+} cations to Ce^{3+}. Higher oxidation states are favored by transition metals in later periods and in groups more to the left side of the periodic table. The preferred coordination mode of M^{n+} cations at the {100} facets depends on the metal and on its oxidation state. Adsorption in each studied M_1-ceria system is stronger than the binding of the corresponding M atom in a representative M_{79} particle.

- Ceria nanoparticles show the ability to accommodate atomic Pt, Pd, Ni and Cu dopants more easily in surface positions than in bulk positions. Of the surface positions, under-coordinated corner ones are most prone to stabilizing the studied atomically dispersed transition metals. Upon partial reduction of the doped ceria nanoparticles, either via oxygen vacancy formation or homolytic dissociative adsorption of H_2, surface Pt, Pd and Ni dopants feature +2 oxidation states, binding to four O atoms in square-planar fashion. Pt and Pd dopants inside ceria particles can be stabilized in the +4 state. In turn, Cu exhibits +2 or +3 state depending on its location in the ceria particle.

- Pt dopants in bulk ceria feature +4 oxidation state and inherent octahedral coordination by six O atoms, leaving two more distant O atoms less-coordinated. Upon formation of a nearby oxygen vacancy bulk Pt^{4+} is reduced to Pt^{2+} and modifies its environment through a strong lattice distortion to become square-planar coordinated. Nanostructuring of Pt-doped ceria makes the +4 state of Pt energetically favorable up to two oxygen vacancies formed nearby. Formation of the third vacancy destroys the octahedral environment of Pt^{4+} and results in Pt^{2+} in the specific square-planar coordination. Nanostructuring of Pt-doped ceria also facilitates the formation of oxygen vacancies close to the dopant. Such improved oxygen storage capacity is related to the presence of surface Ce atoms accepting electrons of released O atoms more favorably than bulk Ce^{4+} species.

- Atomic Pt^{2+} species adsorbed on {100} nanofacets of ceria are found to be resistant to reduction upon the formation of oxygen vacancies, increasing loading of the doping noble metal and deposition of Sn atoms. The onset of Pt^{2+} reduction to Pt^{0} is determined by the concentration of Ce^{3+} cations in the nanoparticle. To start the reduction, adsorption energy of the Pt^{2+} species needs to fall to around or below the cohesive energy of Pt metal. It is estimated to take place after formation of two oxygen vacancies per Pt adsorbate or adsorption in the vicinity of Pt^{2+} species of approximately three Sn atoms oxidized to Sn^{2+}.

- Our study addressing the usage of CO probe molecule for exploring Pt-CeO_2 electrocatalysts for methanol oxidation revealed that the stretching frequency of on-top CO adsorbed on supported Pt particles correlates with the coordination number of the underlying Pt atom and reflects the particle size. Comparison with experimental results suggests that sub-nanometer particles of ca. 30 or fewer Pt atoms are formed at the applied electrochemical conditions.

- Overall, the studies outlined in the present thesis demonstrated new advantages of using dedicated nanoparticle models together with density-functional calculations to describe ceria-based nanomaterials for catalysis and related applications. This approach used in combination with experimental studies has been shown particularly successful for systems with properties strongly affected by their nanostructure and thus hardly accessible to conventional slab models.

CHAPTER NINE

List of publications

"*High Efficiency of Pt^{2+}-CeO_2 Novel Thin Film Catalyst as Anode for Proton Exchange Membrane Fuel Cells*", R. Fiala, **A. Figueroba**, A. Bruix, M. Vaclavu, A. Rednyk, I. Khalakhan, M. Vorokhta, J. Lavkova, F. Illas, V. Potin, I. Matolinova, K.M. Neyman, V. Matolín, Applied Catalysis B: Environmental, 197, 262-270, 2016.

"*Reactivity of Atomically Dispersed Pt^{2+} Species Towards H_2: Model Pt-CeO_2 Fuel Cell Catalyst*", Y. Lykhach, **A. Figueroba**, M. Farnesi Camellone, A. Neitzel, T. Skála, F.R. Negreiros, M. Vorokhta, N. Tsud, K.C. Prince, S. Fabris, K.M. Neyman, V. Matolín, J. Libuda, Physical Chemistry Chemical Physics, 18, 7672-7679, 2016.

"*Towards Stable Single-Atom Catalysts: Strong Binding of Atomically Dispersed Transition Metals on the Surface of Nanostructured Ceria*", **A. Figueroba**, G. Kovács, A. Bruix, K.M. Neyman, Catalysis Science and Technology, 6, 6806-6813, 2016.

"*Atomically Dispersed Pt, Ni, and Pt Species in Ceria-Based Catalysts: Principal Differences in Stability and Reactivity*", A. Neitzel, **A. Figueroba**, Y. Lykhach, T. Skála, M. Vorokhta, N. Tsud, S. Mehl, K. Ševčíková, K.C. Prince, K.M. Neyman, V. Matolín, J. Libuda, Journal of Physical Chemistry C, 120, 9852-9862, 2016.

"*Stabilization of Small Platinum Nanoparticles on Pt-CeO_2 Thin Film Electrocatalysts During Methanol Oxidation*", O. Brummel, F. Waidhas, F. Faisal, R. Fiala, M. Vorokhta, I. Kalakhan, M. Dubau, **A. Figueroba**, G. Kovács, H.A. Aleksandrov, G.N. Vayssilov, S.M. Kozlov, K.M. Neyman, V. Matolín, J. Libuda, Journal of Physical Chemistry C, 120, 19723-19736, 2016.

"*Redox-Mediated Conversion of Atomically Dispersed Platinum to Sub-Nanometer Particles*", Y. Lykhach, **A. Figueroba**, T. Skála, T. Duchoň, N. Tsud, M. Aulická, A. Neitzel, K. Veltruská, K.C. Prince, V. Matolín, K.M. Neyman, J. Libuda, Journal of Materials Chemistry A, doi: 10.1039/c7ta02204b, 2017.

"*Metal-Doped Ceria Nanoparticles: Stability and Redox Processes*", **A. Figueroba**, A. Bruix, G. Kovács, K.M. Neyman, (submitted to Physical Chemistry Chemical Physics).

CHAPTER TEN

Resum en català

10.1. Introducció

Els catalitzadors són substàncies que, en interaccionar amb els reactius, modifiquen el mecanisme d'una reacció química. Un catalitzador és tant un reactiu com un producte, i tant la seva estructura interna i com la seva concentració són les mateixes al principi i al final de la reacció. Tot hi això, els catalitzadors intervenen activament a la reacció química mitjançant la modificació del perfil energètic del procés, el que canvia la cinètica de la reacció fet que el fa de vital importància no només a la indústria, sinó en qualsevol tipus de procés químic que es vulgui dur a terme de manera controlada. Un catalitzador només actua sobre els paràmetres cinètics de la reacció sense modificar l'equilibri termodinàmic del procés.

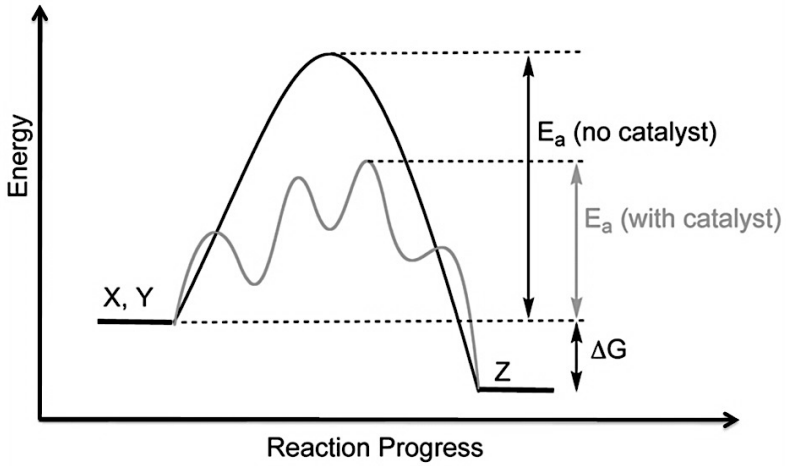

Figura 10.1. Perfil energètic d'una reacció química, on es mostra la evolució de dos reactius (X, Y) cap a la formació d'un producte (Z). La inclusió del catalitzador té com a resultat la modificació del mecanisme de reacció reduint la barrera d'activació.

Els catalitzadors es consideren heterogenis quan reactius i catalitzador presenten fases diferents. La interacció entre reactius i catalitzador es duu a terme a la interfase que es genera entre les dues espècies. Generalment, els reactius s'adsorbeixen a la superfície del catalitzador, provocant un canvi en la estructura electrònica i geomètrica d'aquest.

Un dels materials més utilitzats en el desenvolupament de catalitzadors heterogenis és l'òxid de ceri, CeO_2. El CeO_2 és un component clau dels catalitzadors de triple via utilitzats en el tractament dels gasos d'escapament d'automòbils,[1-3] així com en la eliminació de gasos nocius com el SO_x[4-6] o com a component de catalitzadors per reaccions d'oxidació.[7-14] Més enllà de la reconeguda importància dels materials basats en el CeO_2, es desconeix el funcionament dels mecanismes d'aquests processos a nivell atòmic. D'entre les propietats més estudiades del CeO_2 es troben, entre d'altres, la capacitat inherent d'aquest per dispersar metalls suportats a la seva superfície; la capacitat per incrementar la estabilitat tèrmica dels suports; promoure l'oxidació i reducció de metalls nobles; l'emmagatzematge i proveïment d'oxigen; i la formació de compostos intermetàl·lics.

Moltes de les aplicacions esmentades anteriorment requereixen de metalls de transició com a components dels catalitzadors basats en el CeO_2.[15] D'entre els metalls més utilitzats es troben el Pt, el Pd i el Rh. Es tracten de metalls molt cars, fet que dificulta algunes de les aplicacions industrials dels materials basats en aquest òxid. És important, doncs, trobar alternatives viables i eficients per tal de reduir el preu d'aquests materials catalítics. Una de les opcions possibles és aprofitar una de les propietats del CeO_2 esmentades anteriorment: la capacitat per dispersar metalls a la seva superfície. Aquesta propietat és fonamental per tal de poder obrir noves vies pel disseny de catalitzadors eficients i rendibles on es pugui treure el màxim profit del contingut de metall obtenint el màxim rendiment catalític. La síntesi d'aquest tipus de materials es pot aconseguir dispersant les espècies metàl·liques en forma d'àtoms aïllats a la superfície del suport. Aquest tipus de catalitzadors reben el nom de catalitzadors d'un sol àtom (SACs).[16-18] La formació de SACs estables en condicions de reacció requereix que el suport disposi de llocs d'ancoratge especialment forts per tal de contrarestar la formació d'enllaços metall-metall, donant lloc a processos de sinterització.

En aquesta tesi es realitza un estudi computacional de les interaccions que sorgeixen al depositar metalls de transició en CeO_2. Per tal de dissenyar catalitzadors millorats, eficients i rentables és clau una millor comprensió a nivell atòmic de la estructura dels materials metall-CeO_2.

10.2. Metodologia

Per realitzar els càlculs teòrics s'ha fet servir el programa VASP,[19-21] que tracta els sistemes fent servir el model periòdic i funcions de base basades en ones planes.

Com a metodologia, s'han fet servir càlculs basats en el funcional de la densitat (DFT). Aquesta teoria només té en compte la densitat electrònica $\rho(\vec{r})$ pel càlcul de la energia i de les propietats del sistema. Les bases del DFT van ser establertes el 1927 per Thomas i Fermi, proposant un model basat en un gas uniforme d'electrons per tal d'obtenir un funcional per l'energia cinètica. Més endavant, Hohenberg i Kohn van establir els formalismes del DFT amb dos nous teoremes. El primer teorema estableix que existeix relació entre la $\rho(\vec{r})$ i el potencial extern $\tilde{V}_{ext}$. És a dir, que $\rho(\vec{r})$ determina completament l'energia del sistema mitjançant $\tilde{V}_{ext}$ i l'Hamiltonià electrònic $\hat{H}$. Per altra banda, el segon teorema es tracta d'una aplicació del principi variacional, establint que qualsevol densitat de prova donarà com a resultat una energia superior a la energia del sistema. És a dir, que la densitat electrònica del sistema minimitza l'energia del funcional. Tot hi que el model de Thomas-Fermi proporciona una base de DFT, la seva aplicació pràctica es realment pobre degut a la aproximació abrupte que es realitza per l'energia cinètica. El 1965, Kohn i Sham van abordar aquest problema proposant el càlcul de l'energia cinètica exacta d'un sistema de referència sense interacció amb la mateixa densitat que el sistema real amb interacció. D'aquesta manera, el funcional de la densitat pren la forma

$$F[\rho] = T_S[\rho] + J[\rho] + E_{XC}[\rho] \,, \tag{10.1}$$

on $T_S[\rho]$ correspon a l'energia cinètica del sistema, $J[\rho]$ és el terme de repulsió Coulòmbica i $E_{XC}[\rho]$ és l'energia d'intercanvi i correlació. Aplicant el principi

variacional, s'arriba a les equacions de Kohn-Sham. La seva resolució per sistemes periòdics dona com a resultat orbitals de cristall, on les energies són les bandes electròniques. La forma exacta de $E_{XC}\left[\rho\right]$ no es coneix, pel que existeixen diferents mètodes de càlcul depenent de quina forma d'aproximar $E_{XC}\left[\rho\right]$ s'utilitzi. Dos dels mètodes més emprats es basen en la aproximació de la densitat local (LDA) o en la que es te en compte també el seu gradient (GGA). Malauradament, aquestes aproximacions donen resultats incorrectes per sistemes amb energies de correlació altes. Una manera aproximada per solucionar aquest problema radica en la inclusió d'un terme de repulsió extra, l'anomenat paràmetre de Hubbard *U*, donant lloc als mètodes LDA+*U* i GGA+*U*. En aquest treball s'ha fet servir el mètode GGA+*U* per tal de descriure correctament els electrons f altament correlacionats del Ce parcialment reduït. A més, els electrons de capes internes s'han descrit mitjançant pseudopotencials i, amb el mètode del *Projector Augmented Wave*[22] s'ha descrit la interacció entre els electrons de valència i els de capes internes.

10.3. Metalls de transició atòmicament dispersats en nanopartícules de CeO_2

Com s'ha esmentat a la Secció 10.1, la utilització de metalls de transició com a components de materials catalítics resulta molt cara, pel que s'han de trobar alternatives viables a la utilització d'aquests metalls. Una d'aquestes alternatives es basa en la utilització de manera òptima i eficient del contingut de metall present al material, el qual es pot aconseguir dispersant el metall a la superfície del suport en forma d'àtoms aïllats. Aquest tipus de materials es coneixen com a SACs, i són catalíticament actius per diverses reaccions químiques.[23-29] Tal com s'especifica a la literatura, les espècies actives en aquests SACs són els àtoms metàl·lics oxidats presents a la superfície del suport. És important, llavors, estabilitzar correctament quines són aquestes espècies metàl·liques oxidades per tal de no perdre activitat específica sota les dures condicions de reacció. Per aquest motiu, resulta essencial que el suport presenti suficients llocs superficials capaços d'ancorar els àtoms metàl·lics amb prou força per prevenir processos no desitjats, tals com l'aglomeració o la difusió cap a l'interior del suport.

Una de les arquitectures proposades més prometedores per estabilitzar aquests àtoms metàl·lics són les cares {100} de les nanopartícules (NPs) de CeO_2. Mitjançant càlculs DFT i espectroscòpia de raig X (XPS) es va poder determinar la presència de cations Pt^{2+} adsorbits en aquest llocs superficials mostrant coordinació plano quadrada.[30,31] Aquestes espècies catiòniques són estables fins i tot a altes temperatures (700 K). Sembla ser, doncs, que aquestes cares compleixen els requisits per estabilitzar àtoms de metalls i utilitzar-los per a la preparació de SACs. Per tal d'avaluar aquesta particular propensió per ancorar metalls, s'ha investigat computacionalment la interacció de les cares {100} de NPs de CeO_2 amb varis metalls de transició (M = Fe, Ru, Os, Co, Rh, Ir, Ni, Pd, Cu, Ag i Au). Com a model representatiu de CeO_2, s'ha emprat la NP $Ce_{40}O_{80}$.[32,33] Per tal de comparar la força d'aquesta interacció en front de l'aglomeració en partícules de metall M_n, s'ha calculat també l'energia d'enllaç d'un àtom localitzat a una posició a la vora d'una NP de M_{79}.

A la Figura 10.2 es mostren les estructures optimitzades pels sistemes M_1-$Ce_{40}O_{80}$. L'adsorció de tots i cadascun dels metalls estudiats a la cara {100} té com a resultat l' oxidació de l'àtom metàl·lic, el qual produeix una transferència d'electrons cap als Ce^{4+} de la NP amb la conseqüent formació de Ce^{3+}. El nombre de Ce^{4+} reduïts depèn de la

espècie metàl·lica adsorbida. En general, els resultats calculats indiquen que els metalls de transició pertanyents a períodes alts i grups situats a la esquerra de la taula periòdica estabilitzen millor estats d'oxidació alts.

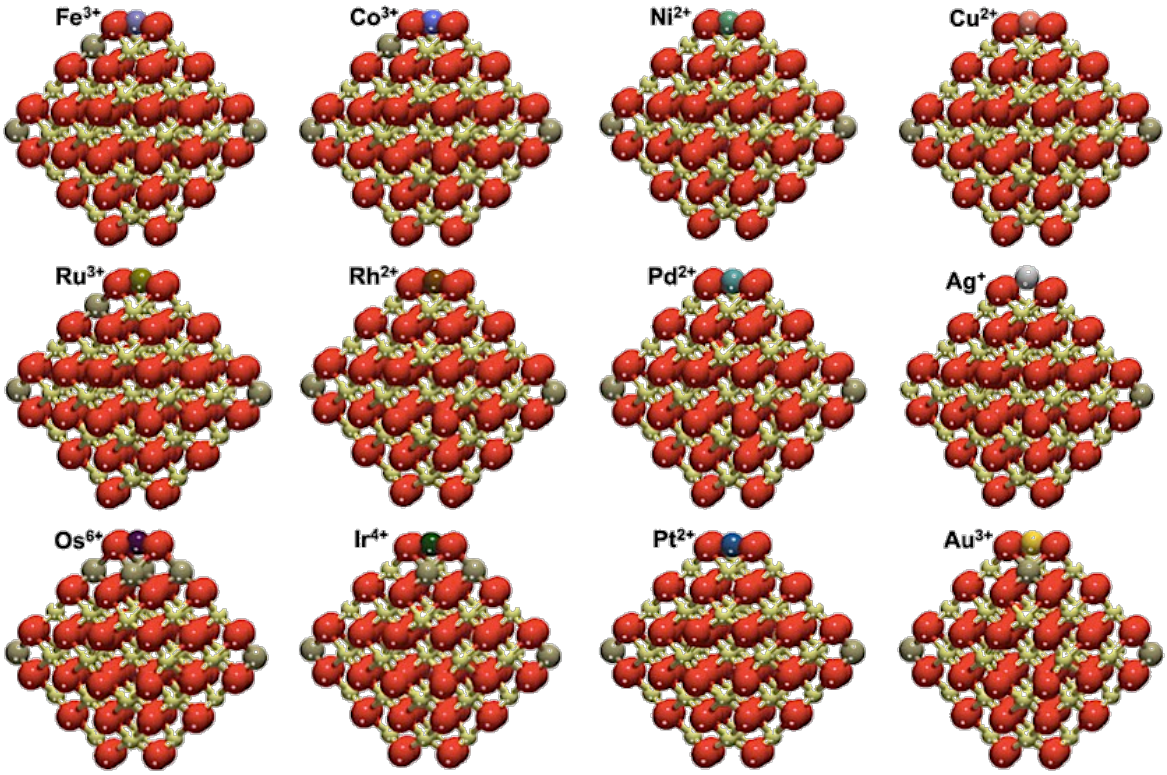

Figura 10.2. Estructures optimitzades sistemes M_1-$Ce_{40}O_{80}$ on es mostra l'adsorció de diferents metalls (M) a les cares {100} de la NP $Ce_{40}O_{80}$. Les boles grogues, marrons i vermelles representen els ions Ce^{4+}, Ce^{3+} i O^{2-}, respectivament.

Els resultats obtinguts indiquen que les cares {100} poden acomodar no només Pt, sinó també tots els altres metalls estudiats. Per tots aquests metalls, l'energia d'adsorció E_{ad} obtinguda a la NP de CeO_2 és més alta en magnitud que l'energia d'enllaç E_{ad79} d'un àtom localitzat a una posició de la vora d'una NP de M_{79}. Aquest fet indica que la dispersió atòmica dels metalls als llocs O_4 de les nanoestructures de CeO_2 està afavorida en front de la formació d'agregats metàl·lics. Per tant, podem esperar que els complexos d'adsorció entre metalls de transició i CeO_2 nanoestructurat siguin resistents a processos de sinterització.

10.4. Estructura i estabilitat redox de nanopartícules de CeO_2 dopades amb metalls de transició

Com s'ha vist a la Secció 10.3, les espècies catiòniques de metalls de transició poden interactuar amb llocs superficials específics presents a les nanoestructures de CeO_2. No obstant, aquesta no és la única forma en que els àtoms metàl·lics poden interactuar amb el suport de CeO_2. De manera alternativa, els metalls poden substituir àtoms de Ce a la estructura cristal·lina. Aquest enfocament es denomina dopatge, i es pot utilitzar per la preparació de catalitzadors.[16-18]

Els dopants es poden classificar d'acord amb el valor del seu estat d'oxidació relatiu al que presenta el metall en el material hoste. Els dopants de valència baixa presenten una valència (estat d'oxidació) més baixa al seu òxid més estable que la del catió que substitueixen en l'òxid hoste. Aquest tipus de dopants indueixen un dèficit d'electrons als anions O^{2-} o, dit d'una altra manera, estats buits (forats) a baixes energies al voltant de la banda de valència del material. Per la seva banda, els dopants de valència alta presenten una valència més alta al seu òxid més estable que la del catió que substitueixen al òxid hoste. En aquest cas, l'efecte dels dopants depèn en la reductibilitat del suport.[34,35] Tot hi que s'han dedicat molts esforços a entendre la interacció entre els metalls dopants i el CeO_2, no s'han trobat estudis a la literatura on es consideri el dopatge amb metalls de transició en nanoestructures de CeO_2. Per aquest motiu, s'ha estudiat la substitució d'àtoms de Ce amb quatre metalls rellevants tecnològicament (Pt, Pd, Ni i Cu) en diferents posicions d'una NP de CeO_2. S'han tingut en compte també dos possibles processos de reducció presents en les condicions d'operació de les piles de combustible: i) la formació de vacants d'oxigen (O_{vac}) i ii) la adsorció dissociativa de H_2.

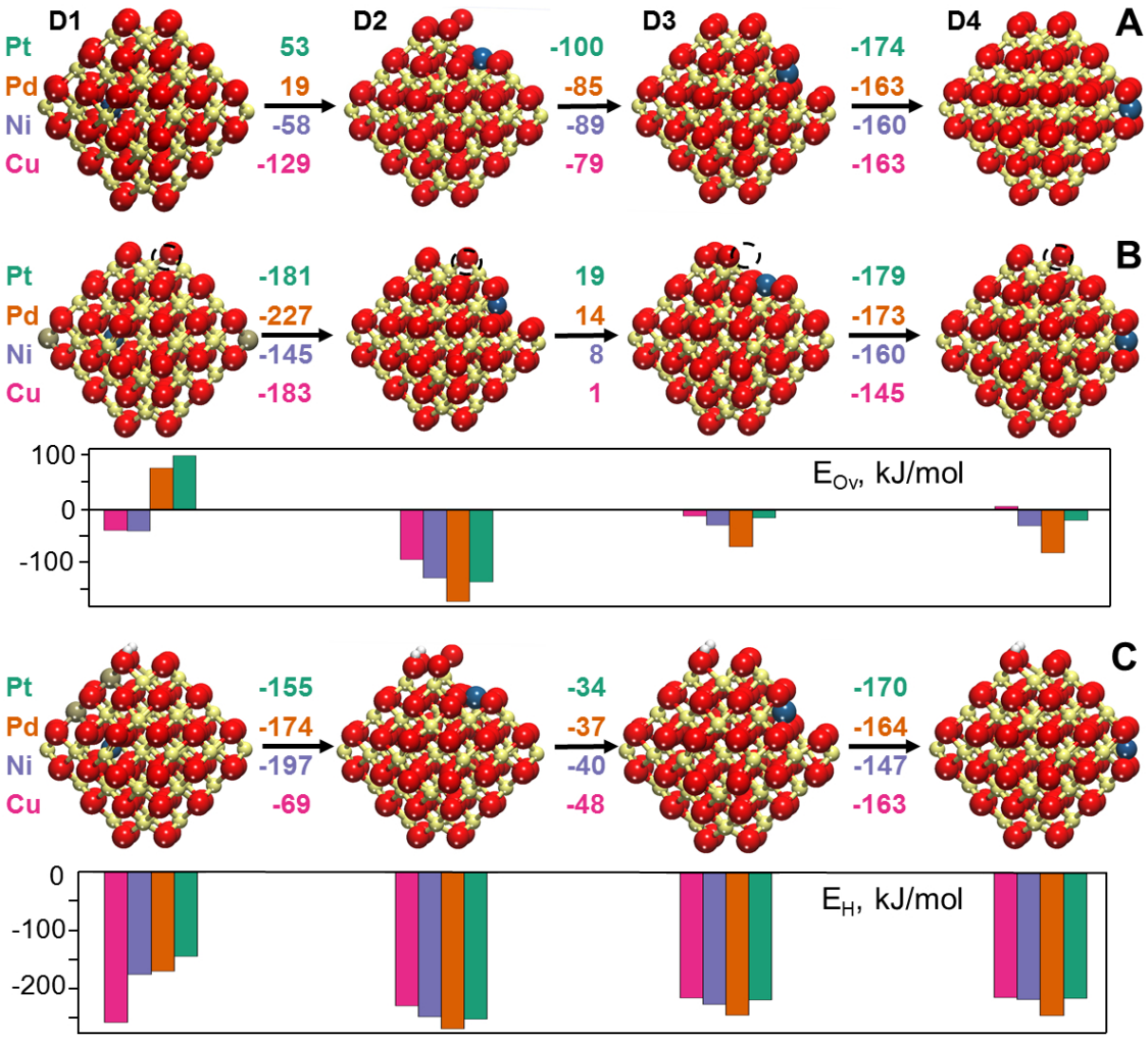

Figura 10.3. Estructures no reduïdes (A – $PtCe_{39}O_{80}$) i parcialment reduides (B – $PtCe_{39}O_{79}$, C – $H_2/PtCe_{39}O_{80}$) de NP de CeO_2 dopades amb Pt, el qual substitueix un àtom de Ce a l'interior (D1), a la cara (D2, D3) o a la cantonada (D4). Les estructures corresponents al dopatge amb altres metalls M = Pd, Ni i Cu son similars. Les boles representades són: O – vermell, Ce – groc (+4) o marró (+3), Pt – blau, H – blanc. Els cercles discontinus indiquen la posició de la vacant d'oxigen. Les energies relatives de les diferents estructures amb el mateix dopant M es troben llistades (en kJ mol^{-1}). Els gràfics als panells B i C il·lustren, respectivament, les tendències en les energies de formació de vacants calculades i en les energies d'adsorció dels àtoms de H.

Per sistemes no reduïts, la substitució a la posició interior de la NP dóna lloc a la formació de cations Pt^{4+} i Pd^{4+} octaèdrics. Per la seva banda, Ni i Cu localitzats a

l'interior de la NP presenten estats d'oxidació +3. En posicions superficials, tots els dopants presenten estat d'oxidació +3, sent la posició situada a la cantonada de la NP la més estable per a la substitució. Els resultats obtinguts impliquen que els dopants localitzats a l'interior de la NP patiran processos de difusió cap a posicions superficials. La presencia de metalls en estats d'oxidació +3, el qual és un estat poc comú per les espècies estudiades, suggereix que els sistemes corresponents al model $MCe_{39}O_{80}$ puguin ser fàcilment reduïbles sota condicions experimentals. Per tal de tractar aquests possibles processos de reducció, s'ha estudiat l'efecte en els metalls dopants de la formació d'una vacant d'oxigen i de l'adsorció dissociativa homolítica d'una molècula de H_2.

Per posicions interiors, només Pt i Pd són capaços de mantenir l'estat d'oxidació +4. Per a la resta de posicions, tots els metalls es troben en estat d'oxidació +2. Això vol dir que els electrons donats per l'oxigen o pels dos àtoms d'hidrogen són transferits al metall i als forats creats als oxígens. Només pel cas del Cu es troben diferents estats d'oxidació, +2 i +3, depenent del procés i de la posició del dopatge.

Els resultats presentats en aquesta secció proporcionen informació sobre com s'estabilitzen les espècies catiòniques presents en posicions de la xarxa del CeO_2, els quals poden ser d'utilitat en la preparació de materials catalítics amb SACs.

10.5. Espècies de Pt^{4+} i Pt^{2+} dopants en CeO_2: Efecte de la nanoestructuració

Un dels majors objectius en catàlisi és el desenvolupament de materials rentables per reaccions d'oxidació a baixa temperatura. Una de les propietats clau que han de presentar els materials potencials per aquest tipus d'aplicació és la seva capacitat per emmagatzemar oxigen (OSC). Per aquest motiu, s'ha estudiat com la OSC del CeO_2 es veu afectada pel dopatge amb Pt. Per tal de tenir en compte quin és el possible efecte de la nanoestructuració, s'han estudiat tant models de CeO_2 3D estesos com models de NPs amb diferents concentracions de Pt.

Els resultats obtinguts per sistemes de CeO_2 dopats amb Pt mostren que el metall noble només es pot trobar en l'estat d'oxidació +4 si presenta coordinació octaèdrica, enllaçant 6 O i deixant els altres dos O poc coordinats. En presència d'una O_{vac}, l'àtom de Pt pateix la reducció a Pt^{2+} amb la conseqüent modificació en la coordinació, sent aquesta plano quadrada. Els resultats obtinguts indiquen que la sola presència de l'àtom de Pt a la xarxa del CeO_2 provoca una disminució de la energia necessària per formar la vacant d'oxigen E_{vac} en 218 kJ mol^{-1}. La major predisposició del Pt a acceptar els electrons deixats per l'oxigen en formar la vacant està relacionada amb els cations Ce^{3+}. La reducció dels cations Ce^{4+} a Ce^{3+} implica un canvi en el volum, fet que introdueix tensions estructurals i electròniques a la xarxa de CeO_2. Per la seva banda, la reducció del Pt^{4+} a Pt^{2+} només implica un canvi de coordinació, deixant la estructura de la xarxa pràcticament sense modificar. Aquest fet queda reforçat al examinar el valor obtingut per la formació d'una segona vacant al costat del Pt^{2+}, el qual és 162 kJ mol^{-1} més alt que l'obtingut per la primera vacant. En aquest cas, el Pt no és la espècie que accepta els electrons deixats per l'àtom de O, sinó que la formació de la vacant implica la reducció de dos Ce^{4+} a Ce^{3+}. Les tensions estructurals que s'introdueixen a la xarxa es veuen reflectides en aquests 162 kJ mol^{-1}.

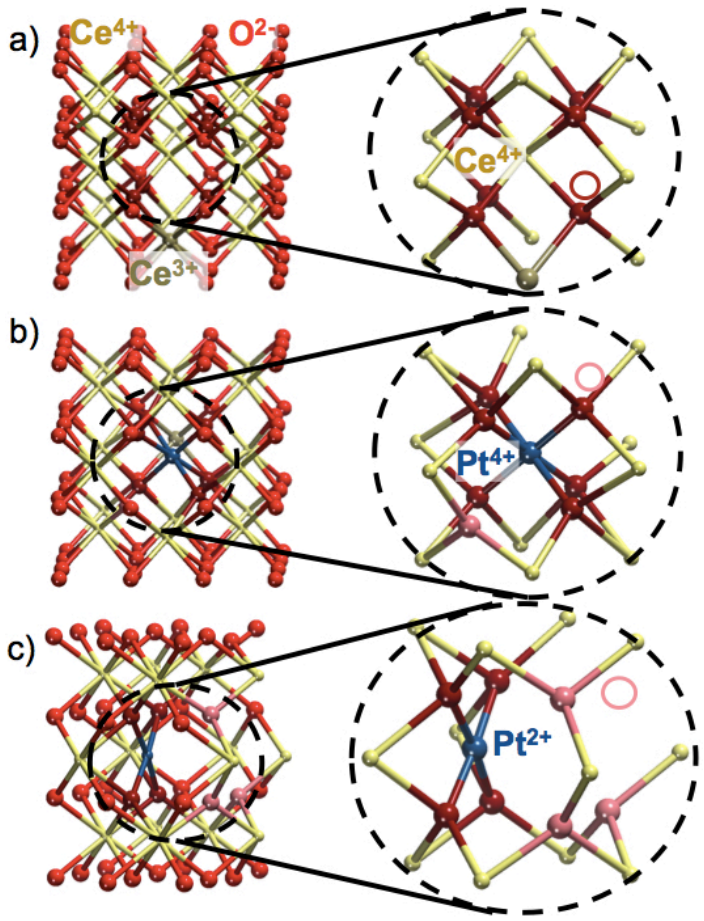

Figura 10.4. Estructures obtingudes després de la formació d'una vacant d'oxigen en CeO_2 al costat de a) cations Ce^{4+}; b) cations Pt^{4+}; c) cations Pt^{2+}. Les esferes grogues, vermelles i blaves representen els àtoms de Ce, O i Pt, respectivament. Les esferes vermell fosc i rosa corresponen a ions O^{2-} propers i distants al Pt, respectivament.

La nanoestructuració dels sistemes de CeO_2 dopats amb Pt produeixen significants efectes sobre la OSC del material. Les espècies de Pt^{4+} semblen poder sobreviure a la formació de fins a dos O_{vac} properes. Per tots els models de NP estudiats (amb cuatre, un o cap àtom de Pt^{2+} presents al les cares {100}) les energies de formació de vacant obtingudes són més baixes que les obtingudes fent servir models 3D estesos. La formació d'una tercera vacant destrueix la coordinació octaèdrica del Pt^{4+}, provocant la reducció del dopant a l'estat d'oxidació +2 i donant lloc a la típica coordinació plano quadrada, amb quatre anions O^{2-}. Es pot concloure, doncs, que la nanoestructuració provoca una millora en les propietats de OSC dels materials de CeO_2 dopats amb Pt.

Com s'ha esmentat prèviament, els cations Ce^{3+} juguen un paper clau en aquesta millora. Els cations Ce^{4+} localitzats a la superfície de la NP són fàcilment reduïbles donada la seva baixa coordinació i llavors, al contrari que els cations Ce^{4+} presents a l'interior de la xarxa de CeO_2, poden acceptar fàcilment els electrons deixats per l'oxigen al formar la vacant. A més, el major volum dels cations Ce^{3+} pot ser més fàcilment acomodat a la superfície.

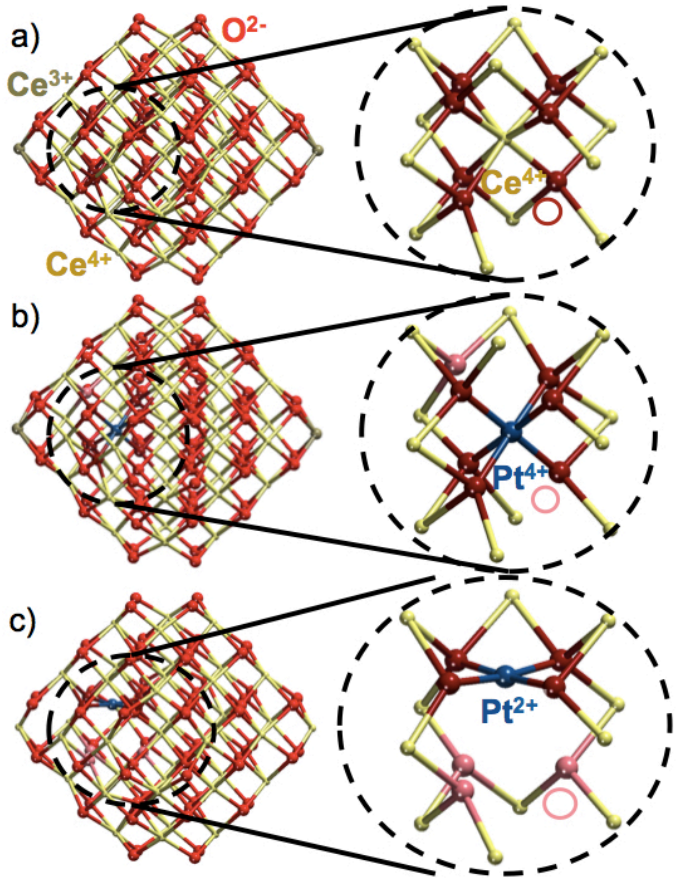

Figura 10.5. Estructures obtingudes després de la formació d'una vacant d'oxigen en la NP $Ce_{40}O_{80}$ al costat de a) cations Ce^{4+}; b) cations Pt^{4+}; c) cations Pt^{2+}. Les esferes grogues, vermelles i blaves representen els àtoms de Ce, O i Pt, respectivament. Les esferes vermell fosc i rosa corresponen a ions O^{2-} propers i distants al Pt, respectivament

Pel que fa a l'efecte del contingut de metall, sembla ser que en general els valors de E_{vac} augmenten en incrementar la concentració de metall, el qual també fa augmentar la quantitat de Ce^{3+} a la NP. Existeix, doncs, una relació directa entre els valors de E_{vac} amb el número de cations Ce^{3+}.

10.6. Desestabilització d'espècies catiòniques superficials de Pt^{2+} a Pt^0 metàl·lic

Com es va mostar a la Secció 10.3, els SAC són una proposta prometedora pel desenvolupament de materials catalítics més rentables que els utilitzats habitualment. Tot hi aquest fet, existeixen diverses aplicacions que requereixen la presència de petits agregats metàl·lics per tal de dur a terme determinades reaccions químiques. Un exemple d'aquest tipus de processos és la dissociació d'hidrogen per aplicació en ànodes de piles de combustible. Per aquest motiu s'han estudiat els efectes de possibles factors que puguin desestabilitzar les espècies de Pt^{2+} presents en la superfície de nanoestructures de CeO_2. Els factors que s'han tingut en compte són: i) formació d'un nombre divers de vacants d'oxigen, ii) l'efecte de la concentració de metall i iii) l'adsorció d'espècies de Sn en posicions properes als cations Pt^{2+}. D'aquesta manera, a més de poder tenir un millor coneixement sobre l'estabilitat de les espècies de Pt^{2+} adsorbides a la superfície de CeO_2, es poden dissenyar rutes per la preparació de NPs sub-nanomètriques de metall en suports de CeO_2.

Pel que fa la formació de O_{vac}, els resultats obtinguts indiquen que tot hi que els àtoms de O localitzats a les cares {100} són els menys coordinats i, per tant, els més làbils, la presència de espècies de Pt^{2+} provoca que siguin difícilment eliminables. Aquest fet es deu a la formació de l'estructura de coordinació plano quadrada [PtO_4], on el Pt interacciona fortament amb els quatre anions O^{2-} que formen la cara. Per aquest motiu, la formació de O_{vac} estarà limitada als O superficials que no estiguin directament enllaçats al Pt. Els resultats obtinguts suggereixen la existència d'un llindar energètic que ha de ser superat per tal de provocar la reducció del Pt^{2+} a Pt^0. Aquest llindar es pot relacionar amb la energia de cohesió el Pt metàl·lic, la qual és de 5.85 eV. D'aquesta manera, la reducció d'espècies de Pt^{2+} estarà afavorida quan la E_{ad} del Pt a la NP sigui més baixa que el valor de la energia de cohesió del Pt metàl·lic. Sembla ser que aquest fet es dona quan es formen aproximadament dos O_{vac} per àtom de Pt. La formació de O_{vac} implica la reducció de Ce^{4+} a Ce^{3+}, els quals són més voluminosos i introdueixen desestabilització estèrica, modificant la estructura de la NP. De forma anàloga, l'increment en la concentració de metall provoca la formació de espècies Ce^{3+}.

Pel que fa l'adsorció d'un àtom de Sn^{2+} proper al Pt^{2+}, sembla ser que quan el metall s'adsorbeix produeix una reducció en la E_{ad} del Pt de 81 kJ mol^{-1}. L'adsorció d'un segon àtom de Sn debilita significativament l'adsorció del Pt a la cara {100}, fins a

un valor de -461 kJ mol^{-1}. Aquest valor és encara massa gran com per que l'àtom de Pt es redueixi a Pt^0. Cal mencionar que la estabilitat del Pt^{2+} està fortament correlacionada amb la llargada dels enllaços Pt-O en la coordinació plano quadrada. Finalment, la reducció a Pt^0 es produeix quan en adsorbir un tercer àtom de Sn^{2+} al costat del Pt, produint un canvi de coordinació amb formació de la estructura lineal [PtO_2]. Curiosament, l'adsorció d'aquest tercer àtom de Sn sembla estar lleugerament afavorida en relació als dos primers àtoms de Sn adsorbits. Aquest fet és degut a que el tercer àtom de Sn interacciona amb un anió O^{2-} el qual està més feblement enllaçat a l'àtom de Pt, pel que pot interaccionar més fortament amb el Sn.

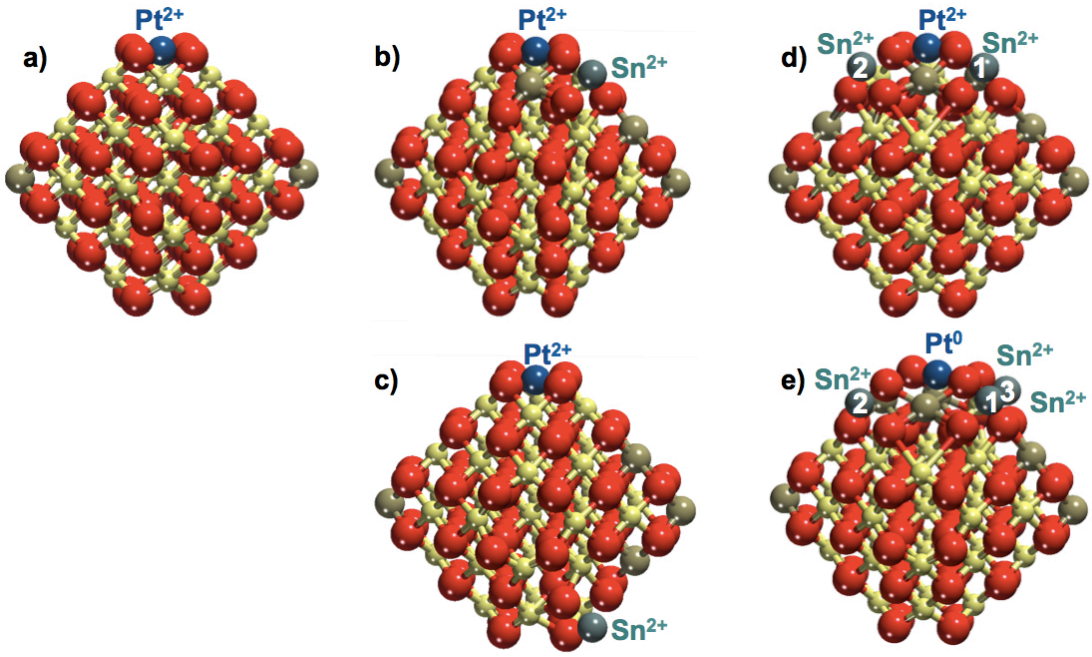

Figura 10.6. Estructures de Pt-$Ce_{40}O_{80}$ obtingudes en adsorbir àtoms de Sn. Els sistemes corresponen a l'adsorció de (a) cap Sn, (b-c) un Sn, (d) dos Sn i (e) tres àtoms de Sn. Les boles grogues, marrons, vermelles i grises representen els ions Ce^{4+}, Ce^{3+}, O^{2-} i Sn^{2+}, respectivament. Els números en (d) i (e) indiquen diferent àtoms de Sn.

Els resultats obtinguts mostren que les espècies de Pt^{2+} adsorbides a les cares {100} de nanoestructures de CeO_2 són resistents a l'adsorció de fins a tres àtoms de Sn. Aquests resultats estan en bona concordança amb els obtingut experimentalment en condicions de buit ultra alt (UHV), els quals suggereixen que la presència de 6 cations Ce^{3+} o, el que és el mateix, 3 àtoms de Sn són necessaris per reduir el Pt^{2+} a Pt^0.

10.7. Anàlisi de freqüències de CO per a la caracterització de films de Pt-CeO_2

Un dels passos més importants en el desenvolupament de catalitzadors és la caracterització correcta i precisa del material. Això és degut a que el rendiment catalític del compost pot dependre de la natura de les espècies metàl·liques suportades a la seva superfície. Per aquesta raó, existeixen una gran varietat de tècniques experimentals per tal de caracteritzar correctament el material. En aquesta Secció es tractarà una d'aquestes tècniques: l'adsorció de CO com a molècula infraroja sonda. Aquesta tècnica es basa en el canvi que presenten les freqüències vibracional C-O en adsorbir la molècula de CO en llocs superficials del material catalític.[36] D'aquesta manera, es pot obtenir informació sobre l'estat d'oxidació,[37] estructura[38] i mida dels metalls.[39,40]

En aquesta Secció, s'ha analitzat el canvi observat en les freqüències vibracional de la molècula de CO en adsorbir-se de forma "on top" en agregats de Pt de diferents mides. A més, s'ha estudiat el possible efecte del suport de CeO_2 en els valors de freqüències. Aquest tipus de materials de Pt-CeO_2 es poden utilitzar en ànodes per piles de combustible, els quals mostren bona activitat i estabilitat. Els clústers de Pt que s'han estudiat van des de NP petites de 8 àtoms fins a partícules grans i regulars formades per 201 àtoms. L'efecte del suport de CeO_2 en les propietats d'adsorció del CO s'ha analitzat per dos agregats de Pt: Pt_8 i Pt_{34}.

Els resultats obtinguts indiquen que els valors de les freqüències de CO presenten una clara dependència del lloc d'adsorció superficial. Bàsicament, les partícules més grans presenten cares grans i ben definides, on els àtoms de Pt exhibeixen números de coordinació alts. La força d'adsorció entre la molècula de CO i l'àtom de Pt sembla seguir la tendència cantonada > vora > cara. Pel que fa els valors de freqüències de CO segueixen, en general, el mateix ordre en increment. Es pot concloure doncs, que el número de coordinació de l'àtom de Pt sembla ser un dels factors més importants en el canvi en els valors les freqüències de CO.

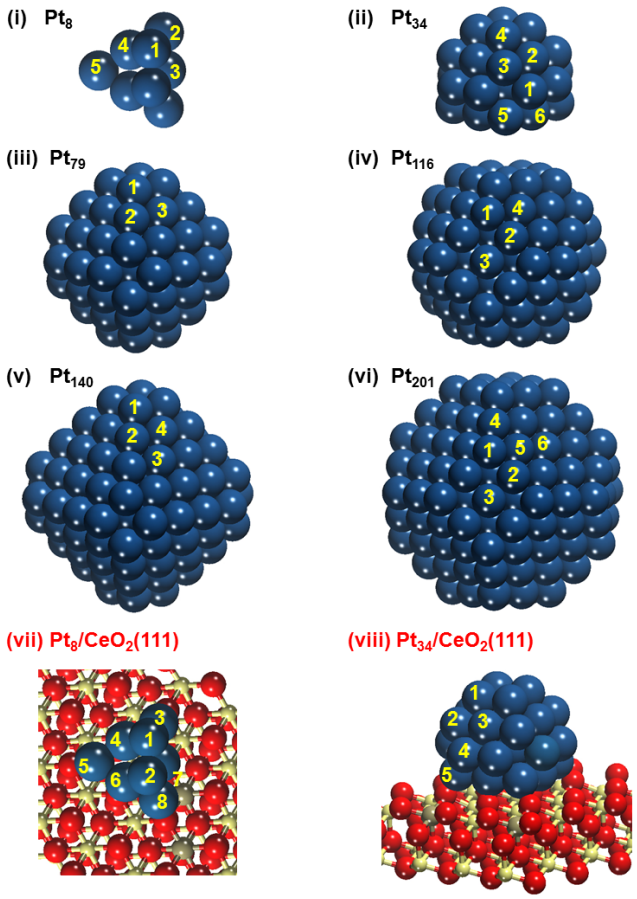

Figure 10.7. Estructures obtingudes a partir de l'optimització DFT de partícules de Pt amb i sense suport per a l'adsorció de CO. Els números indiquen els àtoms de Pt simètricament no equivalents per a cada sistema. Les boles grogues, marrons, vermelles i blaves representen els cations Ce^{4+} i Ce^{3+}, els anions O^{2-} i els àtoms de Pt, respectivament.

Per partícules petites, sembla ser que el número de coordinació de l'àtom de Pt torna a ser un dels factors més importants tant en l'adsorció del CO com pels valors de freqüències de vibració.

Pel que fa els sistemes suportats, cal esmentar en primer lloc que la interacció entre el CeO_2 i les partícules de Pt és molt forta, el que causa la transferència espontània d'electrons des de l'agregat de Pt cap a la superfície de CeO_2.[41] En altres paraules, el suport de CeO_2 oxida les partícules de Pt un cop s'han format o adsorbit a la seva superfície. Aquest efecte es produeix principalment als àtoms de Pt propers a la interfase i és important tenir-lo en compte per les conseqüències que genera tant a les

energies d'adsorció com a les freqüències del CO. Mitjançant la comparació de les adsorcions de la molècula de CO en els sistemes de Pt_8 i Pt_{34} amb i sense suport, es pot observar que les variacions en les energies de adsorció i en les freqüències de vibració relacionades amb la dependència del lloc d'adsorció són molt més fortes pels sistemes suportats. Sembla ser, doncs, que les interaccions electròniques metall-suport són la principal causa d'aquests canvis en les propietats del CO.

La comparació dels resultats teòrics amb els experimentals suggereix que les espècies subnanomètriques de Pt contenen al voltant de 30 àtoms o menys, mesurant menys de 1 nm.

10.8. Conclusions

A partir dels resultats obtinguts en aquesta tesi, s'han extret les següents conclusions:

- Els llocs específics d'adsorció presents a les nanopartícules de CeO_2, les cares {100} poden ancorar de manera efectiva una gran varietat d'àtoms metàl·lics en la forma de cations M^{n+}. L'adsorció dels metalls en aquests llocs provoca l' oxidació d'aquests, amb la conseqüent reducció de cations Ce^{4+} a Ce^{3+}. Els estats d'oxidació alts estan més afavorits per metalls de transició pertanyents a períodes alts i grups situats a la esquerra de la taula periòdica. Els modes de coordinació dels cations M^{n+} localitzats a la cara {100} depenen de la natura del metall i del seu estat d'oxidació. L'adsorció de tots els metalls estudiats a la NP de CeO_2 és més forta que l'energia d'enllaç del corresponent àtom M a la NP metàl·lica M79.

- Les NPs de CeO_2 presenten la capacitat de acomodar metalls dopants més fàcilment a la seva superfície que no a posicions interiors. En particular, les posicions menys coordinades semblen ser les més propenses per estabilitzar els metalls de transició dispersats atòmicament. Per tal d'analitzar tant la estabilitat de les espècies dopants en estats d'oxidació baixos com l'efecte del dopatge en la reductibilitat del sistema, s'han considerat dos processos redox: i) la formació d'una vacant d'oxigen i ii) la dissociació homolítica d'una molècula de H_2. Les espècies dopants Pt, Pd i Ni presenten estats d'oxidació +2 en coordinació plano quadrada. Només Pt i Pd semblen poder oxidar-se fins l'estat +4, el que ocorre només per substitucions a posicions interiors de la NP. Per la seva banda, el Cu pot presentar els estats d'oxidació +2 o +3, dependent de la seva localització a la NP i del procés de reducció dut a terme.

- Els resultats obtinguts per sistemes de CeO_2 amb Pt dopant en posicions internes indiquen que només pot presentar l'estat d'oxidació +4 quan es troba coordinat octaèdricament a 6 àtoms de O. En presència d'una vacant d'oxigen, els àtoms

de Pt^{4+} tendeixen a reduir-se a Pt^{2+}, modificant el seu entorn de coordinació mitjançant una distorsió a través de la xarxa per adoptar una coordinació plano quadrada. La nanoestructuració dels sistemes de CeO_2 dopats amb Pt resulta en l'estabilització de l'estat d'oxidació +4 pel Pt fins a la formació de dos vacants d'oxigen. La formació de la tercera vacant destrueix la coordinació octaèdrica del Pt^{4+}, causant la reducció de l'àtom de metall dopant a l'estat +2 amb l'adopció de la coordinació plano quadrada. Per tant, la nanoestructuració dels sistemes de CeO_2 dopats amb Pt condueix a una millora en la capacitat d'emmagatzematge d'oxigen. L'origen d'aquesta millora està relacionat amb la presència d'àtoms de Ce superficials, els quals són més propensos a acceptar els electrons deixats per l'oxigen.

- Sembla ser que les especies catiòniques de Pt^{2+} adsorbides als llocs {100} de nanoestructures de CeO_2 són estables fins a formar dos vacants d'oxigen per àtom de Pt. La reducció d'aquestes espècies comença a estar afavorida quan l'energia d'adsorció del Pt baixa per sota de la energia de cohesió del Pt metàl·lic. La formació de un número suficient de cations Ce^{3+} a partir de la eliminació d'àtoms d'oxigen facilita la reducció a Pt^0. Per la seva banda, l'adsorció d'àtoms de Sn en llocs propers al Pt^{2+} té com a resultat la oxidació dels àtoms de Sn a l'estat +2 amb la conseqüent formació de dos cations Ce^{3+} per catió Sn^{2+}. La reducció del Pt2+ està, llavors, determinada per la concentració de Ce^{3+} a la NP. En aquest cas, són necessaris uns 6 cations Ce^{3+} al voltant del Pt^{2+} per reduir-lo a Pt^0.

- Tant els valors de les energies d'adsorció com les freqüències vibracionals de la molècula de CO en partícules de Pt, tant amb com sense suport, semblen estar fortament relacionades amb el número de coordinació de l'àtom de Pt i, en menor mesura, amb el tamany de partícula. Per a partícules suportades, la forta interacció metall-suport produeix l'oxidació de les partícules de metall, el qual provoca una major variació en els valors de les propietats del CO. La comparació dels resultats teòrics amb els experimentals suggereix que les

espècies subnanomètriques de Pt contenen al voltant de 30 àtoms o menys, mesurant menys de 1 nm.

- Els estudis presentats en aquesta tesis demostren els avantatges de fer servir models de nanopartícules combinats amb càlculs del funcional de la densitat per tal de descriure nanomaterials basats en el CeO_2 per aplicacions catalítiques. A més, la complementació d'aquest enfoc amb els estudis experimentals ha demostrat ser tot un èxit per l'estudi de sistemes amb propietats que es veuen fortament afectades per la seva nanoestructura i, per tant, serien directament accessibles de descriure fent servir models convencionals de lloses.

10. 9. Referències

(1) Summers, J. C.; Ausen, S. A. Interaction of Cerium Oxide with Noble Metals. *J. Catal.* **1979**, *58*, 131–143.

(2) Kim, G. Ceria-Promoted Three-Way Catalysts for Auto Exhaust Emission Control. *Sect. Title Air Pollut. Ind. Hyg.* **1982**, *21*, 267–274.

(3) Gandhi, H.; Piken, A.; Shelef, M.; Delosh, R. Laboratory Evaluation of Three-Way Catalysts. *SAE Pap. 760201* **1976**, *55*.

(4) Bhattacharyya, A. A.; Woltermann, G. M.; Yoo, J. S.; Karch, J. A.; Cormier, W. E. Catalytic SO_x Abatement: The Role of Magnesium Aluminate Spinel in the Removal of SO_x from Fluid Catalytic Cracking (FCC) Flue Gas. *Ind. Eng. Chem. Res.* **1988**, *27*, 1356–1360.

(5) Yoo, J. S.; Jaecker, J. A. U.S. Patent 4,469,589, 1984.

(6) Bertolacini, R. J.; Hirschberg, E. H.; Modica, F. S. U.S. Patent 4,497,902, 1985.

(7) Kilbourn, B. T. The Role of the Lanthanides in Applied Catalysis. *J. Less-Common Met.* **1986**, *126*, 101–106.

(8) Liu, W.; Flytzani-Stephanopoulos, M. Total Oxidation of Carbon Monoxide and Methane over Transition Metal-Fluorite Oxide Composite Catalysts. *J. Catal.* **1995**, *153*, 304–316.

(9) Brazdil, J. F.; Grasselli, R. K. Relationship between Solid State Structure and Catalytic Activity of Rare Earth and Bismuth-Containing Molybdate Ammoxidation Catalysts. *J. Catal.* **1983**, *79*, 104–117.

(10) Imamura, S.; Uematsu, Y.; Utani, K.; Ito, T. Combustion of Formaldehyde on Ruthenium / Cerium (IV) Oxide Catalyst. *Ind. Eng. Chem. Res.* **1991**, *30*, 18–21.

(11) Zamar, F.; Trovarelli, A.; de Leitenburg, C.; Dolcetti, G. CeO_2-Based Solid Solutions with the Fluorite Structure as Novel and Effective Catalysts for Methane Combustion. *J. Chem. Soc. Chem. Commun.* **1995**, 965.

(12) Yu, Z. Q.; Yang, X. M.; Lunsford, J. H.; Rosynek, M. P. Oxidative Coupling of Methane over Na_2WO_4/CeO_2 and Related Catalysts. *J. Catal.* **1995**, *154*, 163–173.

(13) Haneda, M.; Mizushima, T.; Kakuta, N.; Ueno, A.; Sato, Y.; Matsuura, S.; Kasahara, K.; Sato, M. Structural Characterization and Catalytic Behavior of Al2O3-Supported Cerium Oxides. *Bull.Chem.Soc.Jpn* **1993**, *66*, 1279–1288.

(14) Amirkhanova, A. K.; Krichevskii, L. A.; Kagarlitskii, A. D. Oxidative Ammonolysis of 2,5-Dimethylbyrazine over Molybdena Ceria Titania Catalysts. *Kinet. Catal.* **1994**, *35*, 838–840.

(15) Trovarelli, A. Catalytic Properties of Ceria and CeO2-Containing Materials. *Catal. Rev.* **1996**, *38*, 439–520.

(16) Flytzani-Stephanopoulos, M. Gold Atoms Stabilized on Various Supports Catalyze the Water–Gas Shift Reaction. *Acc. Chem. Res.* **2014**, *47*, 783–792.

(17) Flytzani-Stephanopoulos, M.; Gates, B. C. Atomically Dispersed Supported Metal Catalysts. *Annu. Rev. Chem. Biomol. Eng.* **2012**, *3*, 545–574.

(18) Yang, X.-F.; Wang, A.; Qiao, B.; Li, J.; Liu, J.; Zhang, T. Single-Atom Catalysts:

A New Frontier in Heterogeneous Catalysis. *Acc. Chem. Res.* **2013**, *46*, 1740–1748.

(19) Kresse, G.; Hafner, J. Ab Initio Molecular Dynamics for Liquid Metals. *Phys. Rev. B* **1993**, *47*, 558–561.

(20) Kresse, G.; Furthmüller, J. Efficiency of Ab-Initio Total Energy Calculations for Metals and Semiconductors Using a Plane-Wave Basis Set. *Comput. Mater. Sci.* **1996**, *6*, 15–50.

(21) Kresse, G.; Furthmüller, J. Efficient Iterative Schemes for Ab Initio Total-Energy Calculations Using a Plane-Wave Basis Set. *Phys. Rev. B* **1996**, *54*, 11169–11186.

(22) Blöchl, P. E. Projector Augmented-Wave Method. *Phys. Rev. B* **1994**, *50*, 17953–17979.

(23) Fu, Q.; Saltsburg, H.; Flytzani-Stephanopoulos, M. Active Nonmetallic Au and Pt Species on Ceria-Based Water-Gas Shift Catalysts. *Science* **2003**, *301*, 935–938.

(24) Zhai, Y.; Pierre, D.; Si, R.; Deng, W.; Ferrin, P.; Nilekar, A. U.; Peng, G.; Herron, J. A.; Bell, D. C.; Saltsburg, H.; Mavrikakis, M.; Flytzani-Stephanopoulos, M. Alkali-Stabilized Pt-OH_x Species Catalyze Low-Temperature Water-Gas Shift Reactions. *Science.* **2010**, *329*, 1633–1637

(25) Yang, M.; Li, S.; Wang, Y.; Herron, J. A.; Xu, Y.; Allard, L. F.; Lee, S.; Huang, J.; Mavrikakis, M.; Flytzani-Stephanopoulos, M. Catalytically Active Au-$O(OH)_x$- Species Stabilized by Alkali Ions on Zeolites and Mesoporous Oxides. *Science (80-.).* **2014**, *346*, 1498–1501.

(26) Peterson, E. J.; DeLaRiva, A. T.; Lin, S.; Johnson, R. S.; Guo, H.; Miller, J. T.; Kwak, J. H.; Peden, C. H. F.; Kiefer, B.; Allard, L. F.; Ribeiro, F. H.; Datye, A. K. Low-Temperature Carbon Monoxide Oxidation Catalysed by Regenerable Atomically Dispersed Palladium on Alumina. *Nat. Commun.* **2014**, *5*, 4885.

(27) Qiao, B.; Wang, A.; Yang, X.; Allard, L. F.; Jiang, Z.; Cui, Y.; Liu, J.; Li, J.; Zhang, T. Single-Atom Catalysis of CO Oxidation Using Pt_1/FeO_x. *Nat. Chem.* **2011**, *3*, 634–641.

(28) Vilé, G.; Albani, D.; Nachtegaal, M.; Chen, Z.; Dontsova, D.; Antonietti, M.; López, N.; Pérez-Ramírez, J. A Stable Single-Site Palladium Catalyst for Hydrogenations. *Angew. Chem. Int. Ed.* **2015**, *54*, 11265–11269.

(29) Wei, H.; Liu, X.; Wang, A.; Zhang, L.; Qiao, B.; Yang, X.; Huang, Y.; Miao, S.; Liu, J.; Zhang, T. FeO_x-Supported Platinum Single-Atom and Pseudo-Single-Atom Catalysts for Chemoselective Hydrogenation of Functionalized Nitroarenes. *Nat. Commun.* **2014**, *5*, 5634.

(30) Bruix, A.; Lykhach, Y.; Matolínová, I.; Neitzel, A.; Skála, T.; Tsud, N.; Vorokhta, M.; Stetsovych, V.; Ševčíková, K.; Myslivecek, J.; Fiala, R.; Václavů, M.; Prince, K. C.; Bruyère, S.; Potin, V.; Illas, F.; Matolín, V.; Libuda, J.; Neyman, K. M. Maximum Noble-Metal Efficiency in Catalytic Materials: Atomically Dispersed Surface Platinum. *Angew. Chem. Int. Ed.* **2014**, *53*, 10525–10530.

(31) Aleksandrov, H. A.; Neyman, K. M.; Vayssilov, G. N. The Structure and Stability of Reduced and Oxidized Mononuclear Platinum Species on Nanostructured Ceria from Density Functional Modeling. *Phys. Chem. Chem.*

Phys. **2015**, *17*, 14551–14560.

(32) Vayssilov, G. N.; Lykhach, Y.; Migani, A.; Staudt, T.; Petrova, G. P.; Tsud, N.; Skála, T.; Bruix, A.; Illas, F.; Prince, K. C.; Matolín, V.; Neyman, K. M.; Libuda, J. Support Nanostructure Boosts Oxygen Transfer to Catalytically Active Platinum Nanoparticles. *Nat. Mater.* **2011**, *10*, 310–315.

(33) Migani, A.; Vayssilov, G. N.; Bromley, S. T.; Illas, F.; Neyman, K. M. Greatly Facilitated Oxygen Vacancy Formation in Ceria Nanocrystallites. *Chem. Commun.* **2010**, *46*, 5936.

(34) Hu, Z.; Li, B.; Sun, X.; Metiu, H. Chemistry of Doped Oxides: The Activation of Surface Oxygen and the Chemical Compensation Effect. *J. Phys. Chem. C* **2011**, *115*, 3065–3074.

(35) McFarland, E. W.; Metiu, H. Catalysis by Doped Oxides. *Chem. Rev.* **2013**, *113*, 4391–4427.

(36) Hadjiivanov, K. I.; Vayssilov, G. N. Characterization of Oxide Surfaces and Zeolites by Carbon Monoxide as an IR Probe Molecule. *Adv. Catal.* **2002**, *47*, 307–511.

(37) Hoffmann, F. Infrared Reflection-Absorption Spectroscopy of Adsorbed Molecules. *Surf. Sci. Rep.* **1983**, *3*, 107.

(38) Greenler, R. G.; Burch, K. D.; Kretzschmar, K.; Klauser, R.; Bradshaw, A. M.; Hayden, B. E. Stepped Single-Crystal Surfaces as Models for Small Catalyst Particles. *Surf. Sci.* **1985**, *152*, 338–345.

(39) Rice, C.; Tong; Oldfield, E.; Wieckowski, A.; Hahn, F.; Gloaguen, F.; Léger, J.-M.; Lamy, C. In Situ Infrared Study of Carbon Monoxide Adsorbed onto Commercial Fuel-Cell-Grade Carbon-Supported Platinum Nanoparticles: Correlation with ^{13}C NMR Results. *J. Phys. Chem. B* **2000**, *104*, 5803–5807.

(40) Arenz, M.; Mayrhofer, K. J. J.; Stamenkovic, V.; Blizanac, B. B.; Tomoyuki, T.; Ross, P. N.; Markovic, N. M. The Effect of the Particle Size on the Kinetics of CO Electrooxidation on High Surface Area Pt Catalysts. *J. Am. Chem. Soc.* **2005**, *127*, 6819–6829.

(41) Lykhach, Y.; Kozlov, S. M.; Skála, T.; Tovt, A.; Stetsovych, V.; Tsud, N.; Dvořák, F.; Johánek, V.; Neitzel, A.; Mysliveček, J.; Fabris, S.; Matolín, V.; Neyman, K. M.; Libuda, J. Counting Electrons on Supported Nanoparticles. *Nat. Mater.* **2016**, *15*, 284–288.